

The Pennsylvania State University  
The Graduate School  
College of Earth and Mineral Sciences

DEPOSITIONAL ENVIRONMENTS OF PALEOCENE PLANT  
LOCALITIES WITHIN ESTUARINE FACIES OF THE SALAMANCA FORMATION,  
CHUBUT PROVINCE, ARGENTINA

A Thesis in  
Geosciences  
by  
Emily E. Comer

© 2011 Emily E. Comer

Submitted in Partial Fulfillment  
of the Requirements  
for the Degree of

Master of Science

December 2011

The thesis of Emily E. Comer was reviewed and approved\* by the following:

Rudy L. Slingerland  
Professor of Geology  
Thesis Advisor

Peter D. Wilf  
Associate Professor of Geosciences

Michael A. Arthur  
Professor of Geosciences

Chris J. Marone  
Professor of Geosciences  
Associate Head of Graduate Program of the Department of Geosciences

\*Signatures are on file in the Graduate School.

## ABSTRACT

The most well preserved and diverse early Paleocene macrofloras from Gondwana occur within sediments from Chubut Province, Patagonia, Argentina. Two prolific sites of fossil preservation, Palacio de los Loros and Parque Provincial Ormachea, sit near the top of the southwestern outcrops of the Danian (65.5-61.7 Ma) Salamanca Formation. Resting just above an unconformity spanning the K-T boundary, the Salamanca Fm. provides evidence of plant recovery after the extinction event and the depositional environments in which these floras existed.

This thesis provides a sedimentological description and paleoenvironmental interpretation of the Salamanca and Banco Negro Inferior Fms. in their southwestern outcrops and places macroflora fossil localities in stratigraphic context. The Salamanca Fm. in the area 25-40 km south of Sarmiento, Argentina consists of ten facies and four facies associations representing a transgression onto continental Cretaceous facies followed by regression and infilling of marine, tidal facies. Lower sections of the Salamanca Fm. contain abundant glauconite and fossils characteristic of an open marine shelf environment. These facies transition upward to bi-directional trough cross-bedded sands interspersed with flaser-bedded sandy silts. Cross beds indicate meso-tidal currents with paleocurrent directions that cluster in the NW-SW quadrants. The uppermost unit of the Salamanca Fm. is composed of sands and silts that gradationally transition to dark muds of the Banco Negro Inferior (BNI) Fm. These silts and muds are interpreted as a series of stacked gleysols and vertisols consisting of montmorillonite, illite, glauconitic, and halloysite clay phases deposited through progradation of a

widespread inland swamp. High aluminum content is the cause of dark coloration within the BNI Fm.

Plant localities at PL and OR occur at two stratigraphic levels within the upper Salamanca Fm. and represent accumulation in five types of sedimentary deposits- silty beds of accretion sets, transported silt lenses, mud drapes, tidal flats, and muddy deposits along low-energy tidal channels. These sedimentary deposits signify two stages of estuary infilling and the progradation of a widespread, coastal swamp represented by the Banco Negro Inferior Fm.

Two-dimensional hydrodynamic modeling of tidal currents and ranges in the proto-San Jorge embayment produce tidal amplitudes of 1-3.5 m, consistent with the hypothesis that the Salamanca Fm. was deposited in an open estuary that amplified Paleocene microtidal Atlantic tides to meso-tidal range.

## TABLE OF CONTENTS

List of Figures.....	vi
Acknowledgements.....	xi
Introduction.....	1
Geologic Setting.....	3
Methods.....	11
Results.....	19
Facies Descriptions and Association.....	19
Sand Petrography.....	46
Basin Analysis.....	50
Modeling.....	57
Discussion.....	68
Conclusions.....	78
Bibliography.....	80
Appendix A: Stratigraphic Columns.....	85
Appendix B: XRD Patterns.....	98
Appendix C: Chemical Analysis.....	138
Appendix D: Petrographic Analysis.....	139
Appendix E: Paleocurrent Directions.....	141
Appendix F: Grain Size Results.....	142

**LIST OF FIGURES**

- FIG. 1: Map showing the placement of the area covered by the San Jorge Basin and the localities within. Dots represent well log locations, A-A' is the cross section shown in Fig. 23. Salamanca Fm. outcrops are shown in gray (Brea et al. 2005, Iglesias et al. 2007). The dotted lines represent major highways 20 and 26 in the area. "Basalts" represent the area where basalt samples were taken for dating. The thickest solid line represents the outline of the San Jorge Basin as described by Sylwan (2001); thinner lines represent lakes, rivers, and the border between Chile and Argentina. The dashed and dotted line represents the political boundary between Chubut and Santa Cruz provinces. OR is Ormachea Park, PL is Palacio de los Loros, RG is Rancho Grande, and LF is Las Flores.....4
- Fig. 2: Stratigraphy and ages of formations within the San Jorge Basin. Important formations in this study are the Salamanca Fm. and the Banco Negro Inferior Fm. (part of the Rio Chico Group). Stratigraphic interpretation of this area is based on descriptions by Feruglio (1949), Uliana and Biddle (1988), Sylwan (2001), Raigemborn (2006), and Iglesias (2007).....6
- Fig. 3: Structure map of the unconformity at the base of the Salamanca Fm. as mapped in resistivity wireline logs. Contour interval is 50 m and depths represent measured depth (MD) This map shows the gradual deepening of the Salamanca Fm. toward the east reaching depths of 1000 m.....9
- Fig. 4: Fig. 4: Map of the OR field site with locations of strat columns and plant localities (OR-1, OR-2, Cerro Solo, Dromedary Hill, and Cerro Colorado). Lines represent cliff faces traced from Google Earth. Star represents location of clay mineralogy samples.....12
- Fig. 5: Map of the PL field site with locations of strat columns (A through I) and plant localities (PL-1, PL-2, PL-3, PL-4, and PL-5). Lines represent GIS points taken along cliff faces integrated with tracings of cliff facies from Google Earth.....13
- Fig. 6: Strat column with legend (Maria Sol Raigemborn, personal communication) detailing the stratigraphy where XRD and chemical analysis samples were collected. Samples used in the chemical analysis are BP-2, BP-7, BP-11, BP-13-I, BP-17, and BP-20. The base of this column lies at the top of facies 1a and extends through facies 7, 8, and 10 to the base of the Peñas Coloradas Fm..... 14
- Fig. 7: Strat column from Dromedary Hill at OR showing location of five samples taken for petrographic analysis; OR1001, OR1003, OR1004, and OR1005 (for legend see Appendix A). Facies, paleoenvironmental interpretation, and paleocurrent measurements are also noted..... 17

Fig. 8 A-J: Field photos detailing facies described in text: A) facies 5- transgressive sandy lag with pebbles, marine fossils, and cross beds at Dromedary Hill, OR; B) facies 9- wispy bedded clay with burrows near the upper contact; C) facies 6- flaser, wavy, and lenticular rhythmic bedding at Abigarrado Hill, OR; D) facies 4- hummocky cross-stratification at OR; E) petrified stump from PL; F) facies 1b- unidirectional cross-bedded sands lying conformably within facies 1a- coarse grained trough cross-bedded sands; G) clay drapes within facies 1a; H) Interfingering between facies 1a and facies 7- accretion-bedded silts; I) PL-2 locality and plant fossils within; J) mottling within facies 8- transitional sands and silts; K) Outcrop of facies 2- plane parallel-laminated sands unconformably overlying facies 6; L) Outcrop photo at Palacio de los Loros showing the progression of facies 6, 3 (heterolithic sands), 1a, 7, 8, and 10 (black muds of the BNI).....20-21

Fig. 9: Rose diagrams showing paleocurrent directions at all localities together as well as individual localities PL, OR, and LF (for raw data see Appendix F). These rose diagrams do not indicate any dominant direction, but when combined, data from all localities clusters to the E and WSW. Zero degrees is to the North.....23

Fig. 10: XRD pattern from sample BP-2 (see Fig. 6 for stratigraphic location) showing the natural, glycolated, and calcined sample diffraction patterns. Expansion and collapse of the montmorillonite peak are shown between 5-7  $\theta$ . The subdued illite/glaucinite peak appears at 8 $\theta$ . The halloysite clay peak occurs at 13  $\theta$  expands to 10  $\theta$  in the glycolated sample and is destroyed when calcined.....33

Fig. 11: Graph showing the near linear relationship between iron oxide and stratigraphic position.....35

Fig. 12: Graph showing the relationship between aluminum oxide and stratigraphic position in the chemical analysis samples. The darkest samples (between 4-6 m stratigraphically) have the highest aluminum oxide content.....35

Fig. 13: Graph showing the CIA of chemical analysis samples. The lowest sample has a Significantly lower CIA value whereas the other 5 samples have higher values. All samples ranging between 77-84 indicate a moderate to intense degree of weathering.....39

Fig. 14: Correlation diagram showing the sequence stratigraphy among measured sections at OR (Fig. 4). With the exception of the Dromedary Hill section, only the LST and top of the HST are exposed in outcrop. See Fig. 16 for details.....43

Fig. 15A,B: Correlation diagram showing the sequence stratigraphy among measured

sections at PL (Fig. 3). Spacing is not relative to distance between localities. See Fig. 16 for details.....	44
Fig. 16: Correlation diagram showing the sequence stratigraphy between PL, OR, and RG. Facies are indicated by number, also shown are sample locations and plant localities. Spacing is relative to distance. Dotted lines between OR and RG columns represent uncertainty because the RG locality could not be correlated to either the basal unconformity or facies 10. Two sequences are represented by these strat columns. The first sequence begins with a transgressive systems tract (TST) overlain by a highstand systems tract (HST). This first sequence is overlain by an erosional unconformity succeeded by 15-20 m of lowstand systems tract (LST) deposits representing sequence 2. The marine flooding surface (mfs) lies at the base of the TST and the maximum marine flooding surface (mmfs) lies at the top of the TST. Datum is erosion at base of facies 1a (see Fig. 1 for locations).....	45
Fig. 17: QFL diagram based on the Folk (1970) classification system. All petrography samples cluster within the litharenite and feldspathic litharenite categories.....	47
Fig. 18: QFL diagram based on the Dickinson (1983) classification system. PL and OR samples lie within the recycled orogen whereas LF samples lie within the undissected arc orogen.....	47
Fig. 19: QmFLt diagram based on the Dickinson (1983) classification system. PL and OR samples lie within the recycled orogen whereas LF samples lie within the undissected arc and transitional arc orogen.....	48
Fig. 20: Graph showing the mean grain size vs. lithic content of the seven samples used for the petrographic analysis. This graph shows no relationship between grain size and percent lithics indicating that increased lithic content in the LF localities is the result of real differences in provenance rather than a bias due to higher mean grain sizes.....	49
Fig. 21: Wireline log in meters showing the resistivity (RES curve). The subsurface expression of facies within the Salamanca Fm. in these logs mirror the facies described by Feruglio (1949). The API number is listed at the top of the well and can be found in Fig. 23.....	51
Fig. 22: Resistivity curve a well approximately 17 km away from outcrops showing the correlation between the Salamanca Fm. in the subsurface and PL and OR. Facies are correlated according to resistivity signature. Spacing is relative to distance. The API number is listed at the top of the well (T74) (see Fig. 23 for location relative to other logs).....	52
Fig. 23: Cross section A-A' (for location see Fig. 1) of the resistivity logs showing the	



thickening of the Salamanca Fm. toward the east. This cross section also shows the transition of facies from west to east and three distinct facies patterns (1, 2, and 3).....	55
Fig. 24: Isopach of the Salamanca Fm. based on resistivity wireline logs. This isopach map shows thickening of the Salamanca Fm. to the east, reaching thicknesses of 150 m in the most eastern wells. Contour interval is 5 m.....	56
Fig. 25: Geometry of the funnel-shaped embayment. Thick lines represent open boundaries and color bar represents bathymetry in meters.....	55
Fig. 26: Geometry of the arcuate embayment. Thick lines represent open boundaries, and color bar represents bathymetry in meters.....	58
Fig. 27: Tidal range of the funnel-shaped embayment showing maximum tidal amplification of 3.5 m near the head of the estuary.....	59
Fig. 28: Tidal range of the arcuate embayment showing maximum tidal amplification of 2.5 m near the head of the estuary.....	59
Fig. 29: Graph showing the relationship between water depth and tidal amplification at PL and OR in the funnel-shaped embayment. Maximum amplification occurs at a uniform depth of 25 m.....	61
Fig. 30: Graph showing the relationship between water depth and tidal amplification at PL and OR in the arcuate embayment. Maximum amplification occurs at a uniform depth of 25 m.....	61
Fig. 31A-C: Depth averaged velocity in the funnel-shaped embayment in two hour time increments. Velocities within the embayment follow repeating patterns every six hours, consistent with the ebb and flood currents of M2 tides. Maximum velocities occur near the estuary head as tides rush into and out of the most constricted area of the embayment.....	63-64
Fig. 32A-C: Depth averaged velocity in the arcuate embayment in two hour time increments. Velocities within the embayment follow repeating patterns every six hours, consistent with the ebb and flood currents of M2 tides. Maximum velocities occur in the landward portion of the embayment.....	64-65
Fig. 33: Net deposition and erosion in the funnel-shaped embayment after five years. This figure represents the high sediment concentration end member and shows increasing sedimentation in the fluvial headwaters suggesting the formation of bayhead deltas. Sedimentation in other areas of the embayment remains fairly uniform.....	66

- Fig. 34: Net deposition and erosion in the arcuate embayment after 5 years. This figure represents the high sediment concentration end member and shows increasing sedimentation in the fluvial headwaters suggesting the formation of bayhead deltas. Sedimentation in other areas of the embayment remains fairly uniform.....67
- Fig. 35: Net deposition and erosion in the funnel shaped embayment after 5 years. This figure represents the low sediment concentration end member and shows increasing sedimentation in the fluvial headwaters but no formation of bayhead deltas. Sedimentation in other areas of the embayment remains fairly uniform.....67
- Fig. 36: Net deposition and erosion in the arcuate embayment after 5 years. This figure represents the low sediment concentration end member and shows increasing sedimentation in the fluvial headwaters and the possible formation of a bayhead delta. Sedimentation in other areas of the embayment remains fairly uniform.....68
- Fig. 37: Proposed eustatic sea level curve for the Chubut Group and Salamanca and Banco Negro Inferior Fms. showing time and formation of systems tracts and facies. Numbers refer to stages in Fig. 38.....70
- Fig. 38: Depositional model for the four stages of the Salamanca and BNI Fms., in the vicinity of PL, OR, and RG.....72
- Fig. 39: Modern-day analog for the depositional environment of A)The Bahía Blanca estuary (photo from NASA <http://www.sciencephoto.com/media/174830/view>) later stage of the Salamanca Fm. and B) The Great Dismal Swamp of Virginia (<http://www.fws.gov/northeast>) as an analog for the Banco Negro Inferior....77

## ACKNOWLEDGEMENTS

This research is part of a larger collaborative research project encompassing the fields of paleobotany, sedimentology, geochronology, and palynology funded by the National Science Foundation, grant number DEB-0919071. Other sources of funding include The Pennsylvania State University Department of Geosciences, the Paul D. Krynine fund, and Shell and Chevron travel grants. Yacimiento Petrolifero Fiscales (YPF) and PanAmerican Energy (PAE) are thanked for providing the wireline logs used for basin analysis. I would like to thank my advisor Rudy Slingerland as well as my committee members Peter Wilf and Mike Arthur for their input and advice. Thanks to Heather Graham for TOC and biomarker analysis, Henry Gong for chemical analysis, and Nichole Wonderling for help in interpreting XRD data.

A big thank you to my Argentine colleagues: Ari Iglesias for enlightening me with his knowledge of the history and stratigraphy of the San Jorge Basin, Marcelo Krause for obtaining and aiding in correlation of wireline logs, and Maria Sol Raigemborn for providing the samples used in XRD and chemical analysis. Thank you to the Museo Paleontológico Egidio Feruglio (MEF) and especially Pablo Puerta, without whom, we would have never survived two field seasons in the wilds of Patagonia.

Lastly thanks to my friends and family for their support and positive influences during this process. A special thanks to my mom, brother, and my boyfriend Ryan David Swanson. Thanks for putting up with me through all of this, I love you guys!

## INTRODUCTION

The Danian Salamanca Formation in the San Jorge Basin (SJB) of Chubut Province, Patagonia (Fig. 1) contains an exceptionally diverse and well-preserved macroflora that documents floral recovery less than five million years after the end Cretaceous extinction. In recent collections over 2500 compression specimens comprising 36 angiosperm leaf species (including 33 dicot and 3 monocot species) have been documented from outcrops of the Salamanca Fm. (Iglesias et al. 2007). The species of these new collections include the angiosperm groups: Nothofagaceae, Menispermaceae, Akaniaceae, Lauraceae, Urticaceae, Fabaceae, Sapindaceae, Malvaceae, and Rosaceae. In addition, conifer cones and leaves from the groups Araucariaceae and Podocarpaceae are preserved as well as ferns of the group Lygodiaceae (Iglesias 2007, Iglesias et al. 2007, Brea et al. 2008, 2011). Elevated floral species richness in these collections contrasts with low diversity floras found in the northern hemisphere during the early Paleocene (Iglesias et al. 2007).

In addition to compression floras, petrified logs are preserved in the upper facies of the Salamanca Fm. at four well-studied localities: Palacio de los Loros (PL), Ormachea Park (OR), Víctor Szlápelis, and Ameghino Petrified Forest (Fig. 1) (Brea et al. 2005, 2008, 2011). Results from these studies indicate that during the Paleocene, these sites were covered by an evergreen forest composed of conifers of the family Podocarpaceae. Tree ring analysis suggests a stable warm-temperate climate with dry summers and wet winters (Brea et al. 2005, 2008, 2011). Fossil wood from the species *Paracacioxylon frenguellii* at Palacio de los Loros is the oldest Fabaceae documented

along the western border of Gondwana and the world's second oldest sample of Mimosoideae wood (Iglesias 2007, Brea et al. 2008).

The Salamanca Fm. is also a hydrocarbon reservoir sand in the subsurface of the SJB, the second highest petroleum-producing basin in Argentina with an estimated 473 million m<sup>3</sup> of oil and 70,300 million m<sup>3</sup> of gas produced in the basin as of 2001 (Rodriguez, 2001). Over 25,000 wells have been drilled in the SJB to extract hydrocarbons generated from organic-rich, Mesozoic lacustrine source rocks such as the Pozo D-129 Fm. (Sylwan 2001). Recently, the Salamanca Fm. has been suggested as a source of significant potassium deposits (Castro et al. 2008) because glauconite is abundant in its deeper water facies. Agriculture is one of Argentina's most important economic interests and currently most of the country's fertilizer is imported (Castro et al. 2008). Abundant and easily accessible glauconitic greensands of the Salamanca Fm. could provide a cheap, easy, and "eco-friendly" source of fertilizer for Argentina's growing agricultural demands.

Given the scientific and economic importance of the Salamanca Fm. in the SJB, there is a need to better understand the nature and occurrence of its facies and depositional history. Specifically, we ask four questions: 1) What are the sedimentary facies within the Salamanca Fm. in its southwestern outcrops? 2) In what paleo-environments were the facies of the Salamanca Fm. deposited? 3) What local environments allowed for the deposition and preservation of the diverse macroflora fossils found in the Salamanca Fm.? and 4) What environmental biome did these macroflora live in? To answer these questions, we document the sedimentary facies of the Salamanca Fm. and overlying Banco Negro Inferior Fm. at four localities along the

southwestern outcrop belt of the SJB (Fig. 1) and correlate these facies throughout the central San Jorge Basin using 60 wireline logs. The result is a detailed paleogeographic reconstruction of the study region during the Late Danian that provides a depositional model for the Salamanca Fm. and places the paleofloras in a depositional setting.

### **GEOLOGIC SETTING**

The study area straddles the boundary between Chubut and Santa Cruz Provinces, Patagonia, Argentina and rests between 45 ° - 46 ° S latitude and 68 ° - 69 ° W longitude (Fig. 1). Continental extension in this region beginning in the Triassic led to the separation of South America from Africa and the opening of the Atlantic Ocean (Pasquini et al. 2005). Paleodrainage in South America was greatly affected by its separation from Africa ~100 Ma causing paleoslopes and paleodrainage to shift from westward flowing to eastward flowing (Potter 1997). This continental breakup and extension also created NNW-SSE trending normal faults that shaped large half-graben depocenters throughout Patagonia. One of these grabens, the SJB, covers approximately 170,000 km<sup>2</sup> and is bordered on the north by the Somuncura Massif, the south by the Deseado Massif, the west by the Andean Cordillera, and continues eastward toward the continental margin in the Atlantic Ocean. Although the SJB is generally extensional in the E-W direction, it is divided into eastern and western components by the N-S trending San Bernardo fold belt (Fig. 1) (Sylwan 2001).

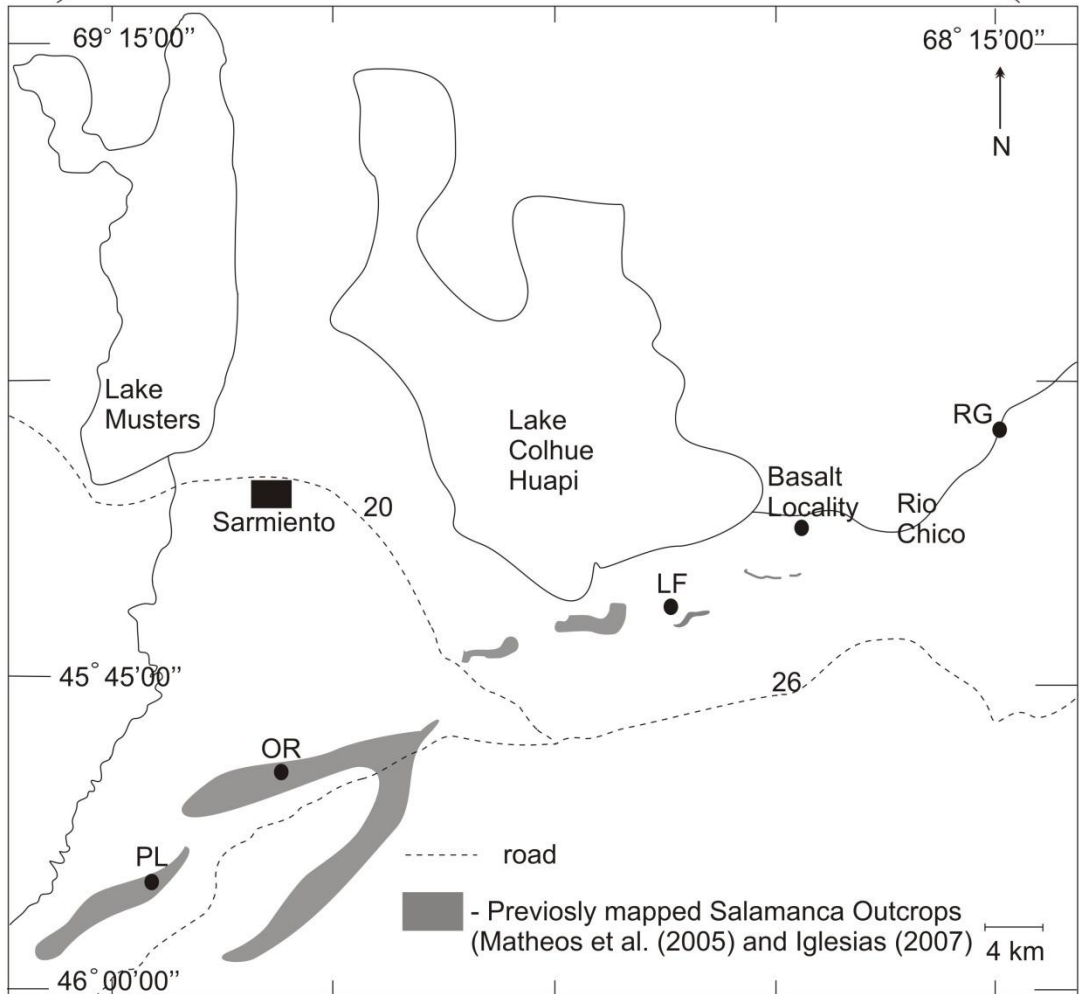
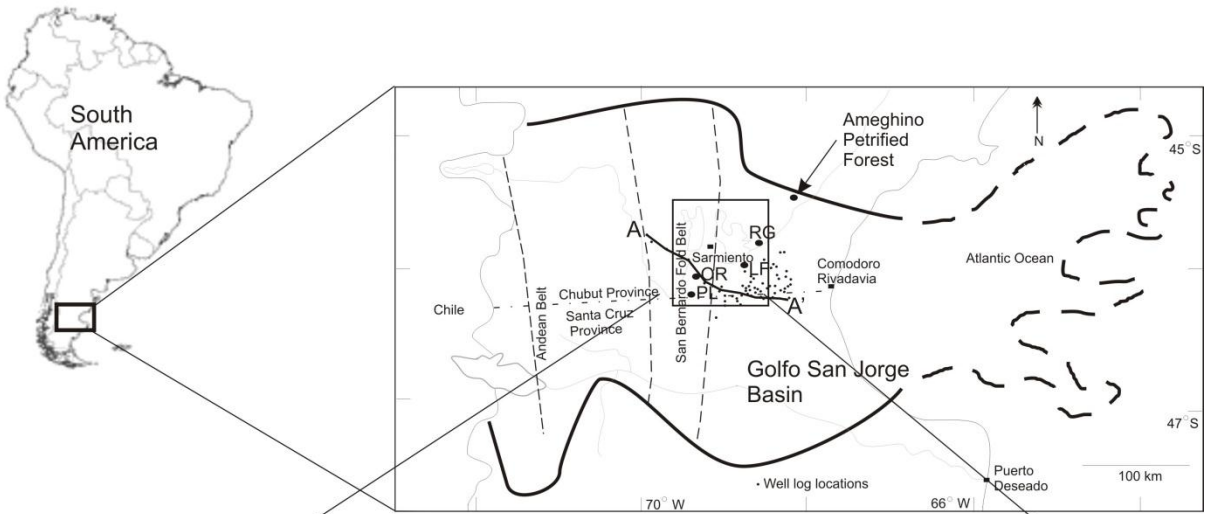


FIG. 1: Map showing the placement of the area covered by the San Jorge Basin and the localities within. Dots represent well log locations, A-A' is the cross section shown in Fig. 23. Salamanca Fm. outcrops are shown in gray (Brea et al. 2005, Iglesias et al. 2007). The dotted lines represent major highways 20 and 26 in the area. "Basalt locality" represents the area where basalt samples were taken for dating. The thickest solid line represents the outline of the San Jorge Basin as described by Sylwan (2001), thinner lines represent lakes, rivers, and the border between Chile and Argentina. The provincial boundary between Chubut and Santa Cruz is the 46<sup>th</sup> parallel. OR is Ormachea Park, PL is Palacio de los Loros, RG is Rancho Grande, and LF is Las Flores

Due to the size of the SJB, stratigraphic relationships and facies vary throughout the basin. The explanation below describes documented stratigraphic relationships in the central San Jorge Basin (Fig. 2). The SJB is underlain by Precambrian metamorphics and intrusives overlain by- Devonian granites and schists, sedimentary rocks of Carboniferous to Permian age, and igneous rocks spanning the Permian-Triassic (see Sylwan 2001 and Iglesias 2007 for detailed Paleozoic stratigraphy). These Paleozoic basement rocks lie at depths of 500-1,750 m (Iglesias 2007).

Increased accommodation in the SJB during the Jurassic allowed for deposition of lacustrine bituminous shales, such as the Aguada Bandera Fm. (Urien et al. 1995, Sylwan 2001). Middle-Upper Jurassic volcanic and pyroclastic formations of the Lonco Trapial and Bahia Laura Groups (Rodriguez 2001) are succeeded by the Las Heras Group, consisting of two formations, the lower Pozo Anticlinal Aguada Bandera and the Pozo Cerro Guadal. The Pozo Anticlinal Aguada Bandera Fm. consists of 600-1200 m of black shale deposited in an anoxic, freshwater, lacustrine environment and is a documented hydrocarbon source rock (Iglesias 2007, Rodriguez 2001). The Pozo Cerro Guadal Fm. consists of 300 m of marine-influenced reservoir sandstones (Iglesias 2007, Rodriguez 2001).



Eon	Period	Epoch	Stratigraphy	
			Western SJB	Central SJB
Cenozoic	Cenozoic	Miocene	Santa Cruz Fm.	Superpatagonio
			Colhue Huapi Fm.	
		Oligocene	Patagoniano	Patagoniano
		Eocene	Sarmiento Fm.	
		Paleocene	Rio Chico Group	Rio Chico Group
	Salamanca Fm.			
Mesozoic	Cretaceous	Upper	Las Palacios Fm.	Y. el Trébol/M. Espinosa Fm.
			Bajo Barreal Fm. Upper	
			Bajo Barreal Fm. Lower	C. Rivadavia/C Seco Fm.
		Lower	Castillo Fm.	Mina del Carmen Fm.
			Matasiete Fm.	Pozo D. 129 Fm.
		P.C. Guadal Fm.	P.C. Guadal Fm.	
Jurassic	Upper	P.A.A. Bandera Fm.	P.A.A. Bandera Fm.	

Fig. 2: Stratigraphy and ages of formations within the San Jorge Basin. Important formations in this study are the Salamanca Fm. and the Banco Negro Inferior Fm. (part of the Rio Chico Group). Stratigraphic interpretation of this area is based on descriptions by Feruglio (1949), Uliana and Biddle (1988), Sylwan (2001), Raigemborn (2006), and Iglesias (2007)

During the Cretaceous, the breakup of Pangaea was completed and Andean uplift began (Uliana and Biddle 1988, Pasquini et al. 2005, Folguera et al. 2011). The San Bernardo fold belt that defines the division between the western and eastern San

Jorge Basin began forming in the Late Cretaceous (Folguera et al. 2011) and experienced continued uplift and deformation throughout the Cenozoic. The Cretaceous Chubut Group is a 2000 m thick section of sediment beginning with black mudstone intercalated with pelitic limestones and sandstones (the Pozo-D 129 Fm.) followed by volcaniclastic sandstones of the Castillo and Bajo Barreal Fms. (Iglesias 2007, Umazano et. al 2009). The Bajo Barreal Fm. in the study area is bounded above by an erosional unconformity. Above the end-Cretaceous unconformity lie marine sediments of the Salamanca Fm ranging from 30-200 m in thickness across the basin. During Salamanca deposition, the basin evolved into a flexural foreland basin as crustal thickening increased south of the proto-Andes (Urien et al. 1995). Deformation peaked in the middle Miocene due to Nazca plate subduction (Urien et al. 1995, Sylwan 2001).

The Salamanca Fm. is designated as Middle-Upper Danian due to foraminifera and ostracods within coastal deposits (Mendez 1966, Bertels 1975). The foraminifera species *Globorotalia compressa* was found at coastal Salamanca localities Puerto Visser and Bajada de Cerro Hansen, 40 and 100 km north of Comodoro Rivadavia respectively. This species places the Salamanca Fm. as Upper Danian (Bertels 1975). The planktonic species *Subbotina triloculinoides* from Punta Peligro about 40 km north of Comodoro Rivadavia also indicates a Middle-Upper Danian age (Mendez 1966). Two basalts just below the base of the Salamanca Fm. dated by whole rock  $^{40}\text{K}$ - $^{40}\text{Ar}$  give basal ages of  $64.0 \pm 0.8$  Ma and  $62.8 \pm 0.8$  Ma (Marshall et al. 1981) and a tuff from the upper Salamanca Fm. gave an age of  $62.6 \pm 5$  Ma (Andreis 1977). Foraminifera species in the Cerro Bororó Fm. located near the northwestern edge of the San Jorge Basin identify it is Danian (Bertels 1973, Scafati et al. 2009). Thus, this freshwater formation

marks the edge of marine influence in the San Jorge Basin during the Danian (Scafati et al. 2009). Palynology from the Cerro Bororó Fm. suggests a subtropical-tropical climate during the Danian similar to climate along the modern-day Gulf of Mexico (Scafati et al. 2009). Marine sediments in other Patagonian basins, such as the Cerro Dorotea Fm. in the more southern Austral basin, indicate that marine transgression was widespread during the early Paleocene (Macellari et al. 1989). To the west and stratigraphically above the Salamanca Fm. lies the Rio Chico Group, a 50-300 m thick section consisting of muds, sands, and conglomerates of terrestrial fluvial origin (Iglesias 2007). A tuff just below the Banco Negro Superior Fm. of the Rio Chico Group was dated by  $^{40}\text{Ar}/^{39}\text{Ar}$  analysis giving an age of  $57.8 \pm 6$  Ma (Iglesias et al. 2007). The Rio Chico Group is overlain by Oligocene-Eocene tuffs of the Sarmiento Fm.

Wireline correlation shows that the Salamanca Fm. generally dips east toward the Atlantic coast reaching depths of 1200 m (Fig. 3). Salamanca outcrops studied in this project represent part of a NE-SW trending structural high that is most likely a post-depositional feature. This high is depicted in geologic maps of the area as a NE-SW trending anticline. East of the outcrop area the contours illustrate a smooth gradual deepening of the Salamanca formation (Fig. 3), however, outcrops near Comodoro Rivadavia indicate that the Salamanca Fm. rises back to the surface near the Atlantic coast. Well control is poor west of the study area but available well data shows that the Salamanca formation rises to the surface at the study area and then dips deep below the surface reaching depths up to 1000 m to the west.

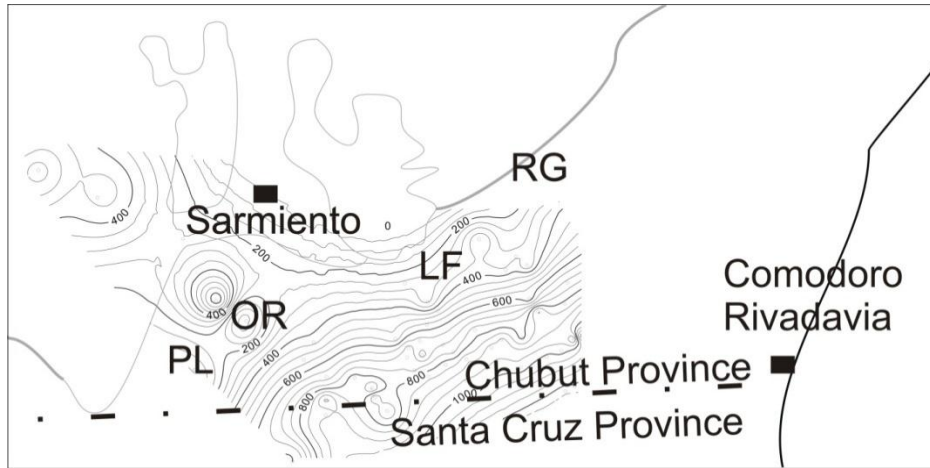


Fig. 3: Structure map of the unconformity at the base of the Salamanca Fm. as mapped in resistivity wireline logs. Contour interval is 50 m and depths represent measured depth (MD) This map shows the gradual deepening of the Salamanca Fm. toward the east reaching depths of 1000 m.

The Salamanca Fm. is characterized by glauconitic marine and estuarine sands, silts, and muds. Feruglio (1949) was one of the first to describe the Salamanca Fm. and his facies interpretations of: Lignitifero, Glauconitico, Fragmentosa, and Banco Verde, are commonly used. The basal unconformity of the Salamanca Fm. is described as Horizonte Madre or the “mother layer”. It is succeeded by the Lignitifero facies, described as thin-bedded clay interspersed with thin wisps of sand and containing marine fossils and carbonized plant remains. Above the Lignitifero is the Glauconitico facies composed of fining-upward glauconitic sands interbedded with clay lenses and containing scarce shark teeth and mollusks. The Fragmentosa facies overlying the Lignitifero facies consists of hardened gray clay with thin sandy to silty layers. The Fragmentosa contains a variety of marine invertebrate fossils and is the thickest facies in most eastern wells. The Banco Verde is the uppermost facies of the Salamanca Fm. and is comprised of glauconitic sand alternating with clay layers. The Banco Verde is capped by the Banco Negro Inferior, a black clay that has been observed and studied in

outcrops at Ormachea Park (OR) and Palacio de los Loros (PL) to Punta Peligro on the Atlantic coast (Feruglio 1949). Feruglio's descriptions and interpretations of the Salamanca Fm. focus on outcrops along the eastern coast of Chubut Province, biasing assessment of facies and paleoenvironments toward an open marine environment.

Sedimentology and paleobotany studies at PL and OR have produced other interpretations of the Salamanca Fm. Martinez (1992) described four facies within the Salamanca Fm. at OR and PL; conglomerates, sandstones, clays, and heterolithic facies. Due to the presence of tidal mud drapes and bi-directional cross-bedding, these facies were interpreted to represent sand bars, delta lobes, tidal channels, and lagoons. Trunks within the sandstone facies indicates that deposits in the upper Salamanca Fm. are proximal to continental deposits (Martinez 1992). Matheos et al. (2001) described the Salamanca Fm. at Victor Szlapelis fossil forest, approximately 25 km southeast of Sarmiento, as clays, tuffaceous clays, silts, and sands deposited in meandering fluvial and deltaic systems. Iglesias et al. (2007) described middle and lower units of the Salamanca Fm. at PL as a transgressive marine package and upper units of the Salamanca Fm. as meandering channels in a low-relief fluvial environment in which macroflora are preserved in oxbow deposits (Iglesias et al. 2007). Brea et al. (2011) stated that the Salamanca Fm. at PL represents a shallow marine transgressive-regressive sequence beginning with tidal estuarine/deltaic sediments overlain by large-scale cross-bedded sandstone indicating higher energy coastal bars. Sandstone facies containing petrified logs were interpreted as proximal to the plant source (Brea et al. 2011).

This study provides a detailed set of facies descriptions at OR and PL, from the K-T unconformity to the Banco Negro Inferior along with specific environmental interpretations for each facies, expanding on previous sedimentological interpretations. Plant localities are assigned to depositional environments, and the Salamanca and BNI Fms. are placed into a sequence stratigraphic model.

## **METHODS**

Data analyzed in this project come from two field seasons in February-March 2010 and April-May 2011. Four localities were visited in Chubut Province: Ormachea Park (OR), Palacio de los Loros (PL), Rancho Grande (RG), and Las Flores (LF) (Fig. 1). This study focuses on Ormachea Park and Palacio de los Loros because these sites contain the most fossil localities and expose the entire Salamanca Fm. from the lower Cretaceous volcanoclastics of the Chubut Group to the overlying fluvial deposits in the Rio Chico Group. Plant localities within Las Flores occur within the younger Peñas Coloradas Fm. of the Rio Chico Group (Iglesias 2007) and plant localities at Rancho Grande occur in significantly different facies that indicate a deeper-water or lagoon environment.

Prior to field work, an ArcGIS database was compiled using a large variety of maps including surface elevation and geologic maps. In the field, stratigraphic columns were measured on multiple cliff faces as well as through all major plant localities in OR and PL (Figs. 4, 5) (Appendix A). Columns were drafted in CorelDraw and hung on a datum defined by the marine flooding surface representing the Cretaceous-Paleocene unconformity. A laser ranger was used to measure dozens of facies thicknesses across

7 outcrop faces in Palacio de los Loros. These measurements were integrated with stratigraphic columns and photomosaics and imported into Fledermaus to allow a 3-D visualization of facies. Geologic and surface maps were also imported into Fledermaus for spatial reference. Approximately 100 samples were collected for analysis of biomarkers, Total Organic Carbon, grain size, clay mineralogy through X-Ray Diffraction, and sand petrography. Samples were chosen to represent the entire range of facies within Ormachea Park and Palacio de los Loros as well as important facies within Rancho Grande and Las Flores.

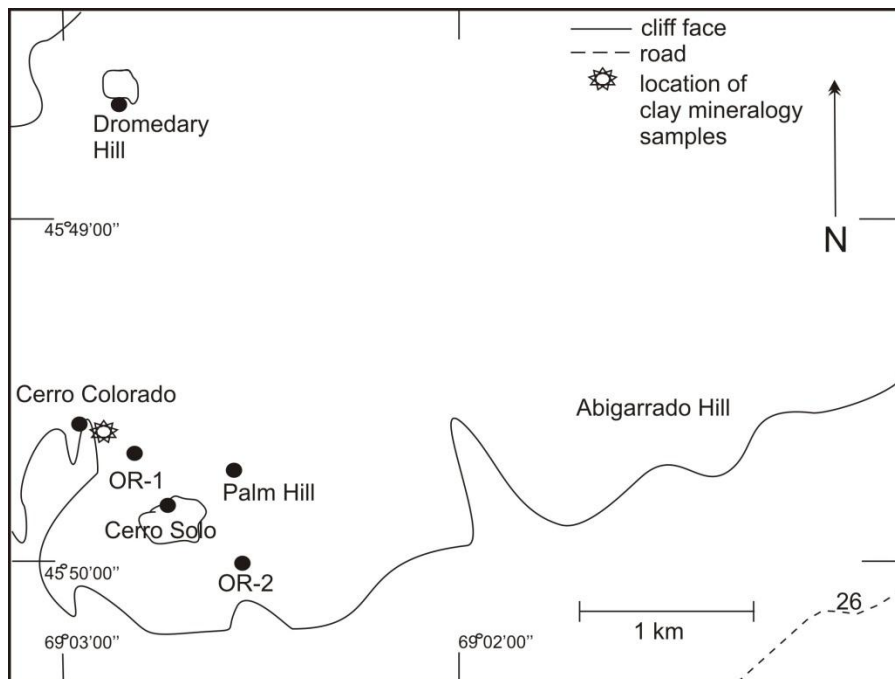


Fig. 4: Map of the OR field site with locations of strat columns and plant localities (OR-1, OR-2, Cerro Solo, Dromedary Hill, and Cerro Colorado). Lines represent cliff faces traced from Google Earth. Star represents location of clay mineralogy samples.

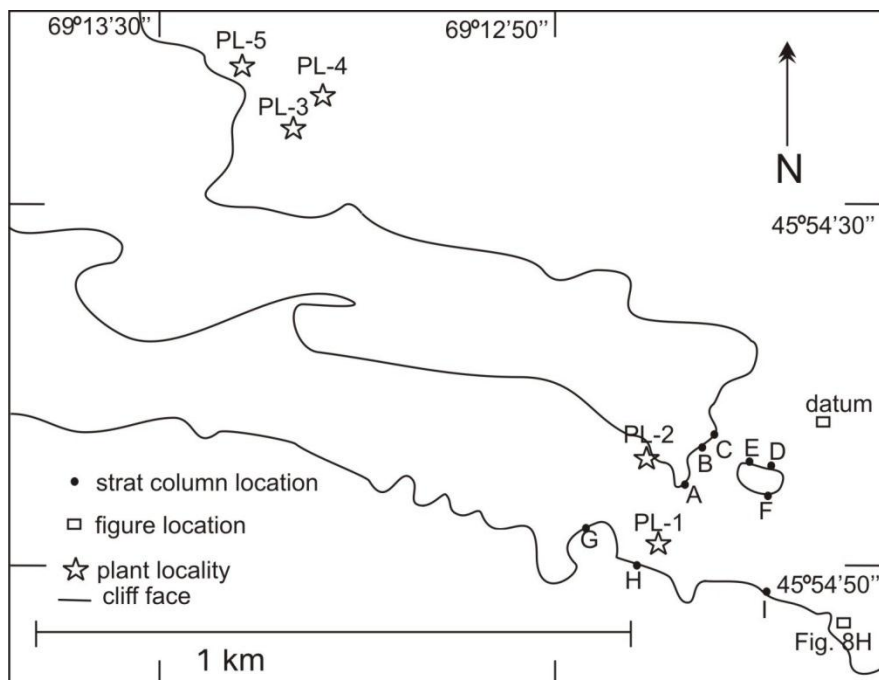


Fig. 5: Map of the PL field site with locations of strat columns (A through I) and plant localities (PL-1, PL-2, PL-3, PL-4, and PL-5). Lines represent GIS points taken along cliff faces integrated with tracings of cliff facies from Google Earth.

Twenty samples were collected (by Maria Sol Raigemborn) from Ormachea Park for a clay mineralogy study. These samples come from a 12 m section beginning in the upper Salamanca Fm. through the Banco Negro Fm. to the erosional base of the continental Peñas Coloradas Fm. of the Rio Chico Group (Figs. 4, 6). The samples were ground to a uniform 4  $\mu\text{m}$  fraction and x-rayed as an unaltered powder sample, an oriented powder sample on a glass mount, an oriented powder sample on glass mount exposed to ethylene glycol for 24-48 hours to ensure clay expansion, and an oriented sample on a glass mount heated to 550° C for 2 hours to ensure mineral collapse (Appendix B). MDI Jade and the USGS Clay Mineral Identification Flow Diagram were used to determine the clay mineral assemblage.



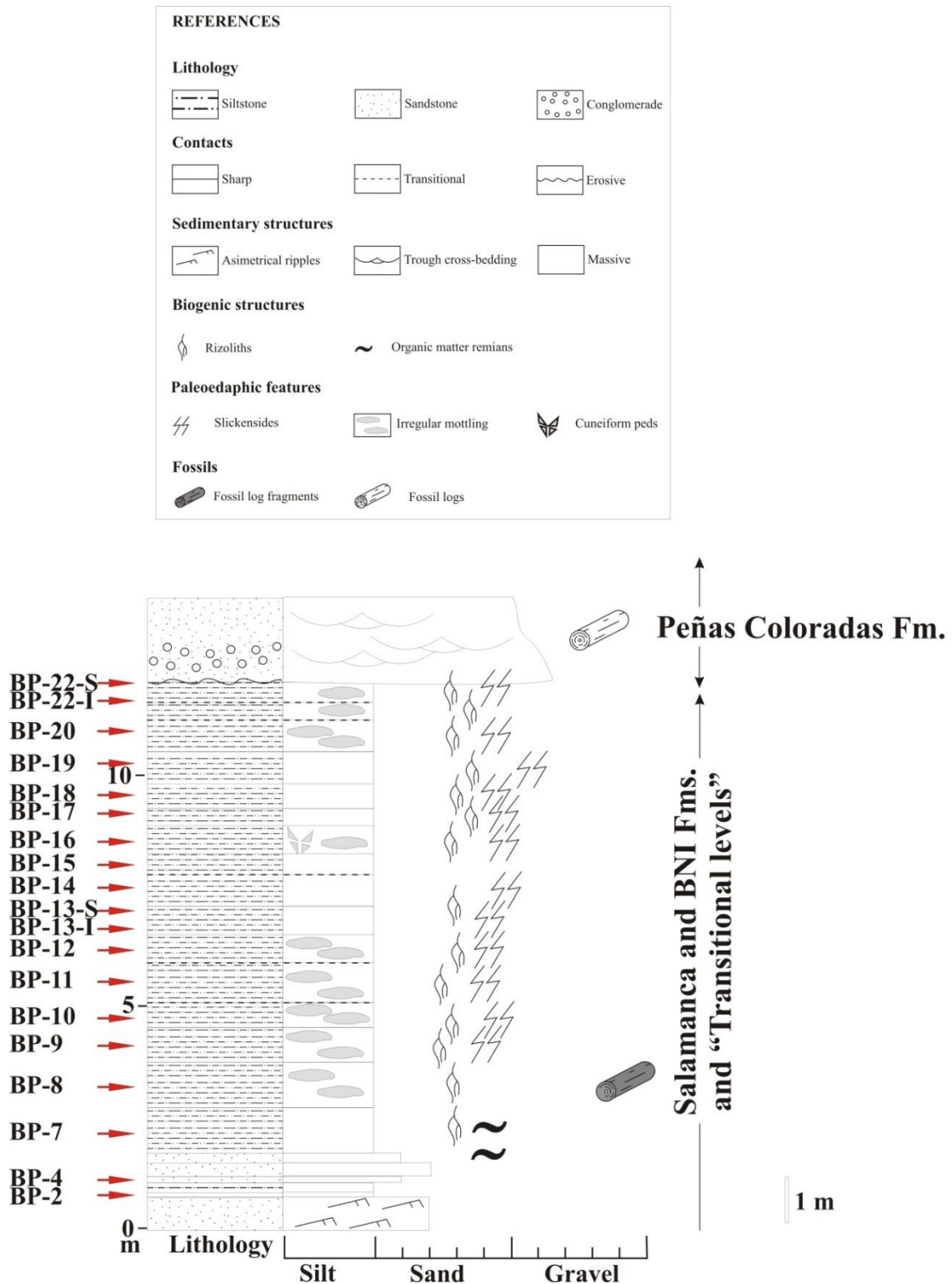


Fig. 6: Strat column with legend (samples collected and section measured by Maria Sol Raigemborn, personal communication) detailing the stratigraphy where XRD and chemical analysis samples were taken. Samples used in the chemical analysis are BP-2, BP-7, BP-11, BP-13-I, BP-17, and BP-20. The base of this column lies at the top of facies 1a and extends through facies 7, 8, and 10 to the base of the Peñas Coloradas Fm.

Chemical analyses were performed on 6 samples (Fig. 6) spanning the transition between the upper Salamanca Fm. and the Banco Negro Fm. Originally, sulfur was thought to be a major contributing element indicative of a marine environment in these sediments, and a sulfur analysis was performed on the samples using barium chloride to produce the precipitant barium sulfate. This test indicated that sulfur was a minimal component. A full chemical analysis of the oxides in these sediments was performed using a Perkin-Elmer Optima 5300 ICP (inductively coupled plasma spectrometer) after dissolution of the ground sediments by lithium metaborate (for results see Appendix C). Total Organic Carbon and biomarker tests were run on samples collected from OR and PL. The samples range in color from white to red to dark gray (Appendix C) but the most important samples are the darkest samples, BP-11 and BP-13-INF, because these samples represent the characteristic coloration of the Banco Negro Inferior. Total organic carbon content of paleosol and rock samples was obtained by elemental analysis of decarbonated sample aliquots. Fifty grams of ground and sieved material was reacted with 1N HCl for 30 minutes, neutralized thoroughly with deionized water and then lyophilized for 48 hours before analysis. Organic carbon was measured by combustion in a Costech EA coupled to a Delta XP mass spectrometer via a ConFlo system. Evolved gases are dried, then oxidized by chromium oxide and cobalt oxide, then reduced by elemental copper. Simultaneous analysis of internal and IAEA standards along with reference gases results in precision and accuracy approaching 0.3%.

Sand composition was estimated by hand lens in the field and verified in the five important sandy facies (facies 1a, 3, 5, 6, and 7) at PL, OR, and LF by point counting (Fig. 7). Samples were cut into thin sections, stained for plagioclase and potassium feldspar, and point counted using an Olympus petrographic microscope. Three hundred points were counted using the Gazzi-Dickinson point counting method (Dickinson et. al 1979) and grains were divided into the 16 categories listed in Appendix D. The data were combined with petrographic data from Raigemborn (2006) and Umazano et. al (2009) on the overlying Peñas Coloradas Fm. and interpreted using QFL and QmFLt classification systems (Folk et. al 1970, Dickinson 1983). Grain size was also determined through point counting 200 grains, and analysis of grain size was performed using Gradistat version 6.0 developed by Dr. Simon J Blott. Grain size point counts produced quantitative measures for properties such as sorting, skewness, modal grouping, and median sizes (Appendix E). Average roundness of quartz grains was determined through visual analysis using 4X and 10X magnification and a standard grain size card.

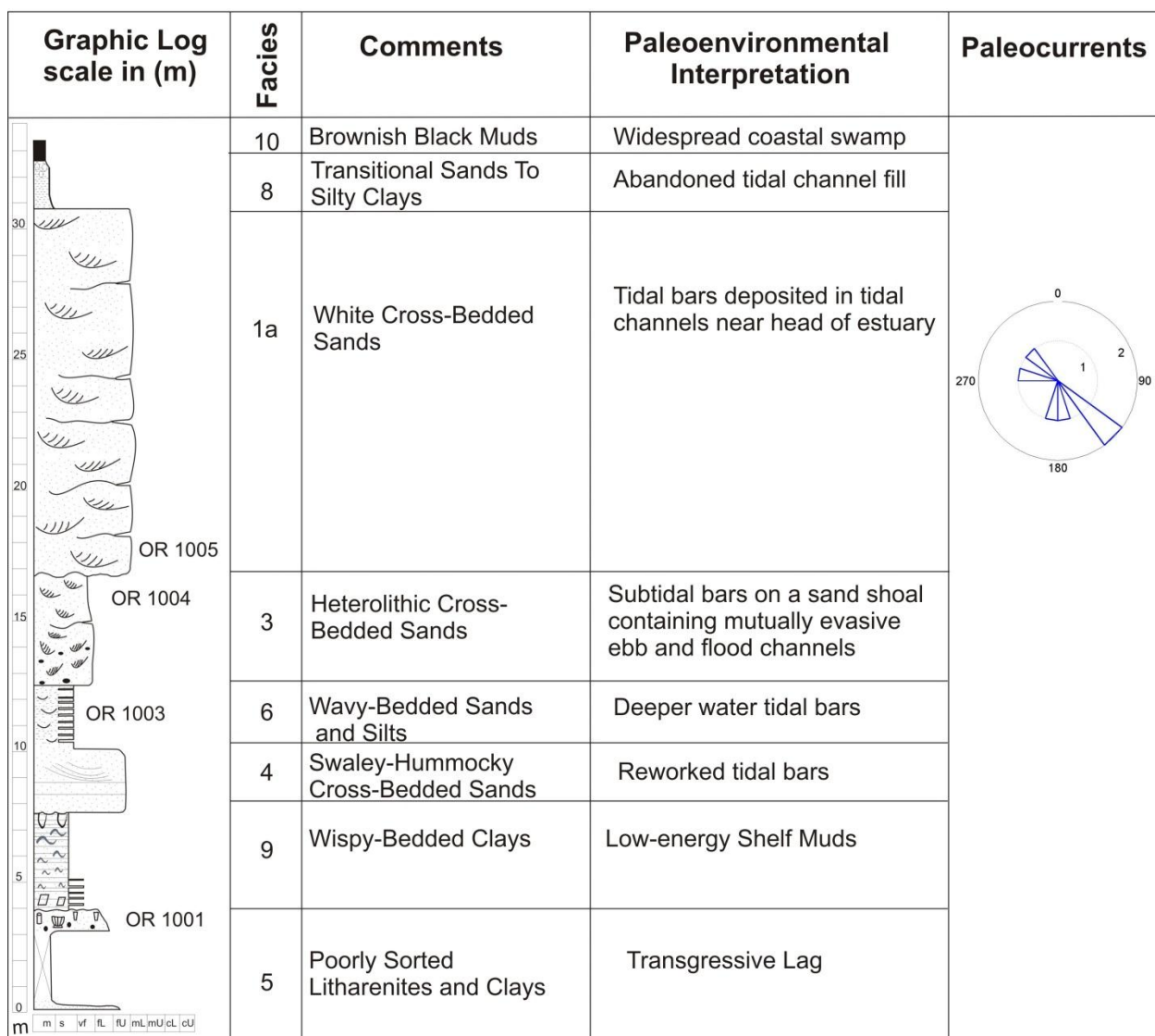


Fig. 7: Strat column from Dromedary Hill at OR showing location of five samples taken for petrographic analysis; OR1001, OR1003, OR1004, and OR1005 (for legend see Appendix A). Facies, paleoenvironmental interpretation, and paleocurrent measurements are also noted.

Facies defined in outcrop were mapped in the subsurface using 60 wireline logs from Pan American Energy Company (PAE). Private raster logs from Yacimientos Petroliferos Fiscales (YPF), stratigraphy studies across the SJB (Lesta 1968), and previous facies descriptions of the Salamanca Fm. (Feruglio 1949) aided in the identification of the Salamanca Fm. in the subsurface. Logs were correlated using

resistivity and SP values, and though the upper limit of the Salamanca varies spatially, the lower contact representing the Cretaceous-Paleogene boundary is distinctive in most logs.

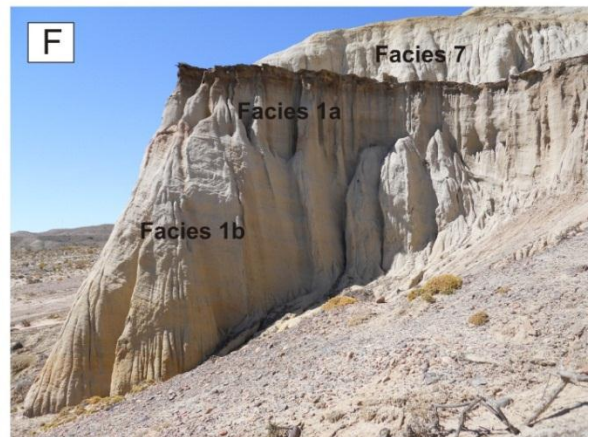
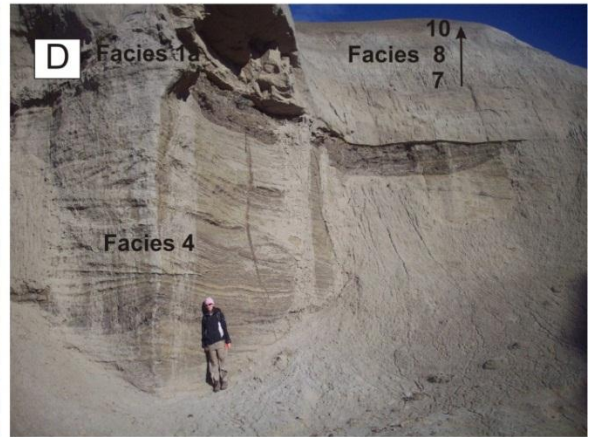
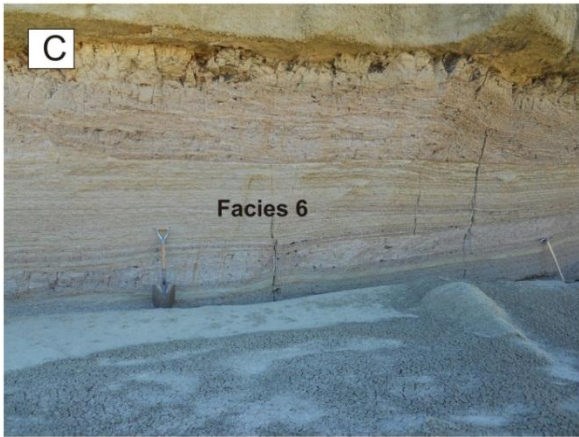
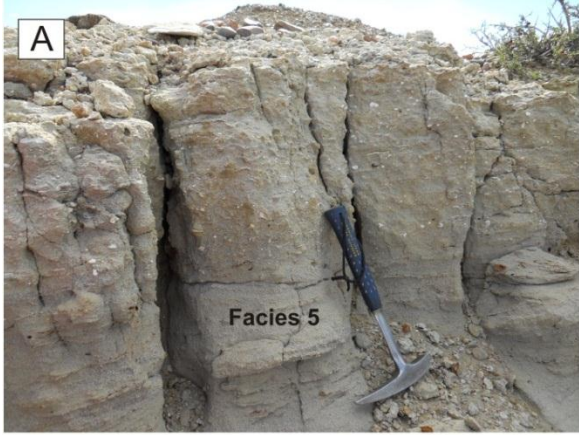
To test the conjecture of a tidal origin for some facies, a model of the paleo-SJB was created using Delft3D, a hydrodynamic sediment transport model created by Deltares. Two configurations of the San Jorge embayment were analyzed, one representing a funnel-shaped estuary with a significant principal river source, and one representing a large arcuate embayment with lesser fluvial input sources. Both geometries honor the geographic extent of present day Salamanca Fm. outcrops with lengths representing the distance from the San Bernardo belt to the modern-day Atlantic coast and widths representing the N-S extent of mapped Salamanca outcrops. The average length of the funnel-shaped embayment is 222 km. The head of the estuary is 13 km wide and the open ocean boundary is approximately 400 km in width N-S. The average length of the arcuate embayment is 213 km with a N-S open ocean boundary of 430 km. Depth in both configurations increases gradually seaward from 3 to 150 m, consistent with modern shallow continental embayments (Glorioso and Flather 1997). Multiple runs with uniform bathymetries of 5 to 150 m were simulated using the two geometries to determine the relationship between bathymetry and tidal wave amplification. The paleo-latitude was set at  $-45^{\circ}$  for an accurate Coriolis acceleration. Both cohesive (.2 mm grain size) and non-cohesive (.15 mm grain size) sediments were available for transport in the basin and were set to equilibrium concentrations. Initial conditions consisted of a water level of 0 m and a salinity of 25 ppt. The model was run with two initial sediment inputs representing the high and low end of sediment

concentration with high end concentrations on the order of  $\text{kg/m}^3$  and low end concentrations of the order of  $\text{mg/m}^3$ . The number of rivers entering the embayment from the west was variable from one to six. A water level boundary with a reflection parameter of  $50 \text{ s}^2$  and an M2 shelf tide with an amplitude of 80 cm, similar to modern M2 tides on the Patagonian shelf (Glorioso and Simpson 1994), were imposed at the shelf edge. Open boundaries of rivers entering the system varied between 1-13 km in width and 2000-10000  $\text{m}^3/\text{s}$  in discharge. Gravity, water density, and temperature were kept at  $9.81 \text{ m/s}^2$ ,  $1000 \text{ kg/m}^3$ , and  $15^\circ \text{ C}$  respectively.

## **RESULTS**

### **FACIES DESCRIPTIONS AND ASSOCIATIONS**

The Salamanca and Banco Negro Inferior Fms. in the study area consist of 10 facies (Fig. 8).



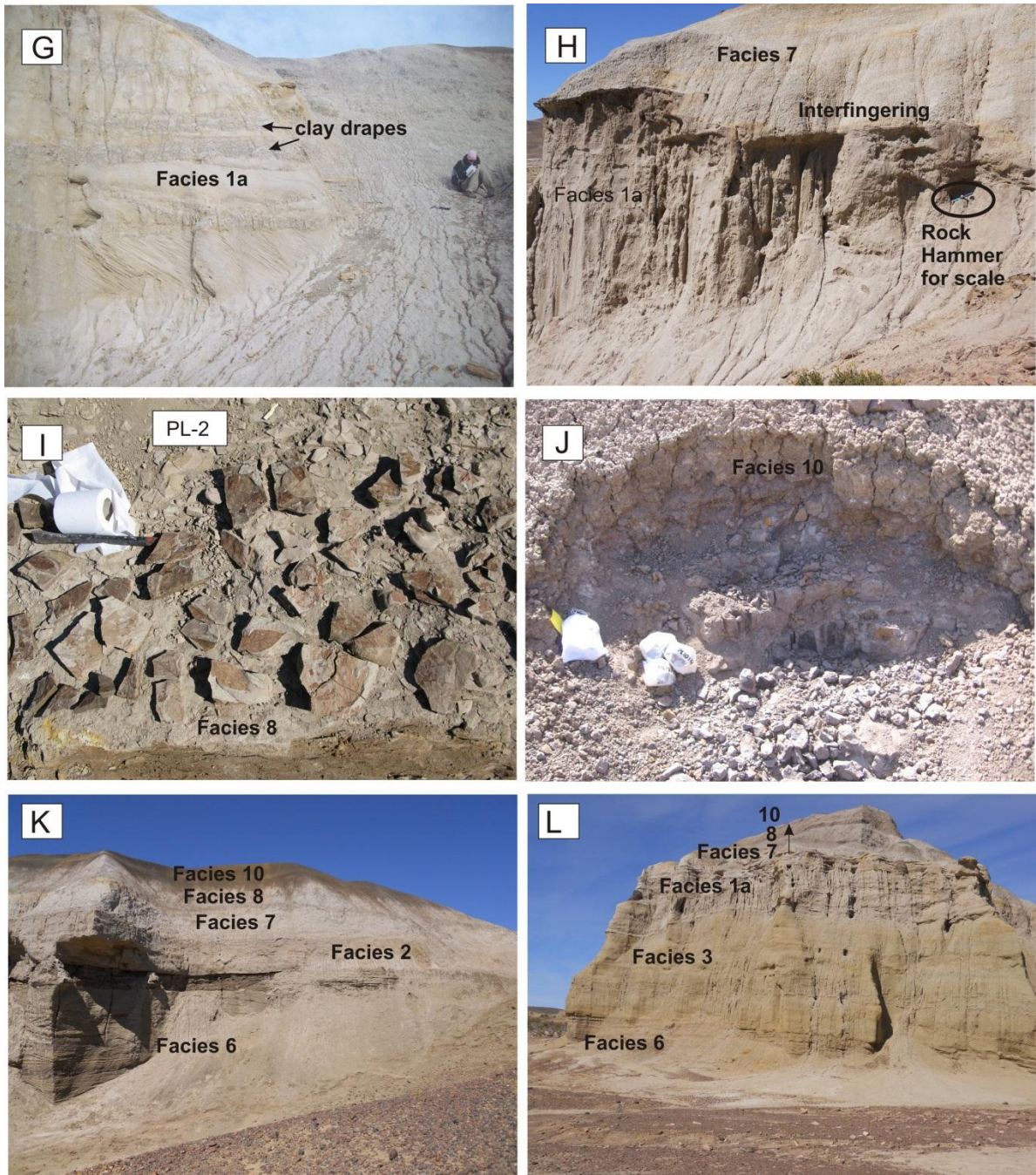


Fig. 8 A-J: Field photos detailing facies described in text: A) facies 5- transgressive sandy lag with pebbles, marine fossils, and cross beds at the base at Dromedary Hill, OR; B) facies 9- wispy bedded clay with burrows near the upper contact; C) facies 6- flaser, wavy, and lenticular rhythmic bedding at Abigarrado Hill, OR; D) facies 4- hummocky cross-stratification at OR; E) petrified stump from PL; F) facies 1b- unidirectional cross-bedded sands lying conformably within facies 1a- coarse grained trough cross-bedded sands; G) clay drapes within facies 1a; H) Interfingering between facies 1a and facies 7- accretion-bedded silts; I) PL-2 locality and plant fossils within; J) mottling within facies 8- transitional sands and silts; K) Outcrop of facies 2- plane parallel-laminated sands unconformably overlying facies 6; L) Outcrop photo at Palacio de los Loros showing the progression of facies 6, 3 (heterolithic sands), 1a, 7, 8, and 10 (black muds of the BNI)



### ***Facies 1a: White cross-bedded sands***

**Description.**--- Facies 1a consists of moderately sorted (fL-cU), poorly cemented, white litharenite (Fig. 8 D, E, F, G, H). The grain size distribution is unimodal with a median grain size of 704  $\mu\text{m}$ , corresponding to cL sand. Quartz grains are angular to subangular. Facies 1a contains the highest quartz fraction of any collected sample with 60% quartz, 10% feldspar, and 30% lithic grains. Sedimentary structures include trough cross-beds in bedsets ranging from 0.5-3 m in thickness.

Paleocurrent data were taken from trough cross-beds and petrified trunks within this facies at PL and OR (Appendix F). Rose diagrams indicate bimodal to polymodal current directions (Fig. 9). This assertion was tested using a uniformity test created for directional data (Swan and Sandilands 1995). This test uses the equation:

$$x^2 = \left(\frac{1}{E}\right) \sum (O - E)^2$$

$$E = n/k$$

where  $n$  is number of samples,  $k$  is number of bins, and  $O$  is the number of datum points per bin. Paleocurrent data from PL, OR, and the combination of the two are not uniformly distributed at the 95% confidence interval. Paleocurrents from PL and OR cluster in the NW and SW quadrants.

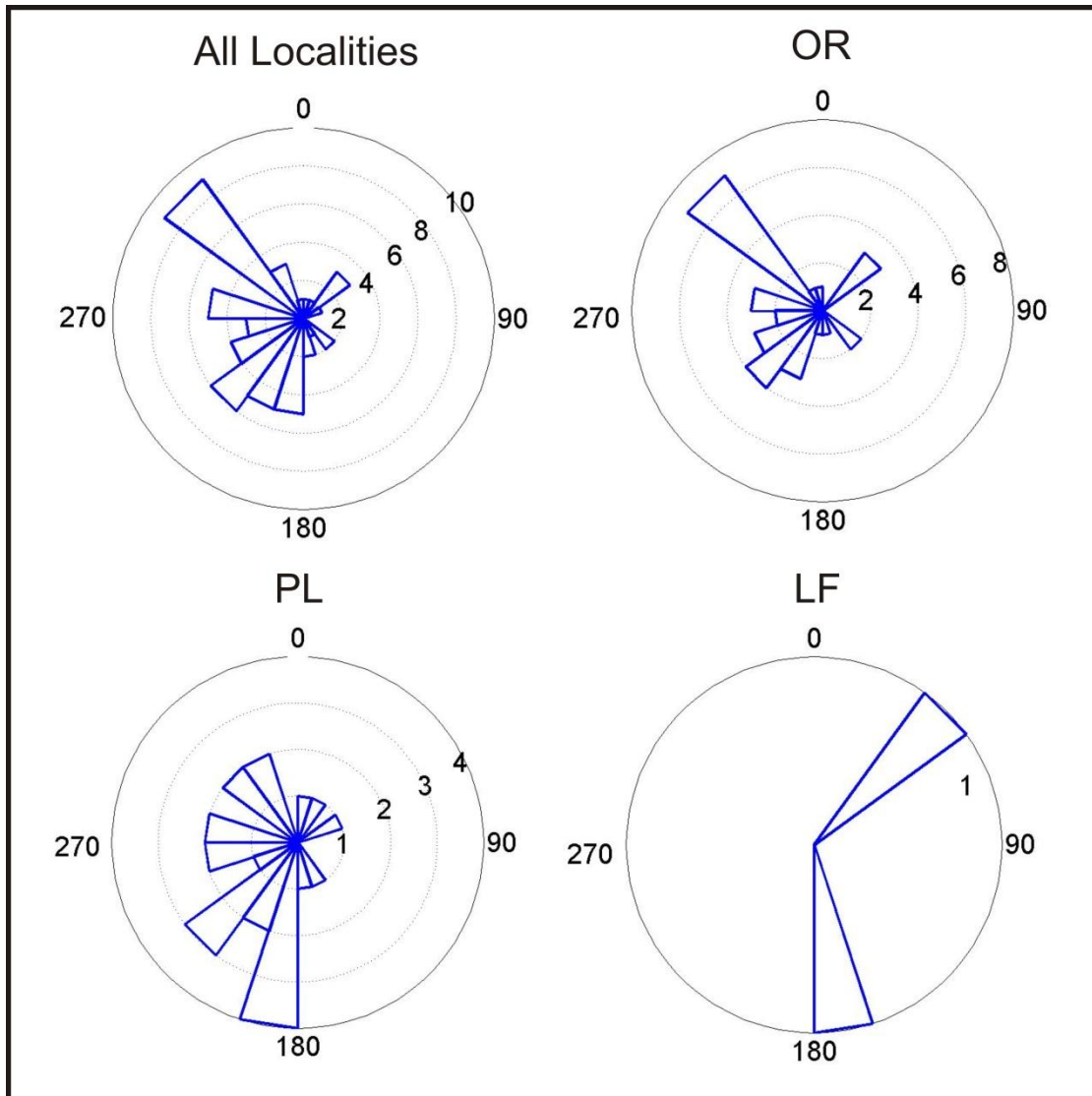


Fig. 9: Rose diagrams showing paleocurrent directions at all localities together as well as individual localities PL, OR, and LF (for raw data see Appendix F). These rose diagrams do not indicate any dominant direction, but when combined, data from all localities clusters to the E and WSW. Zero degrees is to the North.

Facies 1a lies unconformably over facies 3. The upper boundary is transitional and numerous outcrops show interfingering with the overlying fine-grained facies (Fig. 8H). Clay drapes of 10-50 cm thickness are deposited on cross-bed foresets at Palacio de los Loros. Petrified logs are common within facies 1a (Fig. 8E) and plant fossil localities often occur the below the base of this facies as well as above the upper

contact of this facies. Facies 1a is present at PL, OR, and LF and is extremely variable in thickness ranging from 3-24 m.

**Interpretation.**--- Average flow velocities needed to entrain grains of this size over a bed of large dunes range from 0.4 m/s to 1.5 m/s (Leeder 1999). Water depth can be estimated from dune height by assuming that approximately 1/3 of the duneslip face is preserved in cross-strata (Leclair 2002), and dune height is approximately one-fifth of the water depth (Leeder 1999). Average cross bed thickness in this facies ranges from 1-2 m, thereby corresponding to a total dune height of 3-6 m and a water depth of 15-30 m. Consequently, this facies is interpreted to represent elongate sand bars deposited in deep tidal channels near the headwaters of a tide-dominated estuary. Tidal bars aide in dissipating marine wave energy up the estuary (Darlymple 1990) and this facies is interpreted to be strongly influenced by tidal and fluvial flows but not waves. Therefore tidal channels are thought to be in the proximal region of the paleo-SJB estuary. Non-uniform distribution of paleocurrent directions indicates that two or more current directions dominate, further supporting the evidence of tides.

Only the uppermost sediments of this facies preserve mud drapes (Fig. 8G). This is consistent with modern tidal bars where a lower zone of high energy prevents preservation of fines (Darlymple 1992). Mud drapes in upper portions of facies 1a indicate a vertical decrease of flow strength as might be expected on tidal bars adjacent to a tidal channel. Interfingering at the upper contact with facies 7 suggests that facies 7 and facies 1a are time transgressive and represent a rapid change in depositional environment. Brea et al. (2008) describe stumps within facies 1a as parautochthonous due to the excellent state of preservation of stumps however sedimentological analysis

in this study suggests the stumps are allochthonous.

### ***Facies 1b: Unidirectional cross-bedded sands***

**Description.**--- Facies 1b is a moderately sorted, poorly cemented tan-white litharenite composed of vcU angular grains and 30% lithics (estimated by hand lens). Sedimentary structures are unidirectional, south-dipping ( $185^{\circ}$ ), high angle cross-strata of 5-10 cm thickness within horizontal beds ranging from 2-10 m. Beds contain occasional superimposed smaller-scale cross-strata dipping southwest. Facies 1b is only found in Palacio de los Loros, lies conformably within facies 1a, and is 2-3 m in thickness (Fig. 8F).

**Interpretation.**--- This subfacies represents runoff microdeltas created by late ebb currents during low tide and likely infills scours created in facies 1a (Dalrymple et al. 1990). This facies arises from short-lived local events and does not represent any significant change in environment.

### ***Facies 2: Plane-Parallel Laminated Sands***

**Description.**--- Facies 2 is a very poorly sorted, cL white litharenite composed of 30% lithics (observed by hand lens) with angular quartz grains (Fig. 8K). This facies displays low angle plane-parallel laminations dipping west in bed sets of 10-20 cm. Steeply dipping, unidirectional cross-strata in 1-3 cm. thick beds occasionally occur within these bed sets. The lower contact of facies 2 is an erosional unconformity into facies 6 and its upper contact is sharp and defines the base of facies 8. Facies 2 is only seen in outcrop at OR and has a thickness of approximately 2 m.

**Interpretation.**--- Where present, facies 2 lies in the same stratigraphic location as facies 1a, and replaces it. Dalrymple et al. (1992) describe upper flow regime sand

flats as common features just seaward of the tide-dominated fluvial reach of an estuary. These plane-parallel laminated sandflats lie within the tidal energy maximum of the headwaters (Dalrymple et al. 1990) and it is likely that this high energy environment eroded the underlying deposits of facies 1a.

### ***Facies 3: Heterolithic Cross-Bedded Sands***

**Description.**--- Facies 3 is a moderately sorted, moderately to well-cemented litharenite consisting of 91% framework grains (Fig. 8L). The grain size distribution is bimodal with a median grain size of 156  $\mu\text{m}$ , corresponding to fL sand. Sand composition consists of 43% quartz, 13% feldspar, and 44% lithic grains. Glauconite, grouped with the lithics, is abundant and comprises almost 11% of the entire mineral assemblage. TOC values in this facies range from 0.1-0.17%. This facies is trough cross-stratified in 10-20 cm thick bedsets with sparse silt interbeds 1-2 cm thick. Facies 3 contains plant hash, 0.5 - 1 cm mud rip-up clasts, and is bounded below by a sharp contact and above by an erosive contact. This facies is occasionally succeeded by accretion sets and laminated silts (facies 7 and 8) and macrofossil plant localities lie within these 20-80 cm silt beds. Facies 3 occurs at OR and PL and lies unconformably below facies 1a with thicknesses ranging from 4-12 m. A similar facies is present in RG but this facies is composed of low angle cross-strata rather than trough cross-bedding.

**Interpretation.**--- Facies 3 is interpreted as subtidal bars on a sand shoal that contains mutually evasive tidal channels. Tidal influence is evident in bi-directional trough cross-beds, mud drapes within cross-bed foresets, and heterolithic facies. Tidal channels are evident at the top of this facies in some localities (OR-1 and PL-1) as identified by accretion sets (facies 7). If the glauconite within this sand shoal is not

recycled from adjacent strata, it must be an estuarine mouth shoal nearer to the marine source, similar to the sand shoals at the mouth of the Chesapeake Bay, U.S.A.

Macrofossil localities within this facies lie in the upper meter. Sedimentologic evidence such as accretion sets and laminated silts within and directly above this facies indicate a unit of lower energy such as an intertidal bar top or tidal flat. If true, this facies represents a shallowing-upward cycle in which the upper few meters were deposited in abandoned intertidal channels proximal to a lowland forest or swamp.

Glauconite is an important element in this facies and provides a potential source for future potassium mining (Castro 2008). Glaucony facies are representative of open marine environments experiencing low sedimentation rates within depths of 60-550 m (Odin and Fullagar 1988). Low latitudes are generally more favorable to the formation of glauconite minerals but there are many documented glaucony facies in colder, higher latitudes (Odin and Fullagar 1988). The K-T transgression is a likely reason for the formation of glaucony facies in the Salamanca Fm. as it caused coastal areas to be flooded and to experience water depths greater than 60 m where grains are able to undergo the transition to glauconite minerals. It is likely that these glauconite minerals were reworked into facies 3 through storm events.

#### ***Facies 4: Swaley-Hummocky Cross-Bedded Sands***

**Description.**--- Facies 4 consists of a fU, poorly sorted (vfU-mL), poorly cemented litharenite. Its grains are subangular. Facies 4 exhibits large scale swaley and hummocky cross-bedding (Fig. 8D) in bedsets of .5 - 1m. This facies is highly variable in thickness and in the Dromedary Hill section thickens from 2.4 - 9.4 m over a few meters laterally. This facies was only documented in two areas within Ormachea Park

and interfingers with facies 3 and 6 where present.

**Interpretation.**--- Hummocky and swaley beds are signs of storm deposits, indicating that this facies was formed in water depths above storm wave base. Facies 4 mirrors the composition of the facies with which it interfingers. Therefore, facies 4 is interpreted to have formed in the same system of tidal bars and tidal channels that created facies 3 and 6 but was later reworked by storm waves.

### ***Facies 5: Poorly Sorted Litharenites and Clays***

**Description.**--- Point counting of grain size and mineral composition identifies facies 5 as a poorly sorted (fL-cU), poorly to moderately quartz-cemented, dusky yellow gray litharenite with a median grain size of 272  $\mu\text{m}$  corresponding to mL sand, although the grain size distribution is polymodal. In places facies 5 is slightly gravelly. Framework grains make up 93% of the sand beds and consist of 52% quartz, 12% feldspar, and 36% lithic fragments. Quartz is dominantly subangular. Total Organic Carbon values in this facies are  $\leq 0.1\%$ .

Sand bodies of facies 5 are tabular bodies about 1 m thick (Fig. 8A). Each sand body is bounded on the top by a sharp erosive surface, and surrounded by 0.5-2 m clay intervals. The first sand package of this facies usually contains cross-strata dipping at angles of 15-25<sup>0</sup> while succeeding sand bodies are massive. Individual cross beds are .5-1 cm thick within 10-20 cm thick bedsets. These sands contain phosphatic nodules, plant hash within mud drapes, shark teeth, marine shell fossils, and 1-3 cm clay rip-up clasts. Some units also contain 0.5-2 cm white sand-filled burrows. Facies 5 only occurs at OR and comprises the first 4 m of the Salamanca Fm. directly above the unconformity between Cretaceous and early Paleocene sediments.

**Interpretation.**--- This facies is interpreted to be a transgressive lag deposit above a marine flooding surface. The multiple sand bodies interrupted by clay intervals are interpreted as a transgressive systems tract produced by retrogradation of the shoreline and shoreface. Alternations between clay and sand beds are common in tide-dominated estuaries where partial transgressions are preserved seaward of a highstand shoreline (Darlymple et al. 1992). Tidal influence is evident in the mud drapes on cross bed foresets and a marine origin is indicated by shark teeth fossils.

### ***Facies 6: Wavy-Bedded Sands and Silts***

**Description.**--- Facies 6 consists of alternating sand-silt beds ranging in thickness from 1-5 cm (Fig. 8C) composed of grain sizes from vf sand to silt. The sand beds are moderately sorted, poorly cemented, composed of 49% framework grains, and 51% silt sized grains. This facies lies within the textural group silt and has a unimodal grain size distribution with a median grain size of 59  $\mu\text{m}$ . The mineral assemblage of the sand within this facies is 48% quartz, 13% feldspar, and 39% lithics and with glauconite grains comprising about 10% of the total mineral assemblage. Some intervals are wavy-bedded with 1-2.5 cm thick silt layers intercalated with 1-5 cm thick sandy silt beds. In some localities these wavy bedsets alternate with wave ripple cross-laminated bedsets. Wave ripple lamination sets are of 10-30 cm thick. Some localities display convolute bedding. Everywhere the facies contains abundant plant hash, and glauconite increases upsection.

Facies 6 occurs within OR and PL in 2-4 m packages. The base of this facies is not always visible in outcrop but facies 6 is consistently found underlying facies 3. A similar facies occurs within the Rancho Grande locality but this facies does not have a



rhythmic alternation of beds, is much siltier, and contains abundant plant fossils as well as some starfish fossils.

**Interpretation.**--- This facies is representative of the deeper water deposits of a tidal estuary and mirrors deposits described by Zhang and Zhang (2006). Flaser, wavy, and lenticular bedding are also common in tidal flat settings but tidal flat laminations are commonly thinner, muddier, and are only preserved in intertidal zones (Dalrymple et al. 1990, Choi et al. 2004). The rhythmic alternations in facies 6 are evidence of a tidal setting with coarser-grained beds deposited during tidal flows and fine-grained beds deposited during slackwater. Thinner beds represent neap tides and thicker beds represent spring tides (e.g. Shanmugam et al. 2000). High glauconite content and wave-rippled laminations imply a strong marine influence; thus these facies likely lie near the seaward limit of tidally influenced sediments.

Though the facies at RG are similar, the beds there are not rhythmic and wave ripples are more common, implying that RG deposits are dominated by wave rather than tidal forces. Higher silt content and preservation of delicate flower, leaf, and invertebrate fossils indicate a low-energy brackish to saltwater environment. It is likely that this facies represents a sheltered or offshore environment.

### ***Facies 7: Accretion-Bedded Sands and Silts***

**Description.**--- Facies 7 consists of moderately well sorted homogeneous light gray sands and silts with a bimodal distribution of grain sizes and median size of 85  $\mu\text{m}$  corresponding to vL sand (Fig. 8 D, F, H, K, L). Framework grains make up 85% of the sediment and are composed of 42% quartz, 10% feldspar, and 48% lithic grains. The quartz grains are subrounded. TOC values in this facies are less than 0.1%. This facies

is 0.5-3 m thick and consists of 10-20 cm heterolithic inclined strata dipping 10-15°. The base of facies 7 generally interfingers with various underlying facies and the upper contact is transitional. This facies occurs in two stratigraphic positions- above facies 1a at PL and OR and above facies 3 at PL. Plant deposits are found within and above this facies.

**Interpretation.**--- Inclined heterolithic cross-strata are commonly described as lateral accretion beds of point bars (Nouidar and Chellaï 2001, Crerar and Arnott 2007). The occurrence of facies 7 above facies 1a defines a shallowing-upward sequence from subtidal channel deposits to intertidal point-bar accretion beds. Based on the interbedded fine sand and mud component, this facies is interpreted as an abandoned tidal channel fill (Willis and Tang 2010). Facies 7 represents single point-bar deposits as opposed to amalgamated deposits based on a thickness of < 5 m, unidirectional dips within one succession, and a lack of erosional surfaces within the facies (Crerar and Arnott 2007). Thickness and silt content suggest that this facies was deposited in a lower energy setting (Crerar and Arnott 2007). A lower energy setting is also supported by the well preserved plant deposits found above and within this facies.

The occurrence of facies 7 with facies 3 indicates deposits of a small tidal channel in a low-energy intertidal environment. The large scale deposits above facies 1a at PL represent final stages of infilling in the estuary as this facies is succeeded by low energy tidal flats and abandoned channel fill. From the thickness of the point bar, channel width can be roughly estimated based on the equation:

$$w = 6.8h^{1.54}$$

where  $h$  represents thickness (Leeder 1973, Crerar and Arnott 2007). Given a point bar

thickness of 2-4 m and a dip of 10-15<sup>0</sup>, it is reasonable to assume the width of these tidal channels was on the order of 50-150 m.

### ***Facies 8: Transitional Sands to Silty Clays***

**Description.**--- Facies 8 is a poorly to moderately cemented lithic wacke interbedded with silty clay (Fig. 8 D, I, K, L). The sand is poorly to moderately sorted, with a median grain size of vf-fU, and is composed of 60-80% subrounded to rounded quartz grains (observed through hand lens). Fine laminations near its base give way upward to a mottled texture. Silty clay beds become more abundant upsection until the entire facies is composed of silty clays. The lower and upper contacts are transitional. The silty clay contains plant hash, mottling, and pedogenic slickensides. This facies is present in both PL and OR and lies above either facies 1a or facies 7. It ranges in thickness from 3-10 m.

X-ray diffraction of clays from facies 8 show important clay mineral peaks at 14, 10, and 7 angstroms that are identified as montmorillonite, illite/glaucanite, and halloysite respectively (Fig. 10, Appendix B). A large quartz peak at 26.6 Å is also present.

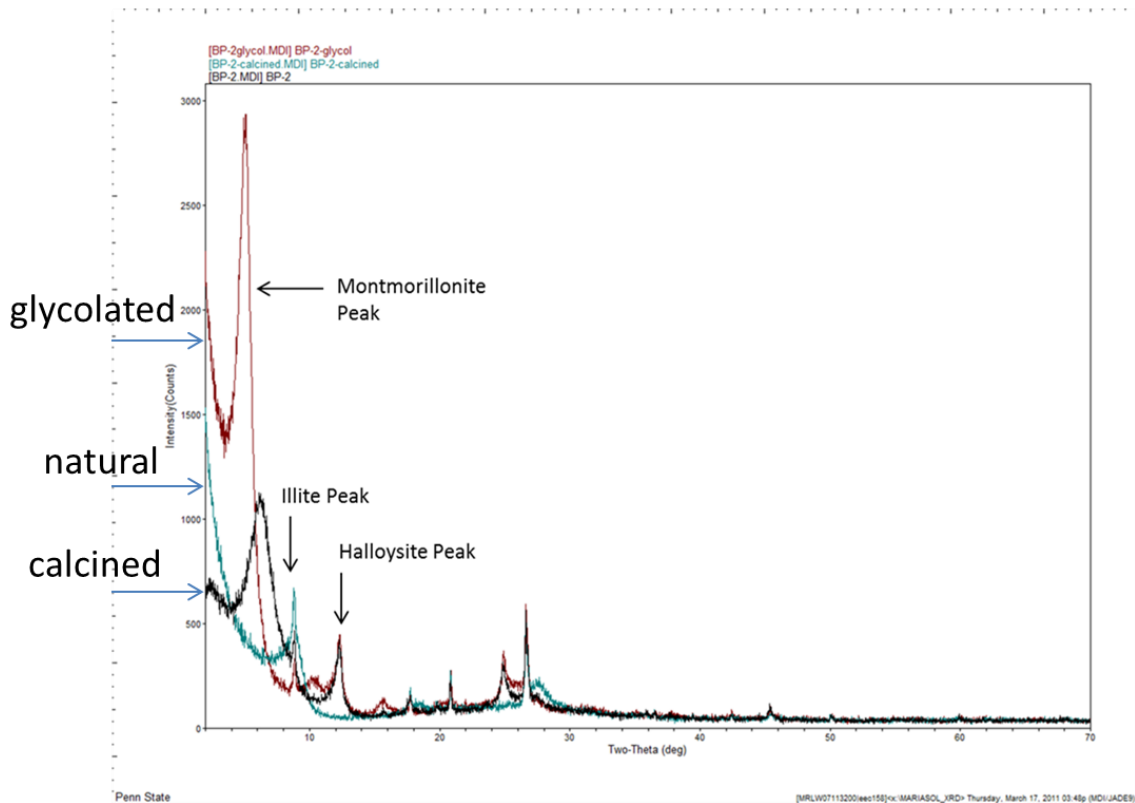


Fig. 10: XRD pattern from sample BP-2 (see Fig. 6 for stratigraphic location) showing the oriented, glycolated, and calcined sample diffraction patterns. Expansion and collapse of the montmorillonite peak are shown between 5-7  $\theta$ . The subdued illite/glaucanite peak appears at 8 $\theta$ . The halloysite clay peak occurs at 13  $\theta$  expands to 10  $\theta$  in the glycolated sample and is destroyed when calcined

The 14 Å peak was identified as smectite due to expansion when exposed to ethylene glycol and subsequent collapse when heated to 550° C for 2 hours. Smectitic clays with 14 Å peaks can be montmorillonite or vermiculite; however pattern fitting in MDI Jade showed montmorillonite to be the closest fit. The 14 Å peak possesses the highest intensity clay peak in all 20 samples- an intensity from 400-3000 counts with a width of approximately 2 Å. This pronounced peak suggests that the clay fraction of these samples is strongly dominated by montmorillonite.

The 10 Å peak did not change greatly when exposed to ethylene glycol or after being calcined. The most likely options for this peak are illite and glauconite and it is

likely that this peak represents a mixed layer containing both glauconite and illite. The 10 Å peak is not a pronounced peak and disappears stratigraphically upward into the larger 14 Å montmorillonite peak. The peak is much narrower than either the 14 or 7 Å peaks suggesting that this clay phase is not a major component of these samples.

The 7 Å peak identifies the presence of either kaolinite or halloysite. A peak at 8 Å that only appears after glycolation indicates expansion of the 7 Å peak and the presence of halloysite. Halloysite is a hydrated form of kaolinite. The two have almost identical XRD patterns and, with the exception of high water content in halloysite, chemical composition (Zhou et al. 2011). The similarity between these minerals suggests a presence of both kaolinite and halloysite in the samples.

A full chemical analysis of samples within this facies (Appendix C) shows that silicon dioxide is the most abundant element, comprising 50-70 % of the total oxides. Apart from SiO<sub>2</sub>, the only other major chemical constituents are Fe<sub>2</sub>O<sub>3</sub> and Al<sub>2</sub>O<sub>3</sub>. Iron Oxide follows a near linear relationship increasing with stratigraphic level (Fig. 11) whereas Aluminum Oxide correlates to coloration and the darkest samples, BP-11 and BP-13-INF, have the highest aluminum oxide values (Fig. 12). Manganese and sulfur, originally hypothesized to be important elements in this facies, are only present in trace amounts in these samples and show no correlation to color or stratigraphic position. Pyrite and gypsum, common minerals in sulfur-rich soil, were not seen in outcrop further supporting the results of the sulfur analysis and the conclusion that these samples contain little to no sulfur suggesting a dominantly non-marine environment.

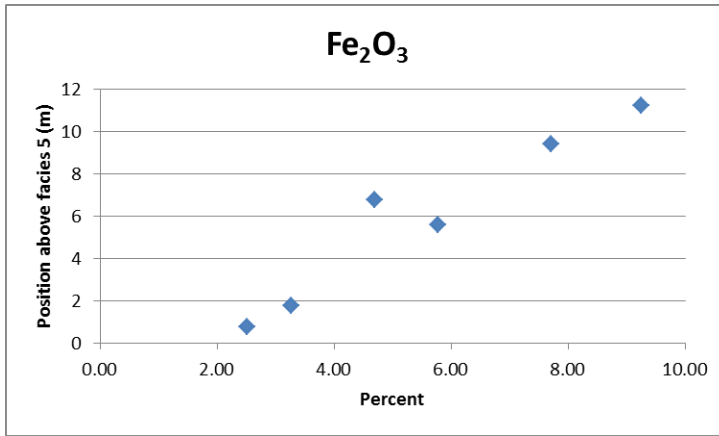


Fig. 11: Graph showing the near linear relationship between iron oxide and stratigraphic position.

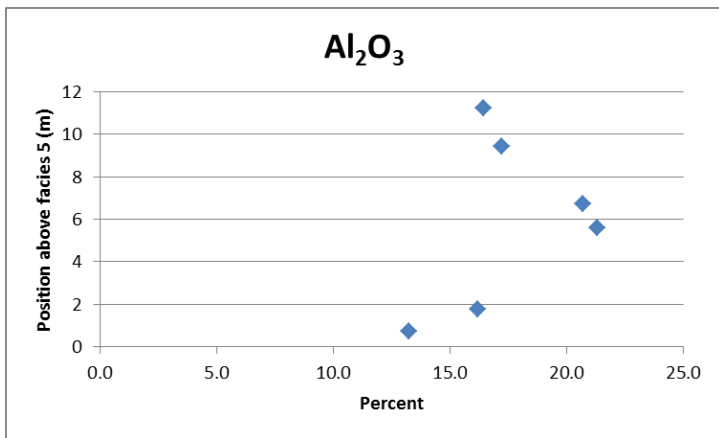


Fig. 12: Graph showing the relationship between aluminum oxide and stratigraphic position in the chemical analysis samples. The darkest samples (between 4-6 m stratigraphically) have the highest aluminum oxide content.

Samples from OR and PL were analyzed for Total Organic Carbon (TOC). TOC values in this facies range between 0.1 – 0.32 % and represent the highest TOC values of any facies.

**Interpretation.**--- Facies 8 represents the transition from a marine to a continental setting. Fine grain sizes and laminations indicate a very low energy environment and mottling is interpreted to result from wetting and drying in a warm to

temperate climate. This facies represents muddy tidal flats and a prograding lower coastal plain of the San Jorge estuary.

Facies 8 is dominated by the clay mineral montmorillonite, a clay mineral within the smectite group. Smectites are minerals containing weakly linked interlayers that commonly swell in the presence of water and collapse in the absence of water (Chamley 1989). Because of their susceptibility to collapse, smectites are not present in sediments that have experienced high temperatures and pressures as a result of deep burial or metamorphism (Borchardt 1989). They are found in areas that limit drainage and leaching such as poorly drained basins or landscape depressions in environments with a high water table, and little regional dip (Singer 1980, Borchardt 1989). Smectites are common clay minerals in sediments weathered from volcanic ashes and are the weathering product of mafic minerals such as pyroxene, olivine, hornblende, biotite, and augite (Borchardt 1989, Chamley 1989).

Due to its weak signal and inconsistency upsection, the 10 Å peak in samples of facies 8 most likely represents secondary alteration and illitization, the transformation of smectite into illite, or the presence of transported glauconite in the samples. Illitization occurs in stages and produces intermediate minerals such as mixed-layer illite/smectites that show a stronger presence of illite with increased depth of burial and temperature (Fanning et al. 1989). Zhou et al. identifies two stages of illitization; OR and PL sediments fall into the first category of medium diagenetic depth less than 2550.25 m and temperatures less than 100-110 C (Zhou et al. 2011). Conditions needed to produce ordered mixed-layer illite/smectite are similar to those produced in oil-generating rocks (Zhou et al. 2011). I interpret the illite in these samples as a product

of a burial in potassium- and aluminum-rich sediments. One method of adding potassium and aluminum is through wetting and drying cycles (Fanning et al. 1989). Mottled texture is present in some areas of facies 8 supporting the notion of wetting and drying cycles. Another explanation of the 10 Å peak is the presence of transported glauconite. Glauconite is abundant in lower facies 3, 4, and 6 and is a common mineral in marine influenced sediments. If this 10 Å peak represents glauconite, then the disappearance of this peak upsection indicates decreasing marine influence through time reinforcing the idea of estuarine infilling through progradation of continental facies.

The occurrence of kaolinite and halloysite in facies 8 samples also suggests a protolith of volcanic ash and rock fragments subjected to intense weathering (Singer 1980, Allen and Hajek 1989, Dixon 1989, Joussein et al. 2005). Halloysite represents an intermediate stage in the transition of smectite to kaolinite (Chamley 1989, Dixon 1989), a transformation that occurs when soils undergo leaching (Allen and Hajek 1989, Dixon 1989, Krause et al. 2010). I conclude that the halloysite/kaolinite clay phase in these sediments is the product of post depositional weathering, indicating a later change in environment to a highly leached, well-drained soil.

The clay mineralogy and internal fabric of facies 8 describe a gleysol according to the Mack (1993) paleosol classification system. These sediments become mottled and weathered upward and are classified as a vertisol in the top few meters of facies 8. Figure 6 illustrates the increasing mottling and alteration of sediments upsection. Gleysols arise under low redox conditions in waterlogged areas with high water tables during most of the year. Mottling can be present at the upper surface of gleysols where the soil undergoes periodic draining (Mack 1993). Vertisols describe soil profiles that



have undergone extensive pedoturbation usually as a result of shrinking and swelling smectitic clays. Slickensides are common morphologic features in vertisols (Mack 1993). Lower gleyed horizons represent sediments that have undergone little weathering. This is evident in both the gleyed character as well as the well-preserved macroflora fossils. Upsection, mottling intensifies indicating a more dynamic environment that experienced periods of wetting and drying.

As feldspars weather into clays, basic elements such as calcium, sodium, and potassium are depleted and replaced by aluminum. The Chemical Index of Alteration (CIA) is a proxy for the degree of weathering undergone because it uses the ratio of aluminum to alkali components using the formula:

$$\text{CIA} = [\text{Al}_2\text{O}_3 / (\text{Al}_2\text{O}_3 + \text{CaO} + \text{Na}_2\text{O} + \text{K}_2\text{O})] \times 100 \quad (\text{Nesbitt and Young 1982})$$

where weight percent values are converted to molecular proportions (White and Schiebout 2008). Figure 13 shows the relationship between CIA and stratigraphic position. All samples of this facies have CIA values between 75-85 % representing rocks that have been moderately to intensely weathered (White and Schiebout 2008). CIA values for montmorillonite and illite range between 75 – 85 % whereas kaolinite approaches 100 % (Nesbitt and Young 1982). Therefore, samples with higher CIA values also contain a larger abundance of kaolinite in relation to montmorillonite and illite. Results from this CIA analysis show that the lowest sample also has the lowest CIA value whereas the upper 5 samples have higher CIA values. This is the expected result as minimally weathered gleysols are replaced upward by vertisols. BP-13-INF has a significantly higher CIA value than the other samples indicating a larger degree of weathering at this stratigraphic level.

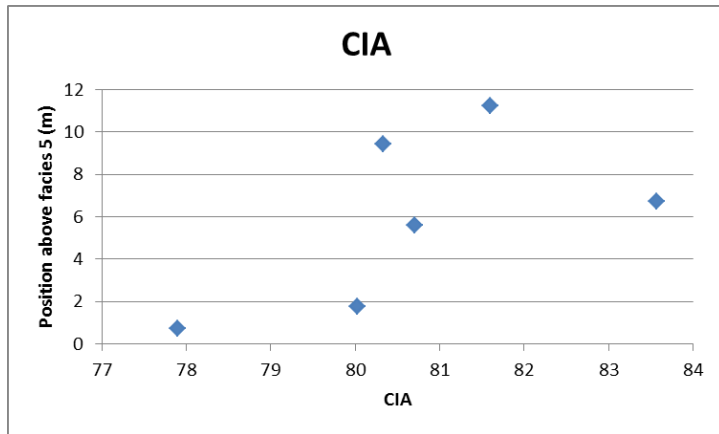


Fig. 13: Graph showing the CIA of chemical analysis samples. The lowest sample has a significantly lower CIA value whereas the other 5 samples have higher values. All samples ranging between 77-84 indicate a moderate to intense degree of weathering.

### ***Facies 9: Wispy Bedded Clays***

**Description.**--- Facies 9 consists of a finely laminated (1-3 mm) purplish gray clay interbedded with 1-3 cm long 1-4 mm thick sand wisps that decrease in number but increase in size up-section. The sand is vfU, light gray, litharenite. This facies typically is 3-4 m thick. Burrows are absent except for the upper 5 to 10 cm which contain 5 cm vertical U-shaped burrows (Fig. 8B). Plant hash is abundant with large (3 cm) intact leaves found in the upper section. Weathering features include iron oxide staining and gypsum formation. Facies 9 appears in outcrop at OR and comprises the 4 m above facies 5. It also occurs in the lower 4 m of RG.

**Interpretation.**--- Undisturbed laminations indicate a low energy environment but the lack of ichnofossils, suggests that this was a deeper water, possibly anoxic environment. These deposits are interpreted as shelf muds deposited below storm wave-base. The U-shaped dwelling structures in the upper few cm of this facies indicate shallowing upward and the change to an oxic habitable environment.

### ***Facies 10: Brownish Black Muds (Banco Negro Inferior)***

**Description.**--- Facies 10 is a mottled brownish black mud with pedogenic slickensides, iron nodules, rhizoliths, and other root traces (Fig. 8 J, K, L). It makes up the Banco Negro Inferior Fm. (BNI). Clay mineralogy mirrors facies 8 but montmorillonite becomes even more abundant and illite is no longer resolvable. TOC values within this facies range between 0.1- 0.26 %. Its basal contact is transitional and its upper contact is an erosional unconformity at the base of the Peñas Coloradas Fm. of the Rio Chico Group. Facies 10 is generally tabular but is occasionally removed by erosion. Facies 10 is found in PL and OR, where it is 1-2 m thick.

**Interpretation.**--- Facies 10 represents a slowly prograding, widespread coastal-plain swamp experiencing a low rate of sediment supply. The BNI is described as a swamp in earlier literature (Feruglio 1949, Marshall et al. 1981, 1997) due to the presence of mammal, turtle, and crocodile fossils. Facies 10 is an important marker bed throughout the San Jorge Basin and has been described in outcrops from PL and OR to the east at Punta Peligro on the Atlantic coast (Feruglio 1949). This bed is important because it overlies the Salamanca Fm. and provides an easily identifiable datum for the contact between the Salamanca Fm. and the Rio Chico Group.

The BNI is distinctive because of its dark coloration. The darker color is not due to higher carbon, manganese, or sulfur values as indicated by TOC, sulfur analysis, and chemical analysis. The darkest samples contain the highest aluminum content and the lowest intensity montmorillonite in relation to halloysite. The chemical formula for halloysite is  $Al_2Si_2O_5(OH)_4$  whereas the chemical formula for montmorillonite is  $Na_{0.33}(Al_{1.67}Mg_{0.33})Si_4O_{10}(OH)_2$  (Chamley 1989), suggesting higher halloysite

content in aluminum-rich rocks. Thus, the cause for dark coloration in the BNI is high aluminum content and possibly higher halloysite content. It is common to find black paleosols, such as the Banco Negro Inferior, just above weathered basalts in landscape depressions so it is also possible that facies 10 is influenced by volcanic sediments (Borchardt 1989).

Abundant mottling, gray coloration, dominance of smectite, and slickensides identify this paleosol as a vertisol similar to upper deposits of facies 8. This is indicative of a waterlogged environment in which the soil underwent periodic wetting and drying cycles. Halloysite and high CIA values indicate post-depositional weathering.

Similar black paleosols occur in Paleocene sediments of Texas with slickensides, low TOC values (0-2%), rare carbonate nodules, and a clay mineral fraction dominated by smectite with a lesser kaolinite presence. White and Schiebout (2008) also concluded that these paleosols were formed in a waterlogged environment that underwent periodic drying (White and Schiebout 2008).

### ***Facies Associations***

The Salamanca and Banco Negro Fms. in the study area consist of two sequences defined by erosional unconformities at the bases of facies 5, and 1a and at the top of facies 10 (Figs. 14, 15, 16).

The lag deposits of facies 5 represent the transgressive systems tract (TST) and the flooding of underlying, Cretaceous continental facies. The erosional marine flooding surface (mfs) lies at the erosional unconformity between Cretaceous and Paleocene sediments and the maximum marine flooding surface (mmfs) lies at the top of TST. The

erosional marine flooding surface also represents the first sequence boundary (SB 1). The marine shelf muds of facies 9 and inner shelf muds of facies 3 and 4 represent a highstand systems tract (HST) deposited during progradation of the shoreline as sediment influx to the basin overwhelms the rate of creation of accommodation space. Facies 3 is bounded above by an erosional unconformity signifying the second sequence boundary (SB 2).

Facies 1a, 1b, 2, 7, 8, 9, and 10 represent the lowstand systems tract (LST), beginning with the scours of deep tidal channels at the base of facies 1a and the subsequent abandonment and infilling of these channels. The final stage in this overall progradation and estuarine infilling is the encroachment of a widespread coastal swamp containing a diverse, lowland, population of plant species. This coastal swamp is the source of transported macroflora fossils found in the upper deposits of the Salamanca Fm. Facies 1a, 1b, 2, 7, 8, 9, and 10 are considered as part of the LST. These are considered a LST rather than a continuation of the HST because accretion sets, laminated silts, and plant preservation overlie facies 3 in some areas, indicating a period of infilling at the end of the HST. It is unlikely that the channel scours of facies 1a were able to form during a stage of infilling without a drop in eustatic sea level.

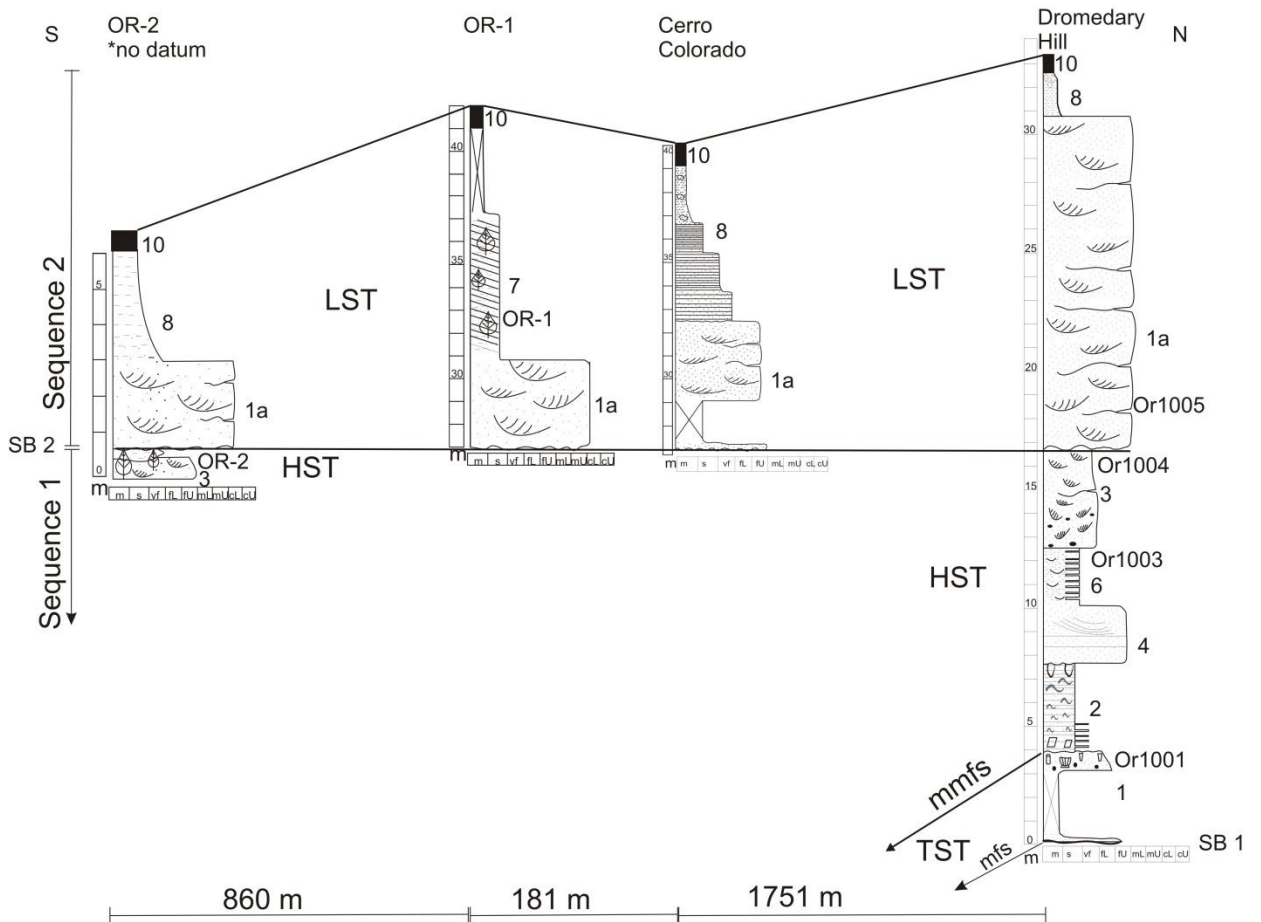


Fig. 14: Correlation diagram showing the sequence stratigraphy among measured sections at OR (Fig. 4). With the exception of the Dromedary Hill section, only the LST and top of the HST are exposed in outcrop. See Fig. 16 for other details.

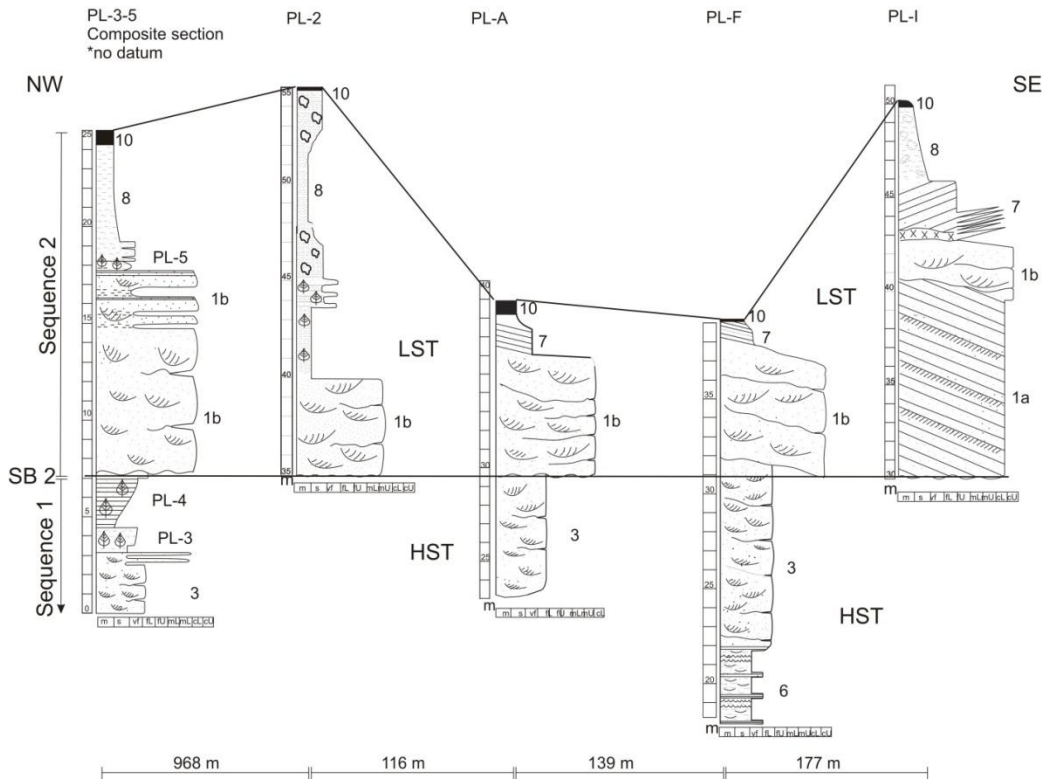


Fig. 15A

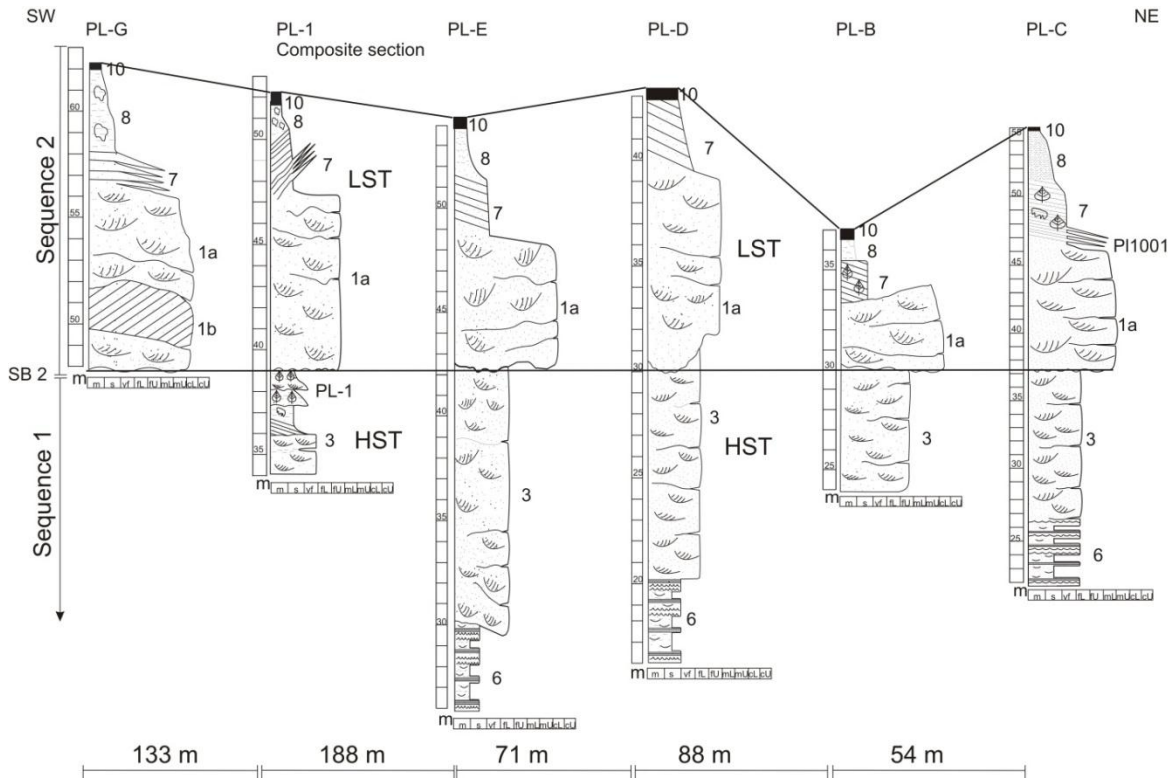


Fig. 15B

Fig. 15A,B: Correlation diagram showing the sequence stratigraphy among measured sections at PL (Fig. 3). Spacing is not relative to distance between localities. See Fig. 16 for details.

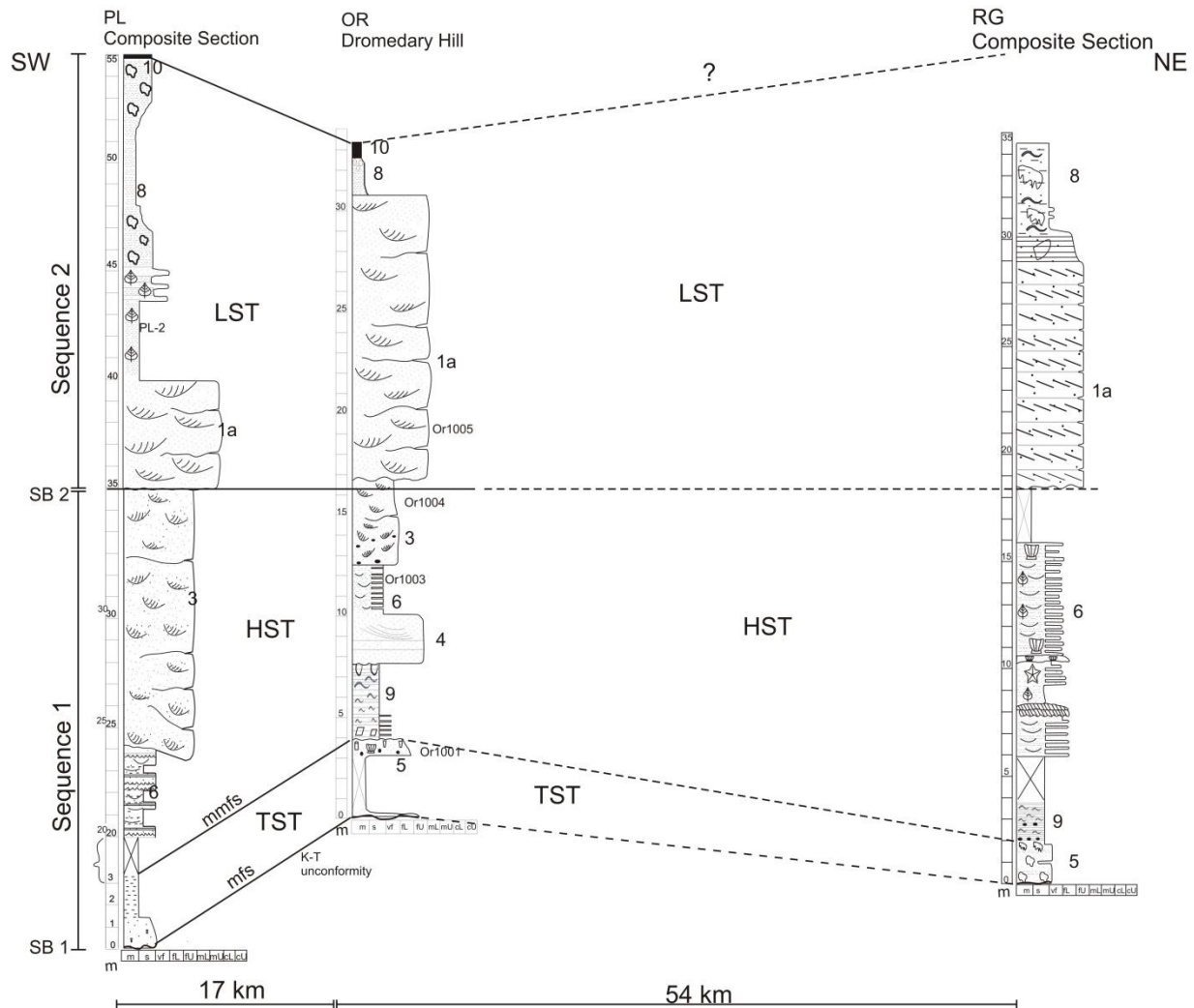


Fig. 16: Correlation diagram showing the sequence stratigraphy between PL, OR, and RG. Facies are indicated by number, also shown are sample locations and plant localities. Spacing is relative to distance. Dotted lines between OR and RG columns represents uncertainty because the RG locality could not be correlated to either the basal unconformity or facies 10. Two sequences are represented by these strat columns. The first sequence begins with a transgressive systems tract (TST) overlain by a highstand systems tract (HST). This first sequence is overlain by an erosional unconformity succeeded by 15-20 m of lowstand systems tract (LST) deposits representing sequence 2. The marine flooding surface (mfs) lies at the base of the TST and the maximum marine flooding surface (mmfs) lies at the top of the TST. Datum is erosion at base of facies 1a (see Fig. 1 for locations). Legend is in Appendix A.



## SAND PETROGRAPHY

The sands of the Salamanca Fm. in the study area range between feldspathic litharenite and litharenite (Fig. 17). Differences among sample localities are evident when provenance distinctions are drawn using Dickinson classification diagrams (Figs. 18, 19) (Dickinson et al. 1983). Samples from OR and PL lie within the recycled orogen provenance in both classification systems (Dickinson et al. 1983). Due to their intermediate quartz content, high sedimentary lithic content, and low carbonate, volcanic, and feldspar content, I conclude that these OR and PL facies were derived from a collision orogen (e.g. Boggs 1992). Quartz grains from these localities dominantly show straight extinction and metamorphic lithics are rare, implying that these sediments come from a plutonic rather than a strongly metamorphosed and tectonically complex area. The North Patagonian batholith is a likely source terrain for these plutonic sediments. This batholith is part of the larger Patagonian batholith which is approximately 200 km wide, extends between 40-53° S latitude, and formed episodically from the Late Jurassic through the Late Cenozoic (Pankhurst et al. 1999). The section of this batholith that formed during the Mid-Cretaceous is the mostly likely source of material. This area lies at the eastern edge of the batholith, about 250 km from the field area, and covers a great area N-S (Pankhurst et al. 1999). Subduction of the Nazca plate and formation of the Andes began as early as the Late Cretaceous (Uliana and Biddle 1988, Folguera et al. 2011) and this late Cretaceous uplift may have led to the exposure of the North Patagonian batholith.

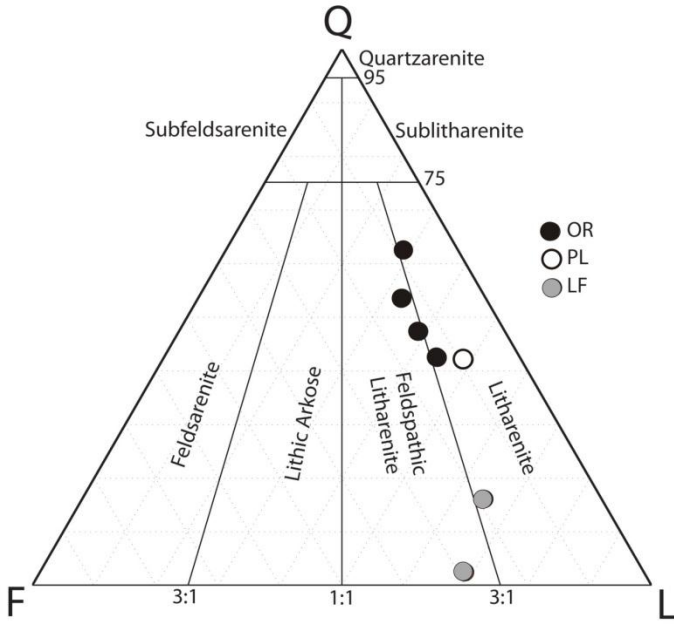


Fig. 17: QFL diagram based on the Folk (1970) classification system. All petrography samples cluster within the litharenite and feldspathic litharenite categories

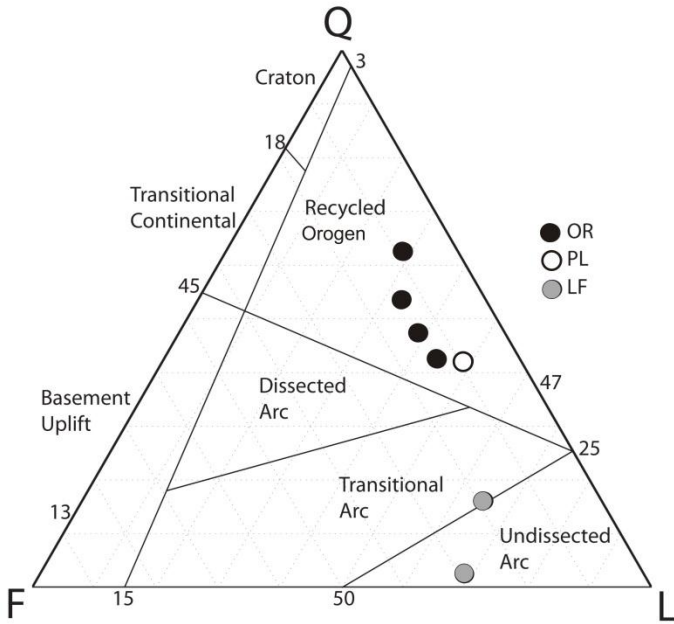


Fig. 18: QFL diagram based on the Dickinson (1983) classification system. PL and OR samples lie within the recycled orogen whereas LF samples lie within the undissected arc orogen

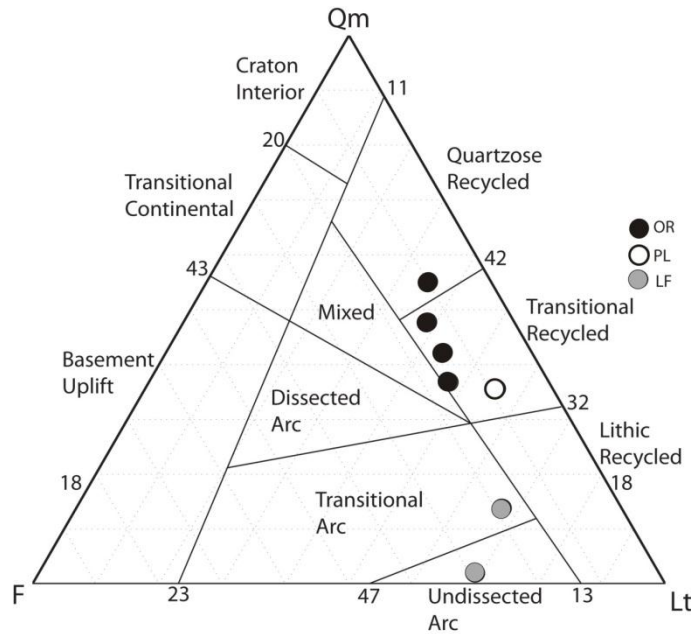


Fig. 19: QmFLt diagram based on the Dickinson (1983) classification system. PL and OR samples lie within the recycled orogen whereas LF samples lie within the undissected arc and transitional arc orogens

The sands just above the Las Flores (LF) plant locality contain few sedimentary lithics, abundant feldspar, and approximately 50% volcanic lithics with the majority being lathwork volcanics, placing LF samples in the undissected to transitional magmatic arc category. Although grain size exerts a strong effect on sand composition, there is no obvious relationship between grain size and lithic content in these samples (Fig. 20). Thus, the LF sediments were almost certainly derived from a volcanic source terrain. These LF sands are within the younger Peñas Coloradas Fm. of the Rio Chico Group causing the difference in petrography between LF and OR/PL sands. The San Bernardo fold belt is a possible source terrain because it has been subject to uplift and magmatism as early as the Late Cretaceous and it is the nearest volcanic source to LF (Folguera et al. 2011).

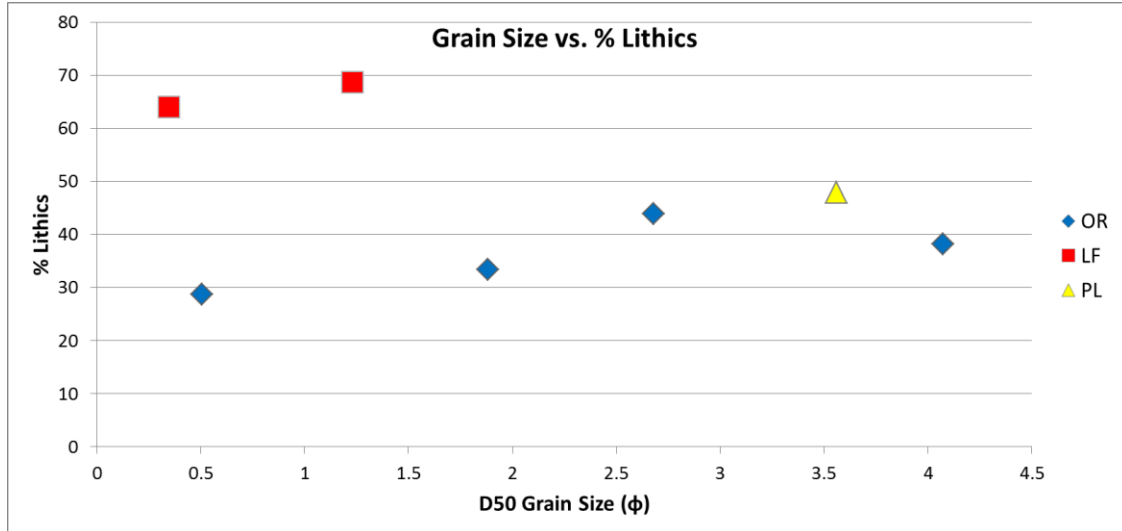


Fig. 20: Graph showing the mean grain size vs. lithic content of the seven samples used for the petrographic analysis. This graph shows no relationship between grain size and percent lithics possibly indicating that increased lithic content in the LF localities is the result of real differences in provenance rather than a bias due to higher mean grain sizes.

Previous petrographic work has been conducted in both the Peñas Coloradas Fm. of the Rio Chico Group (Raigemborn 2006) as well as the Cretaceous Bajo Barreal Fm. (Umanzo et. al 2009). Three sites were analyzed in the Peñas Coloradas Fm. concentrating on outcrops 100-150 km east of this study area. Results from the Peñas Coloradas Fm. indicate a dissected to transitional magmatic arc provenance, with progressive unroofing of batholithic rocks, similar to Peñas Coloradas samples at LF (Raigemborn 2006).

Petrography of the subjacent Bajo Barreal Fm. was studied by Umanzo et al. (2009) in fluvial facies at two sites bordering the San Bernardo Range 35-75 km west and northwest of OR and PL. They classified the sands as litharenite and felsic litharenite (Umanzo et al. 2009), but unlike the Salamanca Fm., these samples show a strong magmatic signature of a transitional to undissected arc. QFL plots most closely resemble QFL values in the Las Flores locality and it is possible that LF sands are

composed of reworked volcanic lithics of the older Bajo Barreal Fm. Classification of Bajo Barreal sediments place this terrain in an undissected transitional arc, and compositional evidence suggests a provenance of the volcanic Divisadero Formation (Umanzo et al. 2009). Thus, the Salamanca sands at PL and OR do not represent much reworking of the subjacent strata below its basal transgressive unconformity.

Petrography of modern sediments from the entirety of South America cluster into five groups; Brazilian, Caribbean, Transitional, Argentine, and Pacific (Potter 1994). Paleocene sediments (from PL and OR) have a much higher quartz content and much lower feldspar content and in general a much lower volcanic lithic content than modern Argentine sediments.

### **BASIN ANALYSIS**

Regional distribution of facies within the Salamanca Fm. was explored using resistivity wireline logs. First, resistivity patterns were correlated to facies described in the literature (Feruglio 1949, Lesta 1968). Standard oil company correlation for the Salamanca Fm. uses Feruglio's facies (Fig. 21); however, these facies change regionally and wireline logs near the PL and OR outcrops more closely resemble facies described in this study (Fig. 22).

T74

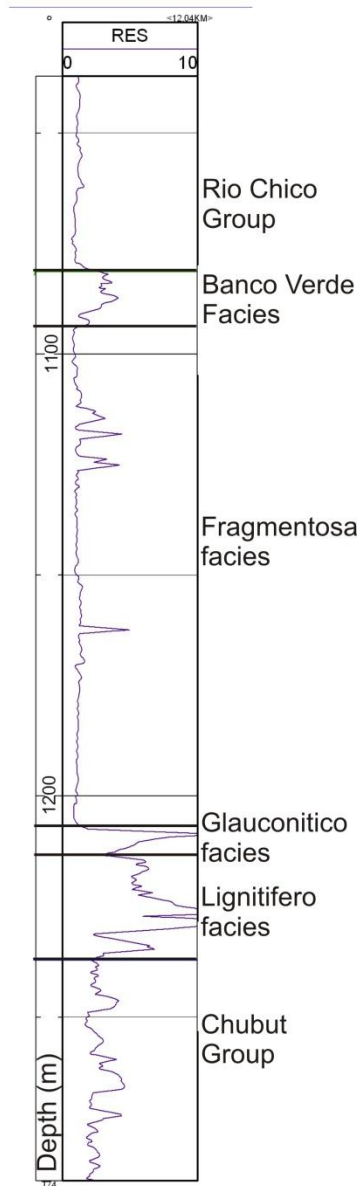


Fig. 21: Wireline log in meters showing the resistivity (RES curve). The subsurface expression of facies within the Salamanca Fm. in these logs mirror the facies described by Feruglio (1949) The API number is listed at the top of the well (T74) (see Fig. 23 for location relative to other logs).

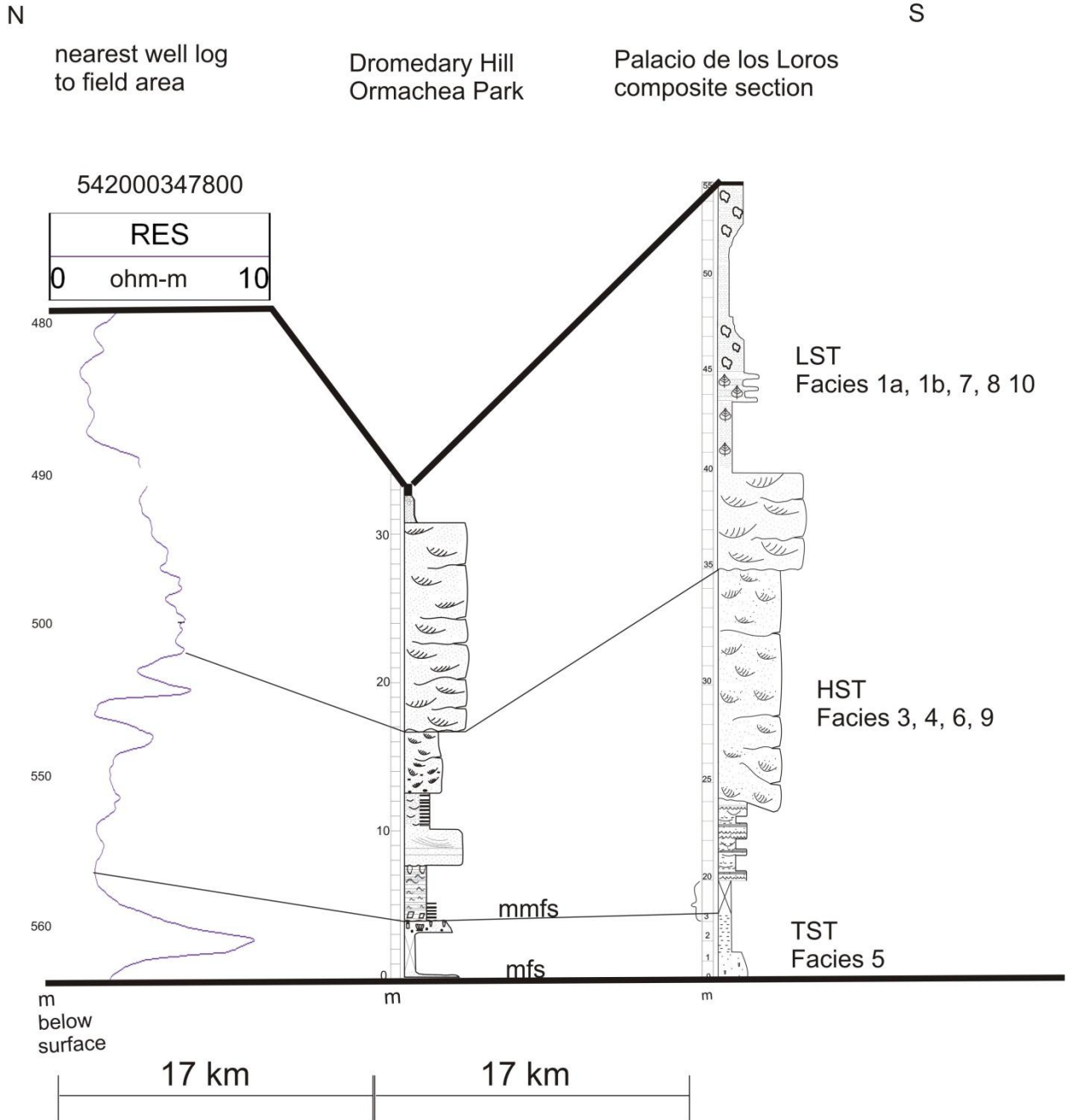


Fig. 22: Resistivity curve from a well approximately 17 km away from outcrops showing the correlation between the Salamanca Fm. in the subsurface and PL and OR. Facies are correlated according to resistivity signature. Spacing is relative to distance. The API number is listed at the top of the well (542000347800) (see Fig. 23 for location relative to other logs).

Cross section A-A' (see Fig. 1 for location) spans from the San Bernardo range to the towns of Holdich and El Tordillo, about 250 km eastward (Fig. 23). Significant facies changes occur as noted earlier by Sylwan (2001). Wireline logs in the A-A' cross section represent three facies patterns. The first facies pattern occurs in wells west of the field area. The second facies pattern spans from the field outcrops to 20-30 km east of the field area. Facies pattern 3 occurs east of the study area and is characterized by the facies described by Feruglio (1949).

The first facies pattern of the Salamanca Fm. begins with a 5-20 m section of high resistivity followed by a 40-50 m section of low resistivity with occasional 1-2 m spikes of higher resistivity in the upper 10 m. The lower high resistivity signal represents sands deposited as transgressive lag during the same transgression seen in field outcrops. Above the transgressive deposits lie 40-50 m of sediments with a low resistivity signature representing muddy or silty facies. These low resistivity deposits are interpreted as muddy offshore or tidal flat deposits with occasional sand pulses.

The second log facies pattern has greater variability in its resistivity signature (e.g. Fig. 22). This facies package ranges from 35-60 m in thickness in the field area and gradually thickens eastward to approximately 100 m. It begins with 5-15 m of high resistivity transgressive sand, representing the TST and corresponding to facies 5 at PL and OR. This transgressive lag is overlain by 20-30 m of low resistivity mud interpreted as shelf muds defining the base of the HST. Overlying these muds are 10-20 m of higher resistivity sand representing sandy tidal channel deposits and tidal bars. This section represents facies 1a, 1b, 2, 3, and 4 and contains upper HST deposits, a sequence boundary, and the first LST deposits. Five to ten m of low resistivity muds cap



the unit, representing tidal mud flats, accretion beds, and abandoned channel fill of facies 7, 8, and 10.

Log facies pattern 3 can be correlated to the four facies described by Feruglio (1949) (e.g. Fig. 21). It is characterized by the same basal transgressive lag in the first 10-30 m of section. This transgressive lag is overlain by 75-150 m of muddy deposits with one characteristic spike in resistivity in the middle of this muddy section. The lower muddy deposits are interpreted as low energy, outer shelf deposits. The uppermost deposits likely represent the infilling of the estuary, the spread of tidal mud flats and a widespread coastal swamp.

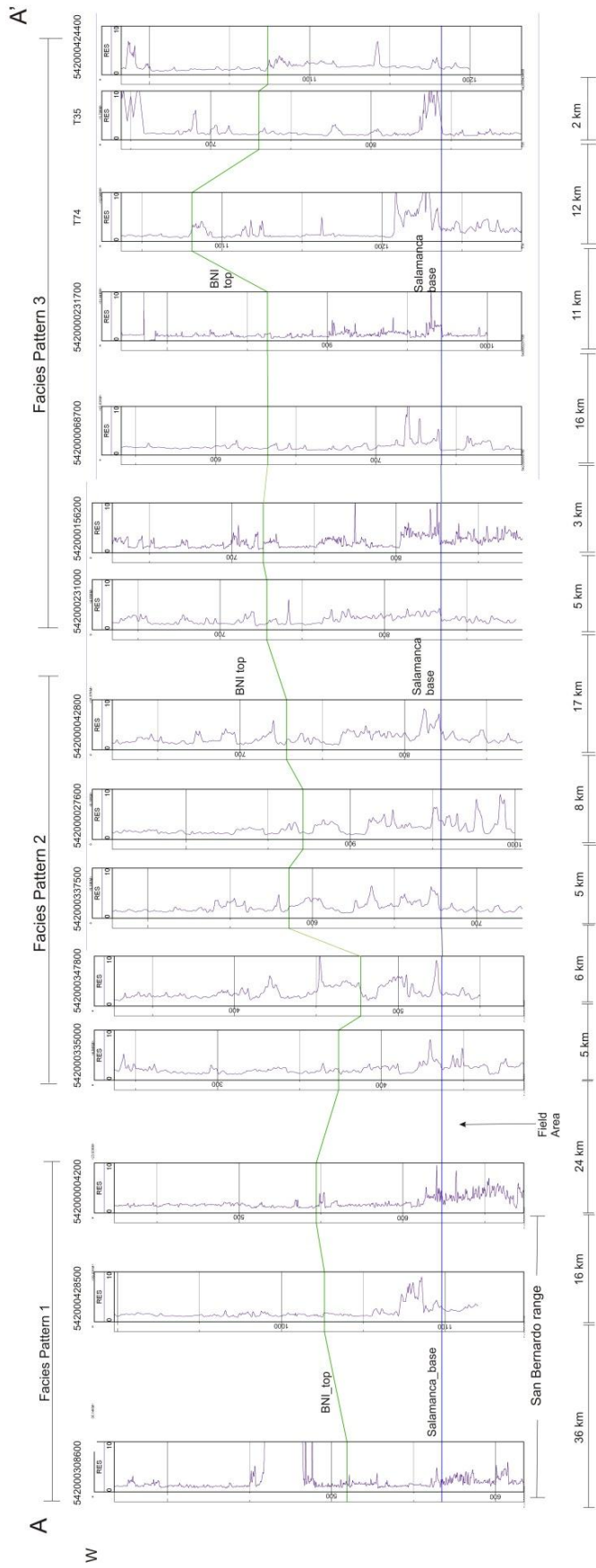


Fig. 23: Cross section A-A' (for location see Fig. 1) of the resistivity logs showing the thickening of the Salamanca Fm. toward the east. This cross section also shows the transition of facies from west to east and three distinct facies patterns (1, 2, and 3).

The Salamanca Fm. in the study area reaches a maximum thickness of 150 m in the most eastern wells near the center of the basin (Fig. 24). The thinnest areas of Salamanca Fm. (50-70 m) occur in the project area and westward toward the San Bernardo thrust front. This indicates a lack of accommodation space near the more proximal edge of the basin.

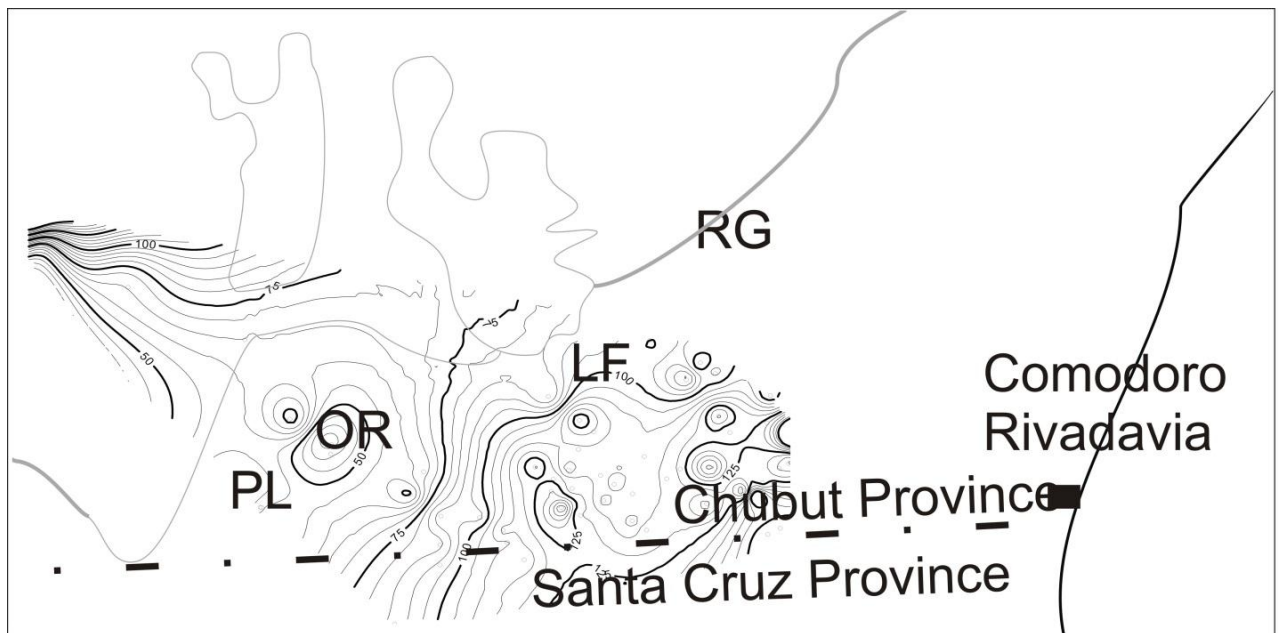


Fig. 24: Isopach of the Salamanca Fm. based on resistivity wireline logs. This isopach map shows thickening of the Salamanca Fm. to the east, reaching thicknesses of 150 m in the most eastern wells. Contour interval is 5 m.

## MODELING

Two theoretical end member geometries of the San Jorge embayment were modeled to explore tidal dynamics during deposition of the Salamanca Fm. Case I (Fig. 25) is a funnel-shaped embayment with one large and two smaller rivers entering from the northwest. The steady freshwater discharges are 10,000, 3,000, and 3,000  $\text{m}^3/\text{s}$ . Case II (Fig. 26) represents a wide arcuate embayment with 120% of the total fluvial input of Case I. This arcuate embayment has 6 small fluvial sources, four with a discharge of 3,000  $\text{m}^3/\text{s}$  and two with a discharge of 4,000  $\text{m}^3/\text{s}$ . Fluvial inputs are arbitrary but are assigned to illustrate differences between one large fluvial source versus many smaller sources. Shelf bathymetry values in both models mirror the shelf bathymetry of the modern San Jorge embayment (Glorioso and Flather 1997) because no paleo-bathymetries are documented from the Paleocene.

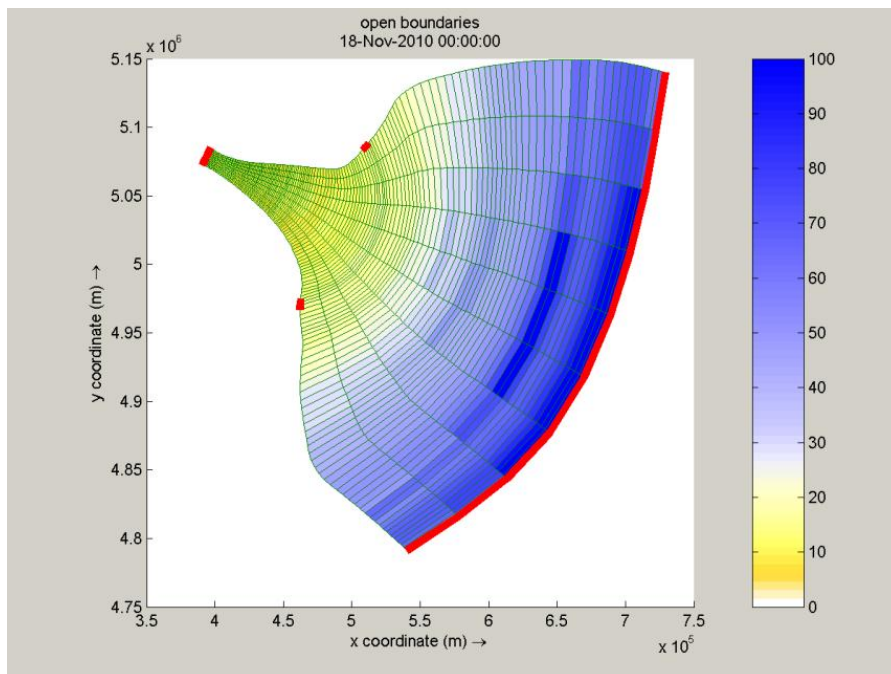


Fig. 25: Geometry of the funnel-shaped embayment. Thick lines represent open boundaries and color bar represents bathymetry in meters.

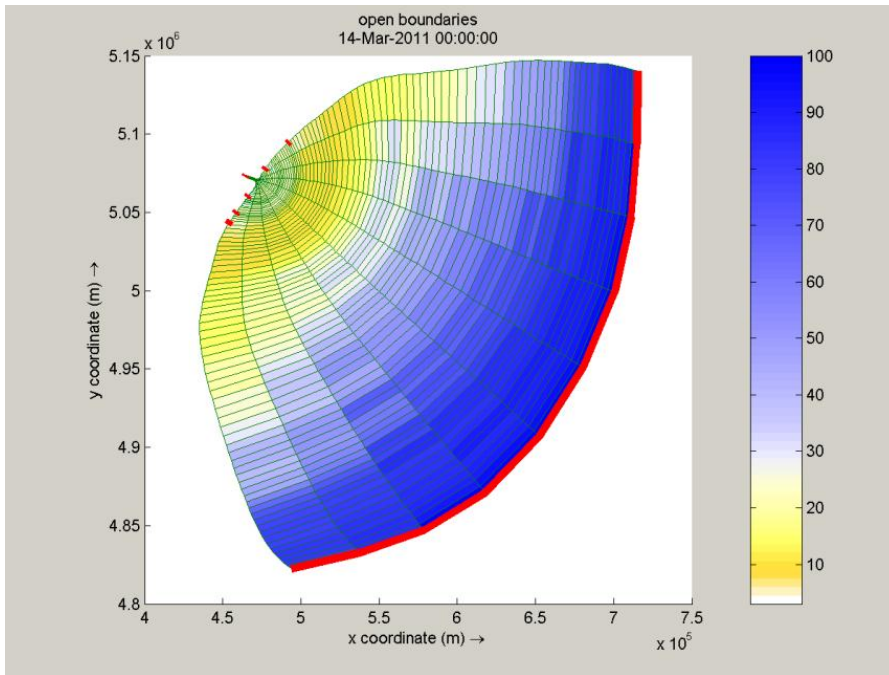


Fig. 26: Geometry of the arcuate embayment. Thick lines represent open boundaries and color bar represents bathymetry in meters.

Results (Figs. 27, 28) show that steady-state tidal ranges are greater in the funnel-shaped estuary. A maximum amplification of approximately 4.4 times the boundary tides occurs in the headwaters of the funnel-shaped estuary, and lesser amplification occurs seaward. The arcuate embayment shows lesser but still significant amplification of tidal ranges up to 2.1 times the boundary tides. Areas of greater amplification occur near fluvial sources in both geometries and there is a slight bias toward higher amplification in the southwest portions of the embayment.

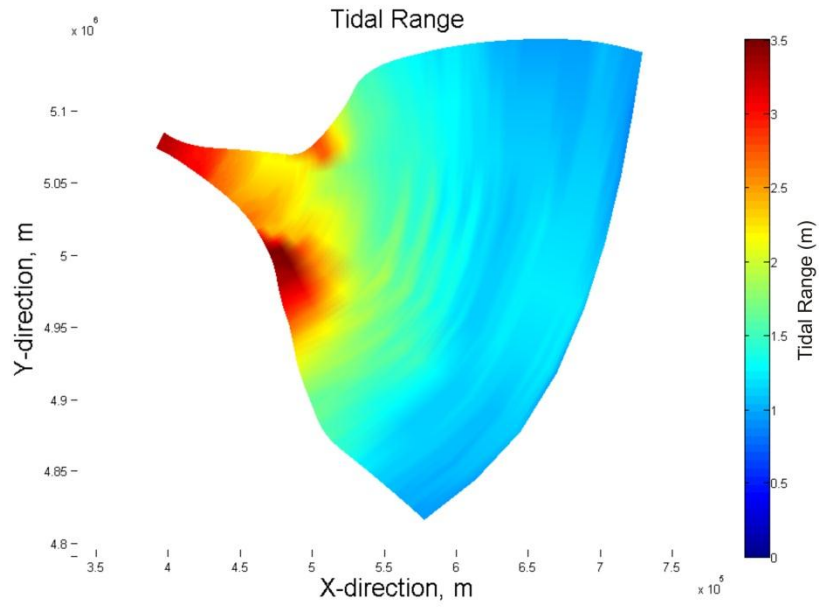


Fig. 27: Tidal range of the funnel-shaped embayment showing maximum tidal amplification of 3.5 m near the estuary head.

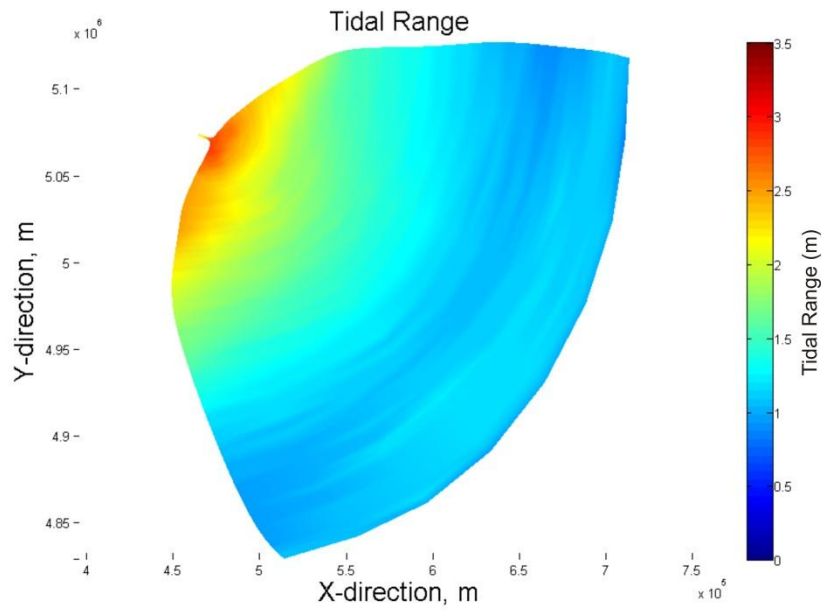


Fig. 28: Tidal range of the arcuate embayment showing maximum tidal amplification of 2.5 m near the estuary head.

What is the origin of this amplification? There are three potential causes—horizontal convergence of the tidal wave crest, vertical convergence due to shallowing bathymetry, and resonance across the shelf. The effects of horizontal and vertical convergence are given by Green’s Formula for frictionless wave propagation as:

$$\frac{a_2}{a_1} = \left(\frac{l_1}{l_2}\right)^{\frac{1}{2}} \left(\frac{h_1}{h_2}\right)^{\frac{1}{4}} \quad (1)$$

where subscripts 1 and 2 denote two different locations in a converging embayment,  $a$  is the amplitude of a tidal wave,  $l$  is the width of the embayment into which the tidal wave is traveling, and  $h$  is the average still water depth. Tidal wave amplitude rises as the square root of horizontal convergence and quarter root of shallowing water depth. Resonance arises when the distance from the edge of the continental shelf to the shoreline is a quarter wavelength of the semi-diurnal tidal wave (e.g. Godin, 1993). Thus the tides at the shoreline should be amplified by resonance when the width of the shelf and embayment  $W = 1/4L$ . The wavelength  $L$ , of a tidal wave is given by:

$$L = \frac{2\pi\sqrt{gH}}{\sigma} \quad (2)$$

where  $H$  = the mean water depth of the shelf and embayment and  $\sigma$  = the angular frequency of the tidal component in radians per second, which for an  $M_2$  tide equals  $1.405 \times 10^{-4} \text{ s}^{-1}$ .

To separate convergence from resonance as causes of the tidal amplification in the Paleocene San Jorge Basin, simulations were conducted with uniform still-water depths ranging from 5 to 150 m. Results show that maximum tidal amplification occurs

at a uniform still water depth of 25 m in both the funnel and arcuate embayments (Figs. 29, 30). Tidal amplification at PL and OR can be as great as 1.8 m or as little as 0.3 m with no changes in the model except bathymetry values.

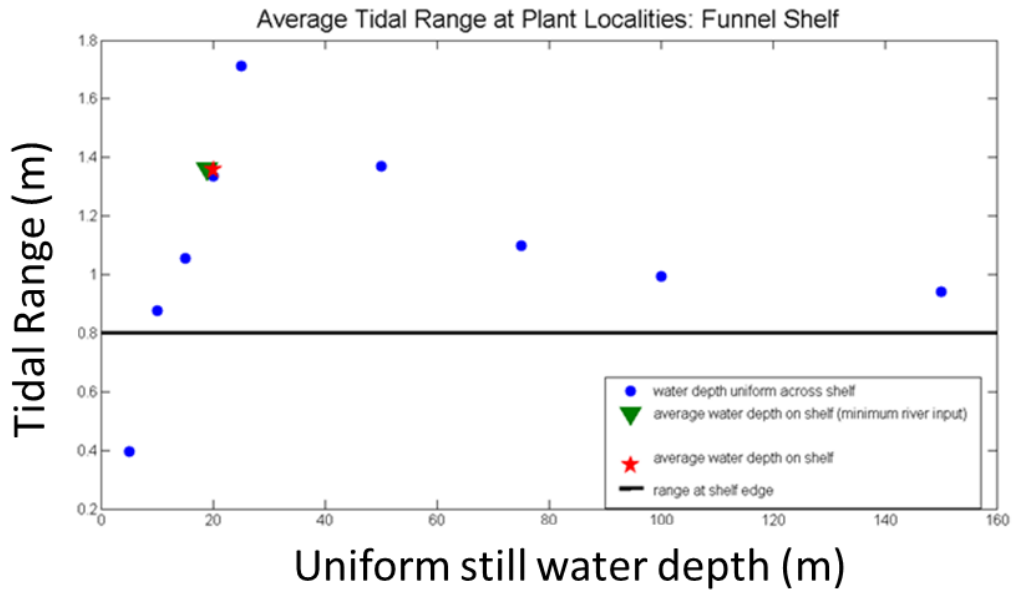


Fig. 29: Graph showing the relationship between water depth and tidal amplification at PL and OR in the funnel-shaped embayment. Maximum amplification occurs at a uniform depth of 25 m.

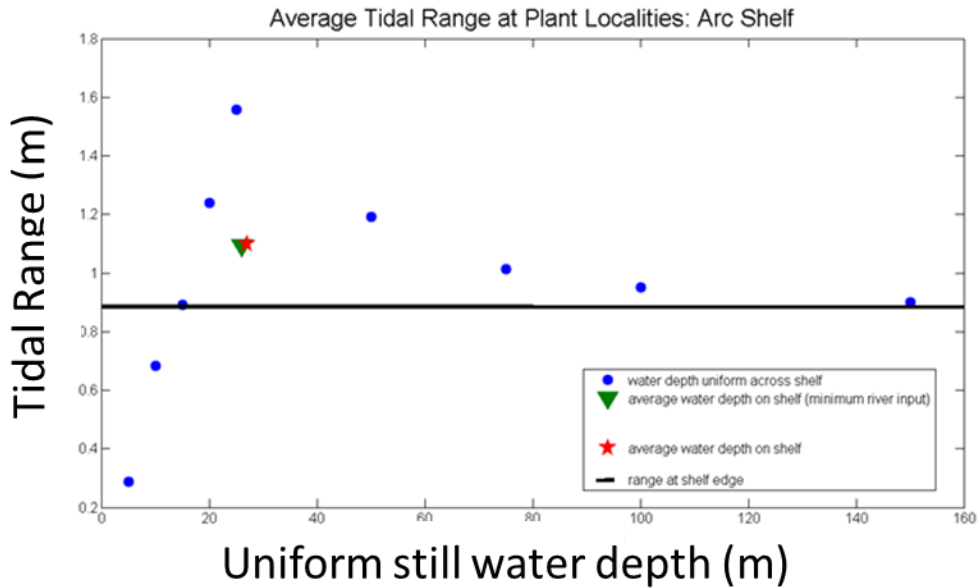


Fig. 30: Graph showing the relationship between water depth and tidal amplification at PL and OR in the arcuate embayment. Maximum amplification occurs at a uniform depth of 25 m



The amplification in these simulations must arise from a combination of width-convergence and resonance because depth is held uniform. To determine if the cause is resonance, I compute the wavelength of the tide in the embayment from Eqn. 2, and divide by 4 to find the resonant width. The resonant width equals approximately 175 km when the uniform depth is 25 m. Average widths are 222 km in the funnel-shaped embayment and 213 km in the arcuate embayment. Thus, the principal cause of the amplification must be width-convergence with a smaller contribution from resonance. Tidal ranges are much greater in the funnel-shaped embayment, also implicating width-convergence. Given the geometry of the SJB with massifs to the north and south, we can conjecture that the paleo-SJB was an embayment that amplified tides, thusly creating the tidal deposits of the Salamanca Fm.

Water velocities for both geometries show the greatest speeds near the estuary head (Figs. 31, 32). Velocity patterns are grouped into 6 hour periods consistent with the ebb and flood tides of M2 semi-diurnal tides. Water velocities in the funnel-shaped embayment remain fairly constant from the shelf until the embayment begins to quickly narrow, approximately 100 km landward. At this point, velocities increase to speeds up to 1 m/s. Velocities in the arcuate embayment only reach 0.5 m/s and show a gradual increase landward rather than a sharp change as seen in the funnel-shaped embayment. This difference is attributed to width-convergence.

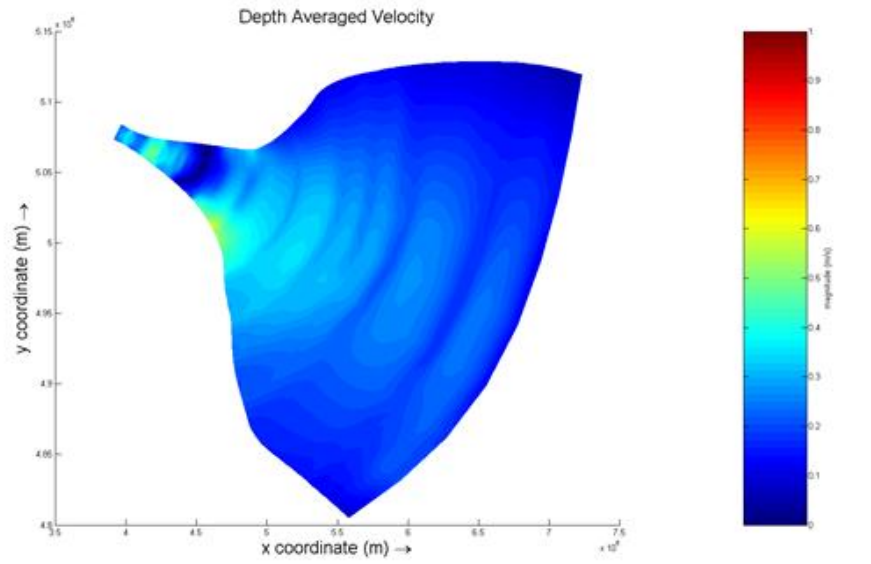


Fig. 31A

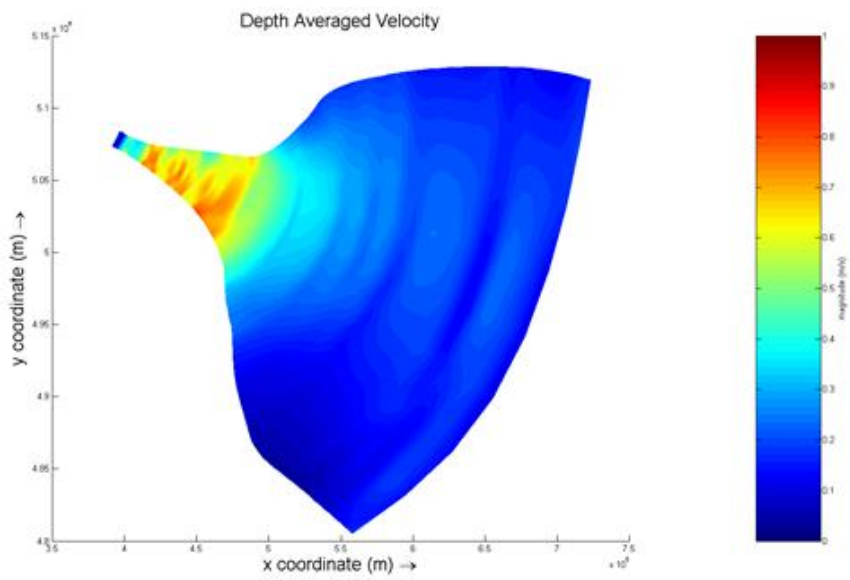


Fig. 31B

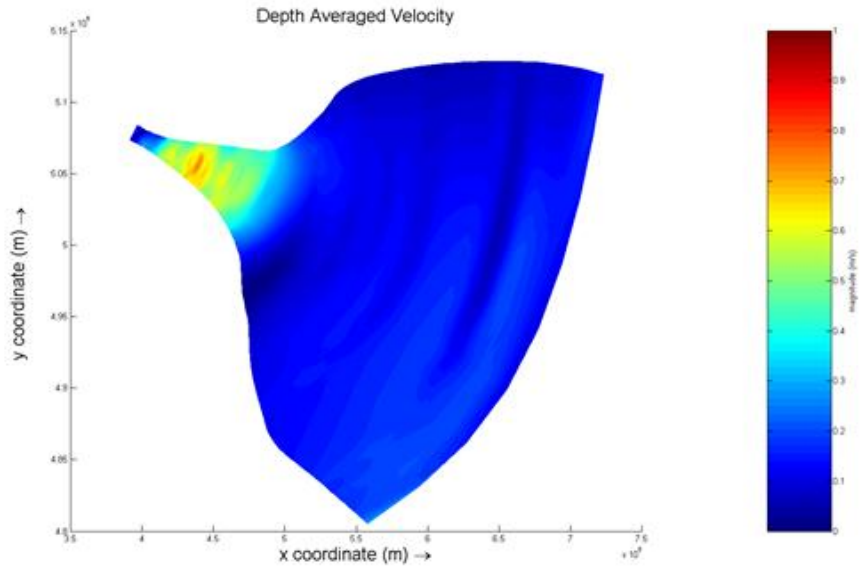


Fig. 31C

Fig. 31A-C: Depth averaged velocity in the funnel-shaped embayment in two hour time increments. Velocities within the embayment follow repeating patterns every six hours, consistent with the ebb and flood currents of M2 tides. Maximum velocities occur near the estuary head as tides rush into and out of the most constricted area of the embayment.

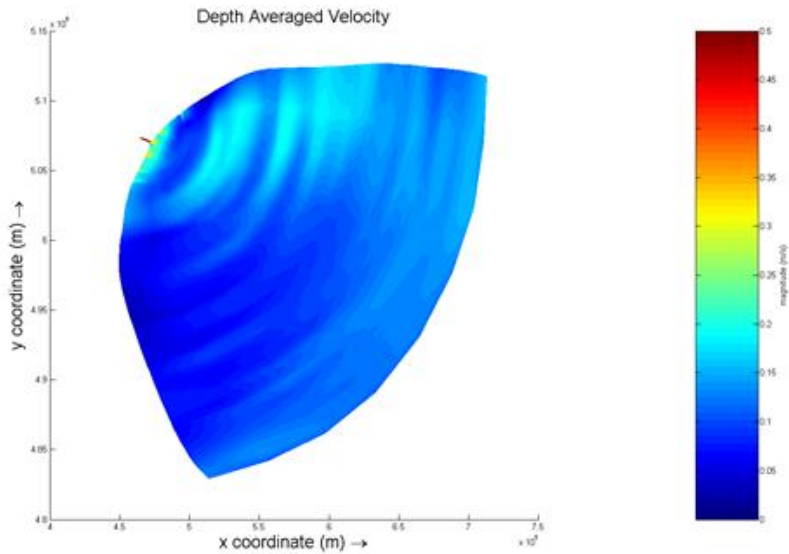


Fig. 32A

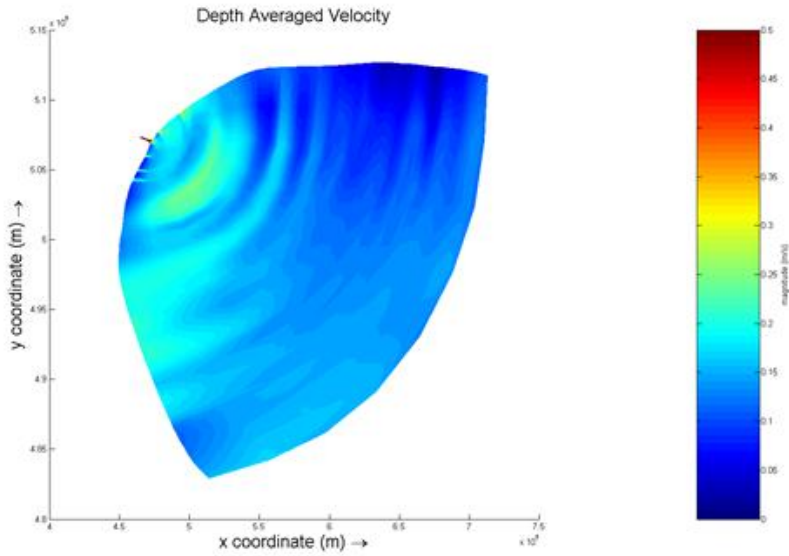


Fig. 32B

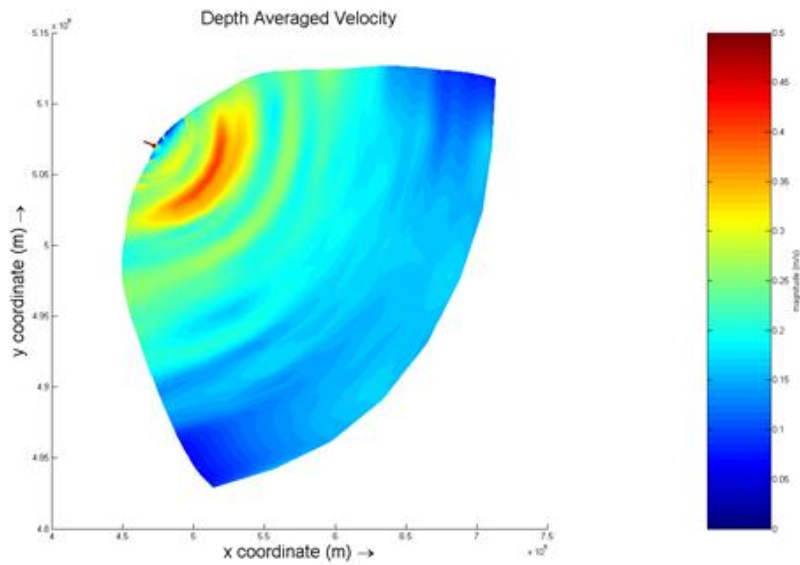


Fig. 32C

Fig. 32A-C: Depth averaged velocity in the arcuate embayment in two hour time increments. Velocities within the embayment follow repeating patterns every six hours, consistent with the ebb and flood currents of M2 tides. Maximum velocities occur in the landward portion of the embayment.

To gain an understanding of sediment circulation in the simulated basins, two grain sizes .2 mm (fL) and < .15 mm (silt) were introduced into all river mouths at their local equilibrium concentrations. The model was run twice using initial sediment concentrations of the order of  $\text{mg/m}^3$  and  $\text{kg/m}^3$  to represent two hypothetical end members. Both embayment configurations experience deposition of sediment near their river mouths (Figs. 33, 34). Sediment deposition in the remaining area of both embayments is fairly uniform with increasing deposition seaward (Figs. 35, 36). This seaward band of sediment deposition is greater in the arcuate embayment than the funnel-shaped embayment. The funnel-shaped embayment also displays a banded pattern of deposition and erosion in the most constricted area of the embayment from the fluvial headwaters 100 km southeastward. As expected, sediment accumulation was significantly greater when initial concentrations were higher. However, within the 5 year time period even the lesser sediment concentrations produced sediment accumulation up to a meter in some areas.

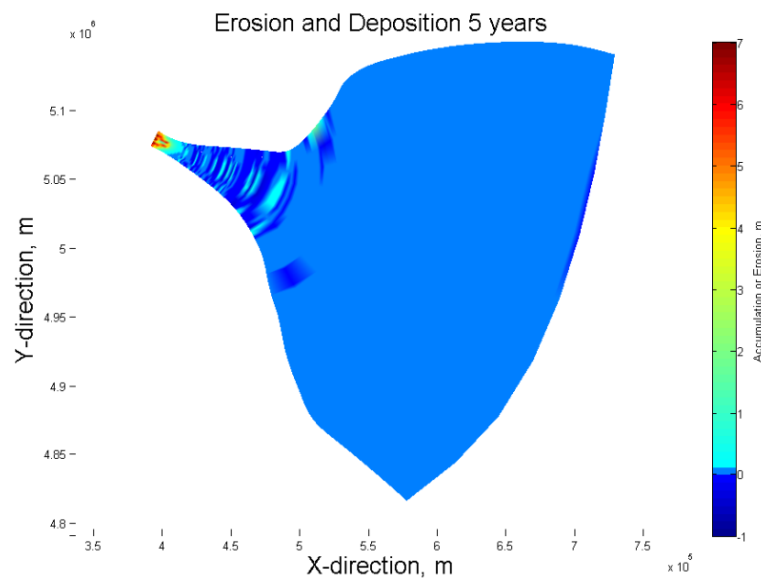


Fig. 33: Net deposition and erosion in the funnel-shaped embayment after five years. This figure represents the high sediment concentration end member and shows increasing sedimentation in the fluvial headwaters suggesting the formation of bayhead deltas. Sedimentation in other areas of the embayment remains fairly uniform.

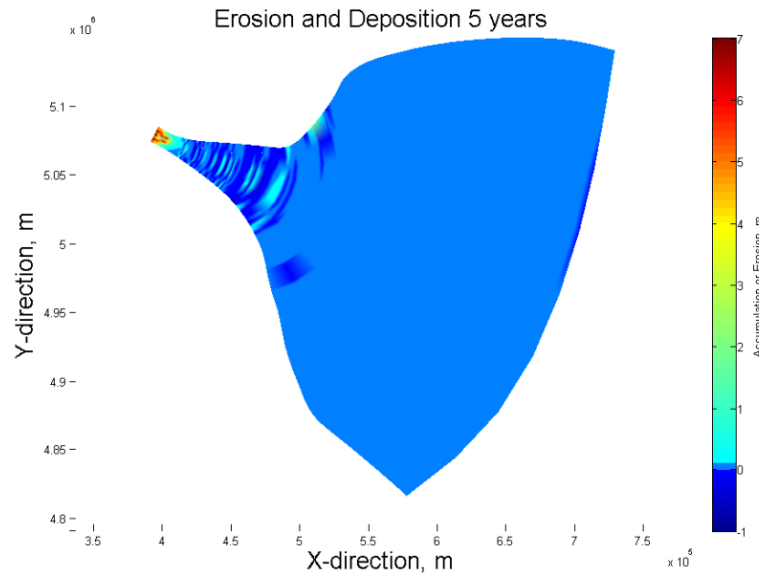


Fig. 34: Net deposition and erosion in the arcuate embayment after 5 years. This figure represents the high sediment concentration end member and shows increasing sedimentation in the fluvial headwaters suggesting the formation of bayhead deltas. Sedimentation in other areas of the embayment remains fairly uniform.

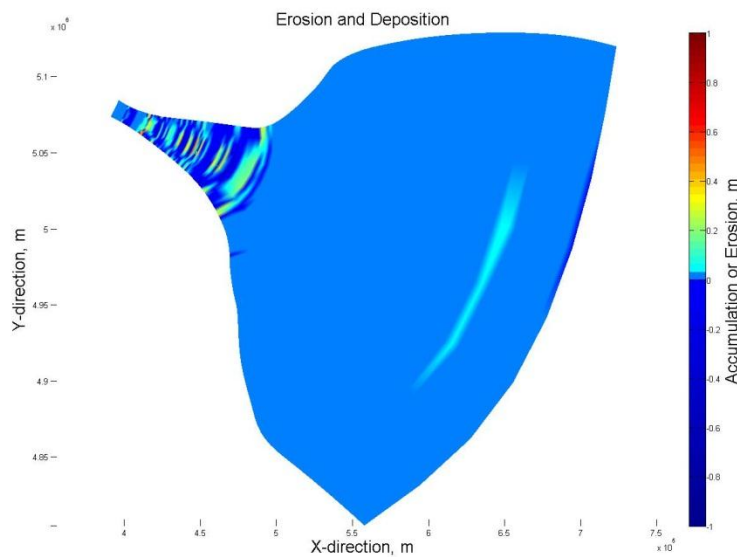


Fig. 35: Net deposition and erosion in the funnel shaped embayment after 5 years. This figure represents the low sediment concentration end member and shows increasing sedimentation in the fluvial headwaters but no formation of bayhead deltas. Sedimentation in other areas of the embayment remains fairly uniform.

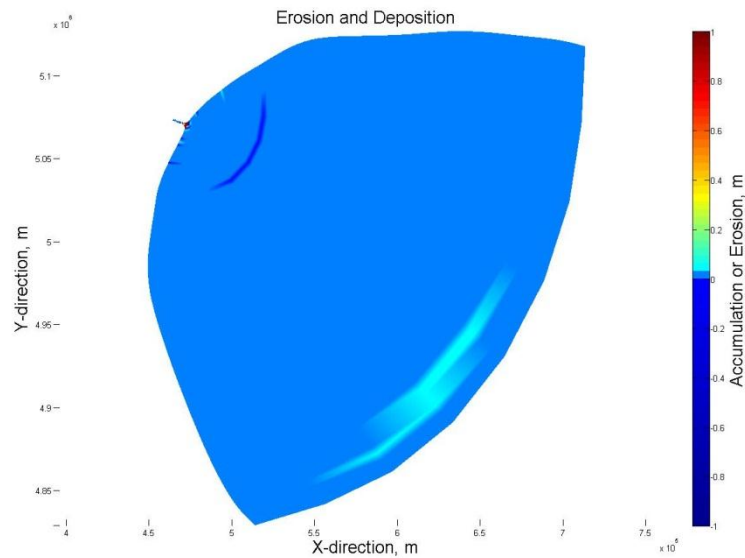


Fig. 36: Net deposition and erosion in the arcuate embayment after 5 years. This figure represents the low sediment concentration end member and shows increasing sedimentation in the fluvial headwaters and the possible formation of a bayhead delta. Sedimentation in other areas of the embayment remains fairly uniform.

In summary, these simulations have shown that mesotidal conditions inferred from sedimentary structures of the outcrop belt are sensible. The increased tidal ranges and currents arise principally from width convergence of the basin with smaller contributions from depth-convergence and resonance.

## DISCUSSION

### ***Depositional Model of the Salamanca Formation***

I interpret the Salamanca and BNI Fms. to have been deposited in an estuary to coastal-plain depositional system. Estuarine deposits are defined as fluvial-, wave-, and tide- influenced sediments located in the seaward portion of a drowned river valley system derived from both fluvial and marine sources (Dalrymple et al. 1992). Estuarine deposits include tidal and coastal facies.

The Salamanca Fm. in the study area represents a shallowing-upward estuarine sequence beginning with a significant marine transgression that forms the base of the section and creates the transgressive systems tract (TST) (Fig. 37). This transgression floods Cretaceous fluvial valleys and the subsiding SJB, creating an estuarine setting. Low energy deeper water sediments define the maximum flooding surface (mfs). As sediment supply overwhelms the rate of accumulation of accommodation, a system of high energy tidal channels, bars, tidal flats, and coastal lowlands prograde to form the highstand systems tract (HST). These HST deposits are capped by progradational facies and then an erosional unconformity defining a sequence boundary. After relative sea level fall, a switch from negative to positive accommodation allows proximal tidal channels and bars to accumulate as lowstand systems tract (LST). These tidal channels are gradually infilled giving way to a widespread coastal swamp overlain by an unconformable surface and fluvial sediments of the Peñas Coloradas Fm.

Figure 37 gives the sea level curve based on the sequence stratigraphy of the Salamanca and BNI Fms. as well as the units that overlie and underlie these formations. This sea level curve can be compared to the Haq sea level curve based on the ages determined by Marshall et al. (1981,1997), Iglesias et al. (2007), Andreis (1977), Méndez (1966), and Bertels (1975). The TST at the base of the Salamanca Fm. is consistent with the Haq sea level curve that places a large-scale transgression at the end of the Cretaceous (Haq and Hardenbol 1987, Miller et al. 2005). In the Haq sea level curve, this transgression is followed by a stable period of sea level highstand lasting from approximately 64-62.5 Ma. This HST is then followed by a slight drop in sea level from approximately 62.5-61 Ma. At approximately 61 Ma there is an increase in



sea level followed by a sharp and longstanding period of lowstand (Haq and Hardenbol 1987, Miller et al. 2005). These Haq sea level trends agree with the proposed sea level curve in Figure 39 of transgression followed by highstand and then a brief period of lowstand.

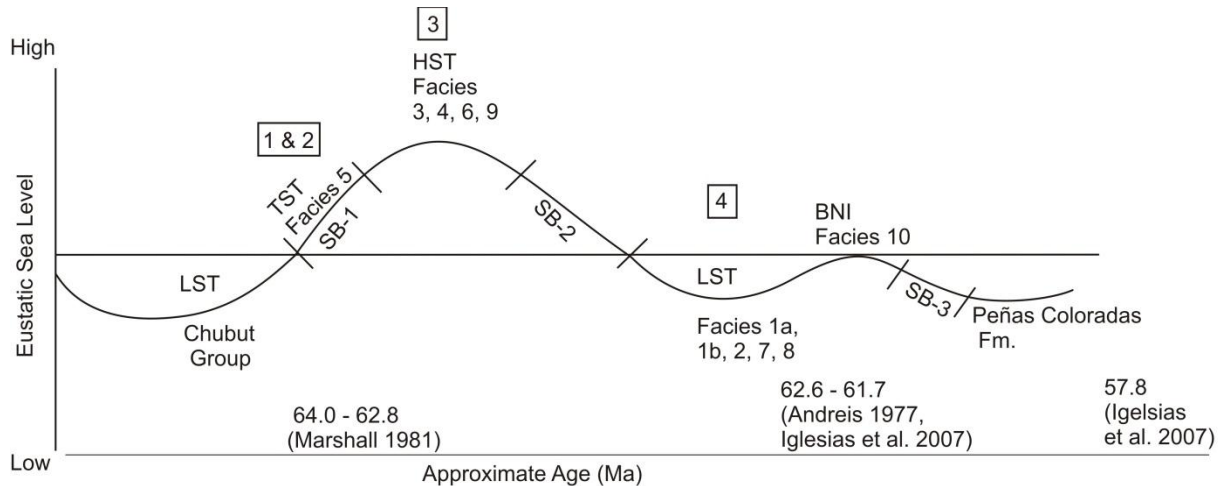


Fig. 37: Proposed eustatic sea level curve for the Chubut Group and Salamanca and Banco Negro Inferior Fms. showing time and formation of systems tracts and facies. Numbers refer to stages in Fig. 38.

The depositional model of the Salamanca/BNI estuarine system contains four main stages of development (Fig. 38). Stage One of the Salamanca Fm. represents the TST and formation of the estuary as Cretaceous fluvial deposits of the Chubut group are flooded by a widespread marine transgression. This stage is represented by the undulating marine flooding surface at the base of the Salamanca Fm. (Martinez 1992). This flooding is observed throughout all the Atlantic bordering basins of southern South America and is attributed to widespread crustal thickening and a warming climate during the Late Cretaceous (Uliana and Biddle 1988, Legarreta and Uliana 1994, Miller et al.

2005, Malumián and Náñez 2011). Due to the shallow slope of the coast at this tectonically quiescent period of time (Uliana and Biddle 1988), the Late Cretaceous transgression inundated a large area of land, most likely extending westward at least as far as the San Bernardo belt which began uplift during the Late Cretaceous ~80 Ma (Folguera et al. 2011). This created a widespread epeirc sea with a low diversity of foraminifera dominated by *Buliminella isabelleana* (Malumián and Náñez 2011). Sandy deposits within facies 5 represent storm events bringing proximal sands further out into the basin. These progradational sands are a common characteristic in tide-dominated estuaries (Dalrymple 1992), supporting the idea that tidal influence was present as early as facies 5.

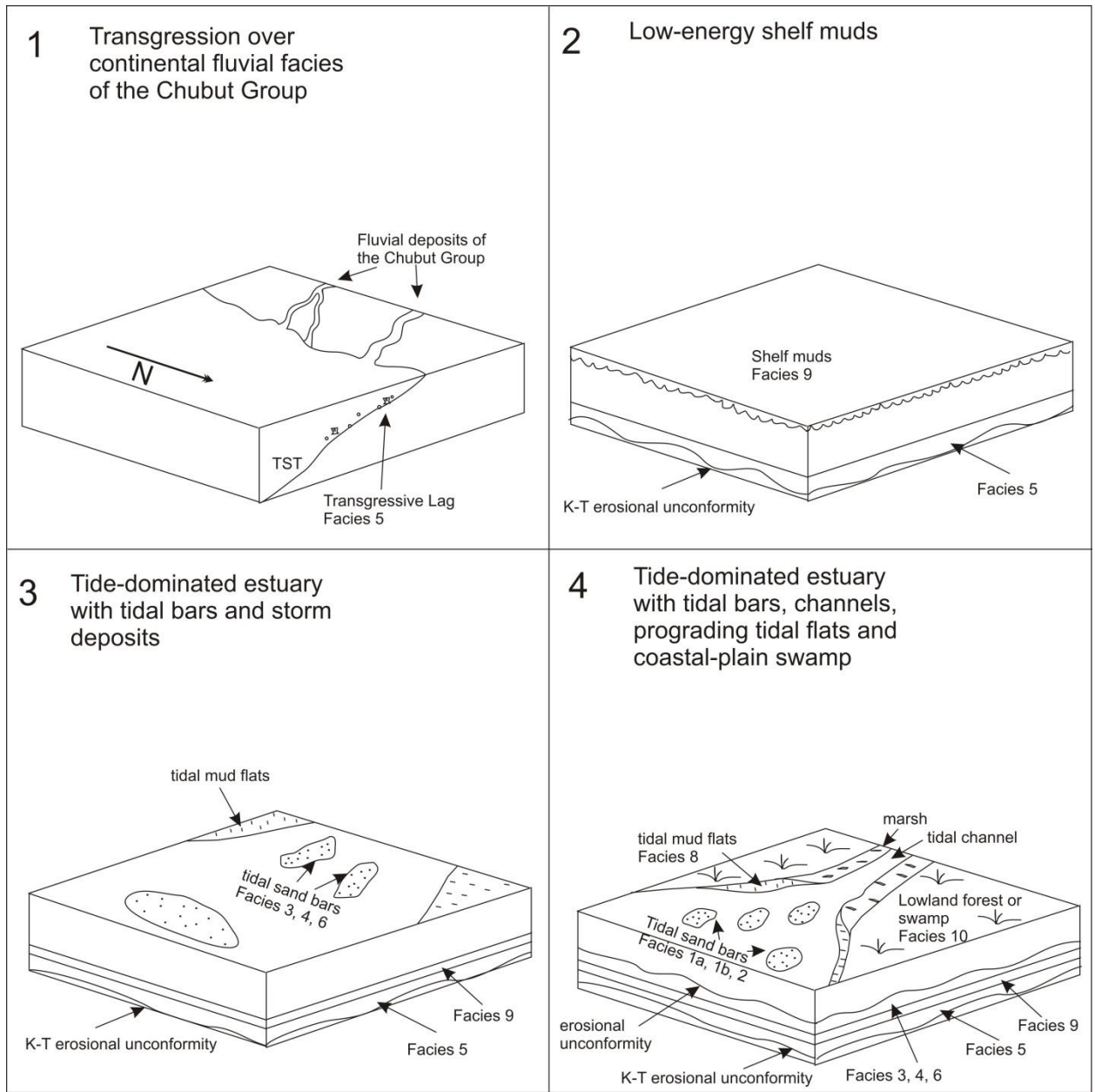


Fig. 38: Depositional model for the four stages of the Salamanca and BNI Fms., in the vicinity of PL, OR, and RG.

Stage Two, the beginning of the HST, is defined by clay deposits within facies 9 that represent low energy deeper water shelf deposits with few organisms. These shelf deposits accumulate slowly but are not bioturbated, suggesting deposition in an anoxic environment.

Sandy and silty facies 3, 4, and 6 represent later phases of the HST and Stage Three. Tidal indicators suggest that these facies were deposited within 10's of km from the estuarine headwaters. Glauconite suggests water depths greater than 60 m in some facies (Odin 1988). Rhythmic flaser and lenticular bedding of facies 6 represent a time of dominant tidal energy with little fluvial input. These tidal rhythmites are common in tidal bars (Zhang and Zhang 2006) such as deposits described in the tidal sand-bar complex zone of Dalrymple's estuarine model (Dalrymple et al. 1990). Tidal- and storm-influenced facies 3 and 4 represent the upper portions of tidal sand bars that are dominated by bidirectional cross-bedding (Zhang and Zhang 2006). Fine to medium grain size and trough cross-bedding orientations indicate that these facies were dominantly formed from ebb tides that generally flowed through the central mid-channel of the estuary (e.g. Harris 1988, Dalrymple et al. 1990). The progressive fining-upward of these facies along with thin accretion beds and plant accumulations suggest a progressive shallowing-upward of water depth, as would occur with progradation of intertidal mudflats or abandoned channel fill proximal to a lowland forest or swamp.

Stage Four is the time of deposition of the LST above a second erosional unconformity that underlies fluvially-influenced tidal channel deposits of facies 1a and 1b. These deposits lie within the transitional reaches of rivers. Subfacies 1b represents runoff microdeltas created by late ebb currents during low tide that infill scours in facies 1a (Dalrymple et al. 1990). Clay drapes (Fig. 7G) preserved on the lee side of cross beds indicate low-tide slackwater deposits within the subtidal zone (Fenies et al. 1999). These deposits contain sets of "tidal bundles" where the sandy deposits wedged in between these clay drapes represent an ebb-flood cycle (Tape et al. 2003). Plane-

parallel laminations of facies 2 represent upper-flow regime deposits of bar tops. These sediments represent the highest energy paleo-flows and the most proximal channel deposits of the Salamanca Fm. (Dalrymple et al. 1990, 1992).

Estuarine infilling through lateral point bar accretion, tidal flat muds, and progradation of a widespread coastal swamp completes the LST. Infilling of truly tidally dominated estuaries does not necessitate the formation of bay-head deltas (Boyd et al. 1992), and in fact none are seen in the study area. It appears that the regime experienced only the seaward progradation of intertidal mudflats and sand banks (Harris 1988, Boyd et al. 1992). Facies 7, 8, and 10 represent a time of low energy, low tidal influence, low sedimentation rate, and high plant diversity

#### ***Environmental Interpretations of Plant Localities***

Ten plant localities were visited in the study area and of these, eight occur at the OR and PL sites (OR-1, OR-2, Cerro Solo, PL1, PL-2, PL-3, PL-4, and PL-5) and the other two occur within RG and LF. The macrofossils all occur in estuarine deposits of the Salamanca Fm. at two stratigraphic levels- near the top of facies 3, and within the lower sections of facies 7 and 8 just above facies 1a.

Plant macrofossils near top of facies 3 (sites OR-2, Cerro Solo, PL-1, PL-3, and PL-4) represent transported deposits occurring at the end of a shallowing-upward cycle that caps the HST. OR-2 and Cerro Solo plant localities occur within silt lenses and, due to their close proximity, it is likely that these deposits represent the same silt lens. This silt lens occurs as a 10 cm thick deposit that thins southward and is laminated in some areas. Lamination implies low energy deposition possibly during slackwater but poor plant preservation implies that these deposits are allochthonous.

Plant localities PL-3 and PL-4 occur within two laminated silt deposits at the top of facies 3. These silty deposits are much thicker (40-80 cm) than the silt lens at OR-2, possibly indicating a longer period of deposition in a low-energy environment. The PL-1 plant locality occurs at the top of facies 3 (Figs. 14, 15) where accretion sets give way to 1.6 m of silty laminated deposits with well-preserved macroflora fossils.

PL-1, PL-3, and PL-4 show evidence of the abandonment and infilling of high energy tidal channels through accreting point bars and prograding tidal mud flats. The plants of PL-1, PL-3, and PL-4 were preserved in these tidal mud flats (facies 8) which were located closer to the plant source than the underlying high-energy tidal bars of facies 3. The sequence boundary overlying these plant deposits represents an erosive unconformity cutting into coastal deposits followed by the LST. Because plant localities PL-3 and PL-4 lie in silt deposits just above facies 3 and display poor preservation, they also suggest allochthonous deposits. PL-1, however, displays good preservation and lies 1-2 m above the sandy deposits of facies 3 indicating further progradation of the coastal sediments and allochthonous deposits.

With the exception of PL-1, plant localities above facies 1a (OR-1, PL-5, PL-2) occur in an environment more proximal to the plant source than deposits above facies 3. OR-1 is deposited within a 6 m accretion-set consisting of alternating thick sandy deposits and thin silty deposits with preserved macroflora occurring in the silty deposits. These deposits are interpreted as point bar accretion during the lateral migration of a tidally influenced, freshwater channel. Given this environment, it is conceivable that OR-1 deposits are allochthonous.

PL-5 is deposited near the top of facies 1a within a clay drape. Clay drapes are common at the PL-5 site, range in thickness from 10-50 cm, and are deposited as lenticular bodies occurring on the foresets of a coarse trough cross-bedded sand (Fig. 17). Tape et al. (2003) describe similar deposits within the Jordan sandstone of Minnesota as tidal bundles. The clay deposition occurs during low-tide slackwater and the white sands represent one ebb and flood cycle (Tape et al. 2003). Flora within these clay drapes are allochthonous.

PL-2 represents the most diverse, abundant, and well preserved macroflora. This locality lies at the base of facies 8 near the top of facies 1a and no accretion sets are present in this area. This stratigraphic location implies the final stage of estuarine progradation and infilling. It is likely that PL-2 represents a muddy deposit along a low-energy tidally influenced fluvial channel. These deposits are the most proximal to the plant source and represent parautochthonous to allochthonous deposits.

The Rancho Grande section sits approximately 54 km seaward of PL and OR. It consists of wispy to wavy bedded muds that grade into unidirectional cross-bedded sands (similar to facies 9 of OR and PL) and contains brackish and salt water fossils. One facies specific to RG is a 10-20 cm coquina composed of oyster and bivalve fossils (Appendix A). There are two possible depositional environments for the Rancho Grande locality. One is a localized low-energy bay sheltered by a barrier island or spit. The other is offshore in the open estuary distal from river mouths. In that case, the coquina likely represents storm deposits.

### **Modern Day Analogs**

Figure 39 gives two examples of modern day analogs for the depositional environment of the Salamanca and BNI Fms. The Bahía Blanca estuary (Fig. 39 A) is a mesotidal estuary dominated by tidal channels and extensive tidal mud flats (Ginsberg et al. 2003). The Bahía Blanca estuary is a good analog for facies 1a, 1b, and 8 that were deposited during the later stages of the estuary where tidal channels and tidal mud flats dominate.

A modern day analog for the BNI Fm. is the Great Dismal swamp of Virginia (Fig. 39 B). The Great Dismal swamp is a large coastal swamp comprised of 450,000 m<sup>2</sup> of forested wetlands along the Virginia and North Carolina coasts. This a good analog for the deposition of facies 10 the Banco Negro Inferior as they both represent widespread coastal swamps in temperate climates.

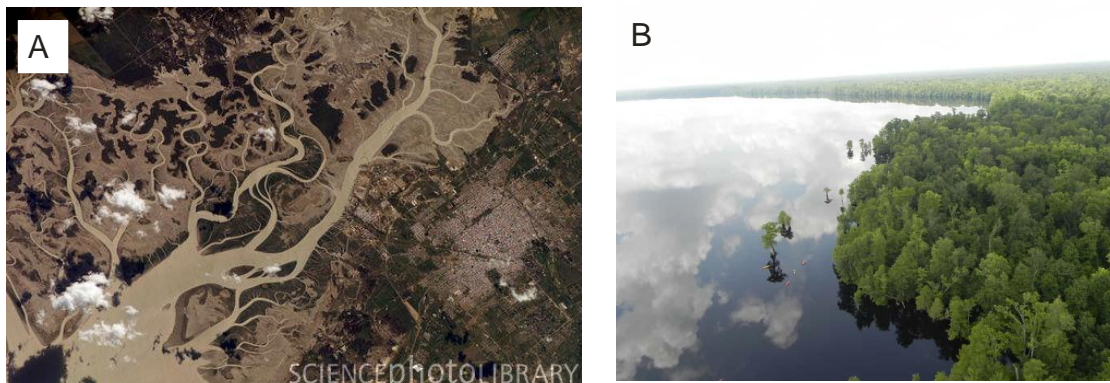


Fig. 39: Modern-day analog for the depositional environment of A)The Bahía Blanca estuary (photo from NASA <http://www.sciencephoto.com/media/174830/view>) later stage of the Salamanca Fm. and B) The Great Dismal Swamp of Virginia (<http://www.fws.gov/northeast>) as an analog for the Banco Negro Inferior

Ricardi and Branco (2009) studied modern plant preservation as an analog for ancient deposits. This study focuses on deposition within forested to swampy fluvial systems in the Itanhaem River Basin similar to interpreted environments of facies 8 and



10. They concluded that conditions leading to high plant preservation include anaerobic conditions, acidic water with high organic content, and rapid burial and sedimentation. Many of the parautochthonous deposits in their study only preserved those plants which were growing nearest the source and upland flora was scarce in the deposits. This implies that the Salamanca Fm. macrofloras must have come from swamps adjacent to the estuary rather than an upland or distant source.

Plant preservation is most common in depressions that experience a perennially high water table (Demko 1998). This is especially true in plants of vertic soils that are subject to expansion and contraction such as the soils of facies 8. Montmorillonite dominance also supports deposition in a lowland area with little leaching of sediment. Sedimentological evidence suggests a warm-temperate climate in a waterlogged, lowland forest or swamp.

## **CONCLUSIONS**

The Salamanca and BNI Fms. consist of 10 facies within PL and OR. Sandy facies show a recycled orogen provenance with a likely source of uplifted Andes terrains. Clay facies within the upper Salamanca Fm. and the BNI Fm. are classified gleyed vertisols dominated by montmorillonite with illite and halloysite occurring as weathering minerals. Montmorillonite dominance indicates that deposition occurred within a waterlogged basin during a warm-temperate climate. Facies within the Salamanca Fm. vary throughout the basin and sandy facies interpreted as tidal channels are replaced eastward by muddy facies interpreted as offshore or tidal flat deposits.

Plant localities at PL and OR occur at two stratigraphic levels within the Salamanca Fm.- above facies 3, and above facies 1a. All plant deposits represent estuary infilling, and the best-preserved sites (PL-1 and PL-2) are interpreted as the most proximal to the plant source. After analysis of each locality, plants show deposition in five environments- silty beds of accretion sets, transported silt lenses, mud drapes, tidal flats, and within muddy deposits of low-energy tidal channels.

Sequence stratigraphy of the paleo-SJB basin describe the Cretaceous-Paleocene unconformity at the base of the Salamanca Fm. as a sequence boundary and marine flooding surface. Overlying deposits are the TST capped by the maximum marine flooding surface. Subsequent facies make up the HST when sediment supply overwhelms accommodation space leading to the progradation of coastal deposits. Erosion of these costal-plain deposits creates the second sequence boundary which is overlain by the LST. The upper deposits of the Salamanca Fm. represent infilling of tidal channels, progradation of tidal flats, and a widespread costal swamp or lowland forest.

Sedimentological analysis and facies relationships within the Salamanca Fm. define a model for the paleo-SJB as a shallowing-upward, tidally influenced estuary in which tidal amplification is the result of width-convergence. Plant localities within PL and OR represent two stages of estuary infilling and the existence of a widespread, prograding coastal swamp represented by the Banco Negro Inferior Fm.

## REFERENCES

- ALLEN, B.L., and HAJEK, B.F., 1989, Mineral Occurrence in Soil Environments, *in* Dixon, J.B., and Weed, S.B., eds., *Minerals in Soil Environments: Minerals in Soil Environments*: Madison, WI, Soil Science Society of America, p. 199-278.
- ANDREIS, R.R., 1977, Geologia del rea de Canadon Hondo, Dto. Escalante, Provincia de Chubut, Republica Argentina *Revista Museo de La Plata*, v. Geol. IV, p. 77-102.
- BERTELS, A., 1973, Bioestratigrafia del Cerro Bororo, provincia del Chubut, Republica Argentina: *Actas del V Congreso Geologico Argentino*, Villa Carlos Paz, Cordoba, v. 3, p. 71-91.
- BERTELS, A., 1975, Bioestratigrafia del Paleoceno marino en la provincia del Chubut, Republica Argentina: *Actas del I Congreso Argentino de Paleontologia y Bioestratigrafia*, Tucumán, v. 2, p. 271-316.
- BOGGS, S., 1992, *Petrology of Sedimentary Rocks*: New York City, NY, Macmillan Publishing Company, 707 p.
- BOYD, R., DALRYMPLE, R., and ZAITLIN, B.A., 1992, Classification of clastic coastal depositional environments: *Sedimentary Geology*, v. 80, p. 139-150.
- BORCHARDT, G., 1989, Smectites, *in* Dixon, J.B., ed., *Minerals in Soil Environments: Minerals in Soil Environments*: Madison, WI, Soil Science Society of America, p. 675-727.
- BREA, M., MATHEOS, S., RAIGEMBORN, M., IGLESIAS, A., ZUCOL, A., and PRAMPÁRO, M., 2011, Paleocology and paleoenvironments of Podocarp trees in the Ameghino Petrified forest (Golfo San Jorge Basin, Patagonia, Argentina): Constraints for Early Paleogene paleoclimate: *Geologica Acta*, v. 9, p. 1-23.
- BREA, M., ZAMUNER, A., MATHEOS, S., IGLESIAS, A., and ZUCOL, A., 2008, Fossil wood of the Mimosoideae from the early Paleocene of Patagonia, Argentina: *Alcheringa*, v. 32, p. 427-441.
- BREA, M., MATHEOS, S., ZAMUNER, A., and GANUZA, D., 2005, Growth rings analysis of the Victor Szlapelis Fossil Forest, lower tertiary of Chubut, Argentina: *Ameghiniana*, v. 42, p. 407-418.
- CASTRO, L.N., FAZIO, A.M., SCASSO, R.A., TOURN, S.M., and SOREDA, M.E., 2008, Potential potassium deposits in Patagonia, Southeast Argentina, Third International Conference on the Geology of the Tethys: Aswan.
- CHAMLEY, H., 1989, *Clay Sedimentology*: Berlin, Germany, Springer-Verlag, 623 p.
- CHOI, K.S., DALRYMPLE, R.W., CHUN, S.S., and KIM, S.P., 2004, Sedimentology of modern, inclined heterolithic stratification (IHS) in the Macrotidal Han River delta, Korea: *Journal of Sedimentary Research*, v. 74, p. 677-689.
- CRERAR, E.E., and ARNOTT, R.W.C., 2007, Facies distribution and stratigraphic architecture of the Lower Cretaceous McMurray Formation, Lewis Property, northeastern Alberta: *Bulletin of Canadian Petroleum Geology*, v. 55, p. 99-124.
- DALRYMPLE, R.W., KNIGHT, R.J., ZAITLIN, B.A., and MIDDLETON, G.V., 1990, Dynamics and facies model of a macrotidal sand-bar complex, Cobequid Bay—Salmon River Estuary (Bay of Fundy), John Wiley & Sons, p. 577-612.
- DALRYMPLE, R.W., ZAITLIN, B.A., and BOYD, R., 1992, Estuarine Facies Models - Conceptual Basis and Stratigraphic Implications: *Journal of Sedimentary*

- Petrology, v. 62, p. 1130-1146.
- DEMKO, T.M., DUBIEL, R.F., and TOTMAN PARRISH, J., 1998, Plant taphonomy in incised valleys: implications for interpreting paleoclimate from fossil plants, *Geological Soc America*, p. 1119.
- DICKINSON, W.R., and SUCZEK, C.A., 1979, Plate-Tectonics and Sandstone Compositions: *Aapg Bulletin-American Association of Petroleum Geologists*, v. 63, p. 2164-2182.
- DICKINSON, W.R., BEARD, L.S., BRAKENRIDGE, G.R., ERJAVEC, J.L., FERGUSON, R.C., INMAN, K.F., KNEPP, R.A., LINDBERG, F.A., and RYBERG, P.T., 1983, Provenance of North-American Phanerozoic Sandstones in Relation to Tectonic Setting: *Geological Society of America Bulletin*, v. 94, p. 222-235.
- DIXON, J.B., 1989, Kaolin and Serpentine Group Minerals, *in* Dixon, J.B., ed., *Minerals in Soil Environments: Minerals in Soil Environments: Madison, Wi, Soil Science Society of America* p. 467-525.
- FANNING, D.S., KERAMIDAS, V.Z., and EL-DESOKY, M.A., 1989, Micas *in* Dixon, J.B., and Weed, S.B., eds., *Minerals in Soil Environments: Minerals in Soil Environments: Madison, WI, Soil Science Society of America*, p. 551-634.
- FENIES, H., DE RESSEQUIER, A., and TASTET, J.P., 1999, Intertidal clay-drape couplets (Gironde estuary, France): *Sedimentology*, v. 46, p. 1-15.
- FERUGLIO, E., 1949, Descripción geológica de la Patagonia, vol. II: Buenos Aires, Ministerio de Industria y Comercio de la Nación, Dirección General de Yacimientos Petrolíferos Fiscales, 1-349 p.
- FOLGUERA, A., ORTS, D., SPAGNUOLO, M., VERA, E.R., LITVAK, V., SAGRIPANTI, L., RAMOS, M.E., and RAMOS, V.A., A review of Late Cretaceous to Quaternary palaeogeography of the southern Andes: *Biological Journal of the Linnean Society*, v. 103, p. 250-268.
- FOLK, R.L., ANDREWS, P.B., and LEWIS, D.W., 1970, Detrital Sedimentary Rock Classification and Nomenclature for Use in New-Zealand: *New Zealand Journal of Geology and Geophysics*, v. 13, p. 937-&.
- GINSBERG, S.S., and PERILLO, G.M.E., 2004, Characteristics of tidal channels in a mesotidal Estuary of Argentina: *Journal of Coastal Research*, v. 20, p. 489-497.
- GLORIOSO, P.D., and FLATHER, R.A., 1997, The Patagonian Shelf tides: *Progress in Oceanography*, v. 40, p. 263-283.
- GLORIOSO, P.D., and SIMPSON, J.H., 1994, Numerical modeling of the M2 tide on the northern Patagonian shelf: *Continental Shelf Research*, v. 14, p. 267-278.
- GODIN, G., 1993, On Tidal Resonance: *Continental Shelf Research*, v. 13, p. 89-107.
- HAQ, B.U., HARDENBOL, J., and VAIL, P.R., 1987, Chronology of Fluctuating Sea Levels since the Triassic: *Science*, v. 235, p. 1156-1167.
- HARRIS, P.T., 1988, Large-scale bedforms as indicators of mutually evasive sand transport and the sequential infilling of wide-mouthed estuaries: *Sedimentary Geology*, v. 57, p. 273-298.
- IGLESIAS, A., 2007, ESTUDIO PALEOBOTÁNICO, PALEOECOLÓGICO Y PALEOAMBIENTAL EN SECUENCIAS DE LA FORMACIÓN SALAMANCA, DEL PALEOCENO INFERIOR EN EL SUR DE LA PROVINCIA DE CHUBUT, PATAGONIA, ARGENTINA: UNIVERSIDAD NACIONAL DE LA PLATA, La Plata, 244 p.

- IGLESIAS, A., WILF, P., JOHNSON, K.R., ZAMUNER, A.B., CUNEO, N.R., MATHEOS, S.D., and SINGER, B.S., 2007, A Paleocene lowland macroflora from Patagonia reveals significantly greater richness than North American analogs: *Geology*, v. 35, p. 947-950.
- JOUSSEIN, E., PETIT, S., CHURCHMAN, J., THENG, B., RIGHI, D., and DELVAUX, B., 2005, Halloysite clay minerals - A review: *Clay Minerals*, v. 40, p. 383-426.
- KRAUSE, J.M., BELLOSI, E.S., and RAIGEMBORN, M., 2010, Lateritized tephric palaeosols from Central Patagonia, Argentina: a southern high-latitude archive of Palaeogene global greenhouse conditions: *Sedimentology*.
- LECLAIR, S.F., 2002, Preservation of cross-strata due to the migration of subaqueous dunes: an experimental investigation: *Sedimentology*, v. 49, p. 1157-1180.
- LEEDER, M.R., 1999, *Sedimentology and sedimentary basins: from turbulence to tectonics*: Oxford, England, Wiley-Blackwell.
- LEGARRETA, L., and ULIANA, M.A., 1994, Asociaciones de fósiles y hiatos en el Supracretácico-Neógeno de Patagonia: una perspectiva estratigráfico-secuencial: *Amaghiniana*, v. 31, p. 257-281.
- LESTA, P.J., 1968, *Estratigrafía de la Cuenca del Golfo San Jorge: Actas de las Terceras Jornadas Geológicas Argentinas*
- MACELLARI, C.E., BARRIO, C.A., and MANASSERO, M.J., 1989, Upper Cretaceous to Paleocene depositional sequences and sandstone petrography of southwestern Patagonia (Argentina and Chile): *Journal of South American Earth Sciences*, v. 2 p. 223-239.
- MACK, G.H., JAMES, W.C., and MONGER, H.C., 1993, Classification of Paleosols: *Geological Society of America Bulletin*, v. 105, p. 129-136.
- MALUMIÁN, N., and NÁÑEZ, C., 2011, The Late Cretaceous-Cenozoic transgressions in Patagonia and the Fuegian Andes: foraminifera, palaeoecology, and palaeogeography: *Biological Journal of the Linnean Society*, v. 103, p. 269-288.
- MARSHALL, L.G., BUTLER, R.F., DRAKE, R.E., and CURTIS, G.H., 1981, Calibration of the beginning of the age of mammals in Patagonia: *Science*, v. 212, p. 43-45.
- MARSHALL, L.G., SEMPERE, T., and BUTLER, R.F., 1997, Chronostratigraphy of the mammal-bearing Paleocene of South America: *Journal of South American Earth Sciences*, v. 10, p. 49-70.
- MARTINEZ, G.A., 1992, Paleoambiente de la Formación Salamanca en La Pampa María Santísima, Departamento Sarmiento, Provincia de Chubut: *Revista de la Asociación Geológica Argentina*, v. 47, p. 293-303.
- MATHEOS, S., BREA, M., GANUZA, D., and ZAMUNER, A., 2001, Sedimentología y paleoecología del Terciario inferior en el sur de la provincia del Chubut, República Argentina: *Asociación Argentina de Sedimentología Revista*, v. 8, p. 93-104.
- MENDEZ, I., 1966, Foraminíferos, edad y correlaciones estratigráficas del Salamanquense de Punta Peligro (45x30'S; 67x11'W), provincia del Chubut: *Revista de la Asociación Geológica Argentina*, v. 21, p. 127-157.
- MILLER, K.G., KOMINZ, M.A., BROWNING, J.V., WRIGHT, J.D., MOUNTAIN, G.S., KATZ, M.E., SUGARMAN, P.J., CRAMER, B.S., CHRISTIE-BLICK, N., and PEKAR, S.F., 2005, The Phanerozoic record of global sea-level change: *Science*, v. 310, p. 1293-1298.
- NESBITT, H.W., and YOUNG, G.M., 1982, *Early Proterozoic Climates and Plate Motions*

- Inferred from Major Element Chemistry of Lutites: *Nature*, v. 299, p. 715-717.
- NOUIDAR, M., and CHELLAI, E.H., 2001, Facies and sequence stratigraphy of an estuarine incised-valley fill: Lower Aptian Bouzergoun Formation, Agadir Basin, Morocco: *Cretaceous Research*, v. 22, p. 93-104.
- ODIN, G.S., and FULLAGAR, P.D., 1988, Geological Significance of the Glaucony Facies, *in* Odin, G.S., ed., *Green Marine Clays: Amsterdam, The Netherlands, Elsevier Science Publishers*, p. 445.
- PANKHURST, R.J., WEAVER, S.D., HERV, F., and LARRONDO, P., 1999, Mesozoic-Cenozoic evolution of the North Patagonian Batholith in Aysén, southern Chile: *Journal of the Geological Society of London*, v. 156, p. 673-694.
- PASQUINI, A.I., DEPETRIS, P.J., GAIERO, D.M., and PROBST, J.L., 2005, Material sources, chemical weathering, and physical denudation in the Chubut River basin (Patagonia, Argentina): Implications for Andean rivers: *Journal of Geology*, v. 113, p. 451-469.
- POTTER, P.E., 1994, Modern Sands of South-America - Composition, Provenance and Global Significance: *Geologische Rundschau*, v. 83, p. 212-232.
- POTTER, P.E., 1997, The Mesozoic and Cenozoic paleodrainage of South America: a natural history: *Journal of South American Earth Sciences*, v. 10, p. 331-344.
- RAIGEMBORN, M., 2006, Analisis Composicional y Procedencia de la Fomacion Peñas Coloradas, Grupo Rio Chico (Paleoceno Superior-Eoceno?), en la Region Oriental de la Cuenca del Golfo San Jorge, Chubut, Argentina: *Latin American Journal of Sedimentology and Basin Analysis*, v. 13, p. 65-87.
- RICARDI-BRANCO, F., BRANCO, F.C., GARCIA, R.J.F., FARIA, R.S., PEREIRA, S.Y., PORTUGAL, R., PESSEDA, L.C., and PEREIRA, P.R.B., 2009, Plant Accumulations Along the Itanhaem River Basin, Southern Coast of Sao Paulo State, Brazil, *SEPM*, p. 416.
- RODRIGUEZ, J.F.R., and LITKE, R., 2001, Petroleum generation and accumulation in the Golfo San Jorge Basin, Argentina: a basin modeling study: *Marine and Petroleum Geology*, v. 18, p. 995-1028.
- SCAFATI, L., MELENDI, D.L., and WOLKHEIMER, W., 2009, A Danian subtropical lacustrine palynobiota from South America (Bororó Formation, San Jorge Basin, Patagonia - Argentina): *Geologica Acta*, v. 7, p. 35-61.
- SHANMUGAM, G., POFFENBERGER, M., and ALAVA, J.T., 2000, Tide-dominated estuarine facies in the Hollin and Napo ("T" and "U") formations (Cretaceous), Sacha field, Oriente basin, Ecuador: *AAPG Bulletin-American Association of Petroleum Geologists*, v. 84, p. 652-682.
- SINGER, A., 1980, The paleoclimatic interpretation of clay minerals in soils and weathering profiles, Elsevier, p. 303-326.
- SWAN, A.R.H., and SANDILANDS, M., 1995, *Introduction to Geological Data Analysis: Oxford, England, Blackwell Science Ltd.*, 446 p.
- SYLWAN, C., 2001, Geology of the Golfo San Jorge Basin, Argentina: *Journal of Iberian Geology*, v. 27, p. 123-157.
- TAPE, C.H., COWAN, C.A., and RUNKEL, A.C., 2003, Tidal-bundle sequences in the Jordan Sandstone (Upper Cambrian), southeastern Minnesota, USA: Evidence for tides along inboard shorelines of the Sauk epicontinental sea, *SEPM*, p. 354.
- ULIANA, M.A., and BIDDLE, K.T., 1988, Mesozoic-Cenozoic paleogeographic and geodynamic evolution of southern South America, p. 172-190.

- UMAZANO, A.M., BELLOSI, E.S., VISCONTI, G., JALFIN, G.A., and MELCHOR, R.N., 2009, Sedimentary record of a Late Cretaceous volcanic arc in central Patagonia: petrography, geochemistry and provenance of fluvial volcanoclastic deposits of the Bajo Barreal Formation, San Jorge Basin, Argentina: *Cretaceous Research*, v. 30, p. 749-766.
- URIEN, C.M., ZAMBRANO, J.J., and YRIGOYEN, M.R., 1995, Petroleum basins of southern South America: an overview, *in* Tankard, A.J., Soruco, R.S., and Welsink, H.J., eds., *Petroleum Basin of South America: AAPG Memoirs*, American Association of Petroleum Geologists, Yacimientos Petroliferos Fiscales Bolivianos, Academia Nacional de Ciencias de Bolivia, p. 63-63.
- WHITE, P.D., and SCHIEBOUT, J., 2008, Paleogene paleosols and changes in pedogenesis during the initial Eocene thermal maximum: Big Bend National Park, Texas, USA: *Geological Society of America Bulletin*, v. 120, p. 1347-1361.
- WILLIS, B.J., and TANG, H., 2010, Three-Dimensional Connectivity of Point-Bar Deposits: *Journal of Sedimentary Research*, v. 80, p. 440-454.
- ZHANG, J.L., and ZHANG, Z.J., 2008, Sedimentary facies of the Silurian tide-dominated paleo-estuary of the Tazhong area in the Tarim Basin: *Petroleum Science*, v. 5, p. 95-104.
- ZHAO, M., Ji, J.F., CHEN, Z.Y., CHEN, X.M., CU, X.D., and WANG, Y.S., 2011, Evolution of kaolinite subgroup minerals and mixed-layer illite/smectite in the Paleogene Damintun Depression in Liaohé Basin of China and its implication for paleotemperature: *Science China-Earth Sciences*, v. 54, p. 73-83.

**APPENDIX A: Stratigraphic Columns**

Graphic Log scale in (m)	Facies	Comments	Paleoenvironmental Interpretation	Paleocurrents
	10	Brownish Black Muds	Widespread coastal swamp	
	8	Transitional Sands To Silty Clays	Abandoned tidal channel fill	
	1a	White Cross-Bedded Sands	Tidal bars deposited in tidal channels near head of estuary	
	3	Heterolithic Cross-Bedded Sands	Subtidal bars on a sand shoal containing mutually evasive ebb and flood channels	
	6	Wavy-Bedded Sands and Silts	Deeper water tidal bars	
	4	Swaley-Hummocky Cross-Bedded Sands	Reworked tidal bars	
	9	Wispy-Bedded Clays	Low-energy Shelf Muds	
	5	Poorly Sorted Litharenites and Clays	Transgressive Lag	

**Dromedary Hill**



Graphic Log scale in (m)	Facies	Comments	Paleoenvironmental Interpretation	Paleocurrents
	10	Brownish Black Muds	Widespread coastal swamp	
	8	Transitional sands to silty clays	Abandoned channel fill	
	1a	White Cross-Bedded Sands	Tidal bars deposited in tidal channels near head of estuary	

Cerro Colorado

Graphic Log scale in (m)	Facies	Comments	Paleoenvironmental Interpretation	Paleocurrents
	8	Transitional sands to silty clays	Abandoned tidal channel fill	
	1a	White Cross-Bedded Sands	Tidal bars deposited in tidal channels near head of estuary	
	3	Heterolithic Cross-Bedded Sands	Subtidal bars on a sand shoal containing mutually evasive ebb and flood channels	

OR-2 \*\*no datum

Graphic Log scale in (m)	Facies	Comments	Paleoenvironmental Interpretation	Paleocurrents
	10	Brownish Black Muds	Widespread coastal swamp	
	7	Accretion-bedded sands and silts	Lateral point bars accretions filling in tidal channels	
	1a	White Cross-Bedded Sands	Tidal bars deposited in tidal channels near head of estuary	

OR-1

Graphic Log scale in (m)	Facies	Comments	Paleoenvironmental Interpretation	Paleocurrents
	10	Brownish black muds	Widespread coastal swamp	
	8	Transitional sands to silty clays	Abandoned tidal channel fill	
	7	Accretion-bedded sands and silts	Lateral point bar accretions filling in tidal channels	
	1a	White Cross-Bedded Sands	Tidal bars deposited in tidal channels near head of estuary	
	8	Transitional sands to silty clays	Abandoned tidal channel fill	
	7	Accretion-bedded sands and silts	Lateral point bar accretions filling in tidal channels	
	3	Heterolithic Cross-Bedded Sands	Subtidal bars on a sand shoal containing mutually evasive ebb and flood channels	

PL-1 \*composite section with PL-H

Graphic Log scale in (m)	Facies	Comments	Paleoenvironmental Interpretation	Paleocurrents
	10	Brownish black muds	Widespread coastal swamp	
	8	Transitional sands to silty clays	Abandoned tidal channel fill	
	1a	White Cross-Bedded Sands	Tidal bars deposited in tidal channels near head of estuary	

PL-2

Graphic Log scale in (m)	Facies	Comments	Paleoenvironmental Interpretation	Paleocurrents
	10	Brownish black muds	Widespread coastal swamp	
	8	Transitional sands to silty clays	Abandoned tidal channel fill	
	1a	White Cross-Bedded Sands	Tidal bars deposited in tidal channels near head of estuary	
	8	Transitional sands to silty clays	Abandoned tidal channel fill	
	3	Heterolithic cross-bedded sands	Subtidal bars on a sand shoal containing mutually evasive ebb and flood channels	

PL-3, 4, 5 \*composite section \*\*no datum

Graphic Log scale in (m)	Facies	Comments	Paleoenvironmental Interpretation	Paleocurrents
	10	Brownish black muds	Widespread coastal swamp	
	7	Accretion-bedded sands and silts	Lateral point bar accretions filling in tidal channels	
	1a	White Cross-Bedded Sands	Tidal bars deposited in tidal channels near head of estuary	
	3	Heterolithic cross-bedded sands	Subtidal bars on a sand shoal containing mutually evasive ebb and flood channels	

PL-A

Graphic Log scale in (m)	Facies	Comments	Paleoenvironmental Interpretation	Paleocurrents
	10	Brownish black muds	Widespread coastal swamp	
	8	Transitional sands to silty clays	Abandoned tidal channel fill	
	7	Accretion-bedded sands and silts	Lateral point bar accretions filling in tidal channels	
	1a	White Cross-Bedded Sands	Tidal bars deposited in tidal channels near head of estuary	
	3	Heterolithic cross-bedded sands	Subtidal bars on a sand shoal containing mutually evasive ebb and flood channels	

PL-B

Graphic Log scale in (m)	Facies	Comments	Paleoenvironmental Interpretation	Paleocurrents
	10	Brownish black muds	Widespread coastal swamp	
	8	Transitional sands to silty clays	Abandoned tidal channel fill	
	7	Accretion-bedded sands and silts	Lateral point bar accretions filling in tidal channels	
	1a	White Cross-Bedded Sands	Tidal bars deposited in tidal channels near head of estuary	
	3	Heterolithic cross-bedded sands	Subtidal bars on a sand shoal containing mutually evasive ebb and flood channels	
	6	Wavy-bedded sands and silts	Deeper water tidal bars	

PL-C

Graphic Log scale in (m)	Facies	Comments	Paleoenvironmental Interpretation	Paleocurrents
	7	Accretion-bedded sands and silts	Lateral point bar accretions filling in tidal channels	
	1a	White Cross-Bedded Sands	Tidal bars deposited in tidal channels near head of estuary	
	3	Heterolithic cross-bedded sands	Subtidal bars on a sand shoal containing mutually evasive ebb and flood channels	
	6	Wavy-bedded sands and silts	Deeper water tidal bars	

PL-D

Graphic Log scale in (m)	Facies	Comments	Paleoenvironmental Interpretation	Paleocurrents
	8	Transitional sands to silty clays	Abandoned tidal channel fill	
	7	Accretion-bedded sands and silts	Lateral point bar accretions filling in tidal channels	
	1a	White Cross-Bedded Sands	Tidal bars deposited in tidal channels near head of estuary	
	3	Heterolithic cross-bedded sands	Subtidal bars on a sand shoal containing mutually evasive ebb and flood channels	
	6	Wavy-bedded sands and silts	Deeper water tidal bars	

PL-E



Graphic Log scale in (m)	Facies	Comments	Paleoenvironmental Interpretation	Paleocurrents
	7	Accretion-bedded sands and silts	Lateral point bar accretions filling in tidal channels	
	1a	White Cross-Bedded Sands	Tidal bars deposited in tidal channels near head of estuary	
	3	Heterolithic cross-bedded sands	Subtidal bars on a sand shoal containing mutually evasive ebb and flood channels	
	6	Wavy-bedded sands and silts	Deeper water tidal bars	

PL-F

Graphic Log scale in (m)	Facies	Comments	Paleoenvironmental Interpretation	Paleocurrents
	10	Brownish black muds	Widespread coastal swamp	
	8	Transitional sands to silty clays	Abandoned tidal channel fill	
	7	Accretion-bedded sands and silts	Lateral point bar accretions filling in tidal channels	
	1a	White Cross-Bedded Sands	Tidal bars deposited in tidal channels near head of estuary	
	1b	Unidirectional Cross-Bedded Sands	Microdelta	
	1a	White Cross-Bedded Sands	Tidal bars deposited in tidal channels near fluvial headwaters	

PL-G




















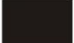


Graphic Log scale in (m)	Facies	Comments	Paleoenvironmental Interpretation	Paleocurrents
	10	Brownish black muds	Widespread coastal swamp	
	8	Transitional sands to silty clays	Abandoned tidal channel fill	
	7	Accretion-bedded sands and silts	Lateral point bar accretions filling in tidal channels	
	1a	White Cross-Bedded Sands	Tidal bars deposited in tidal channels near head of estuary	
	1b	Unidirectional Cross-Bedded Sands	Microdelta	

PL-I

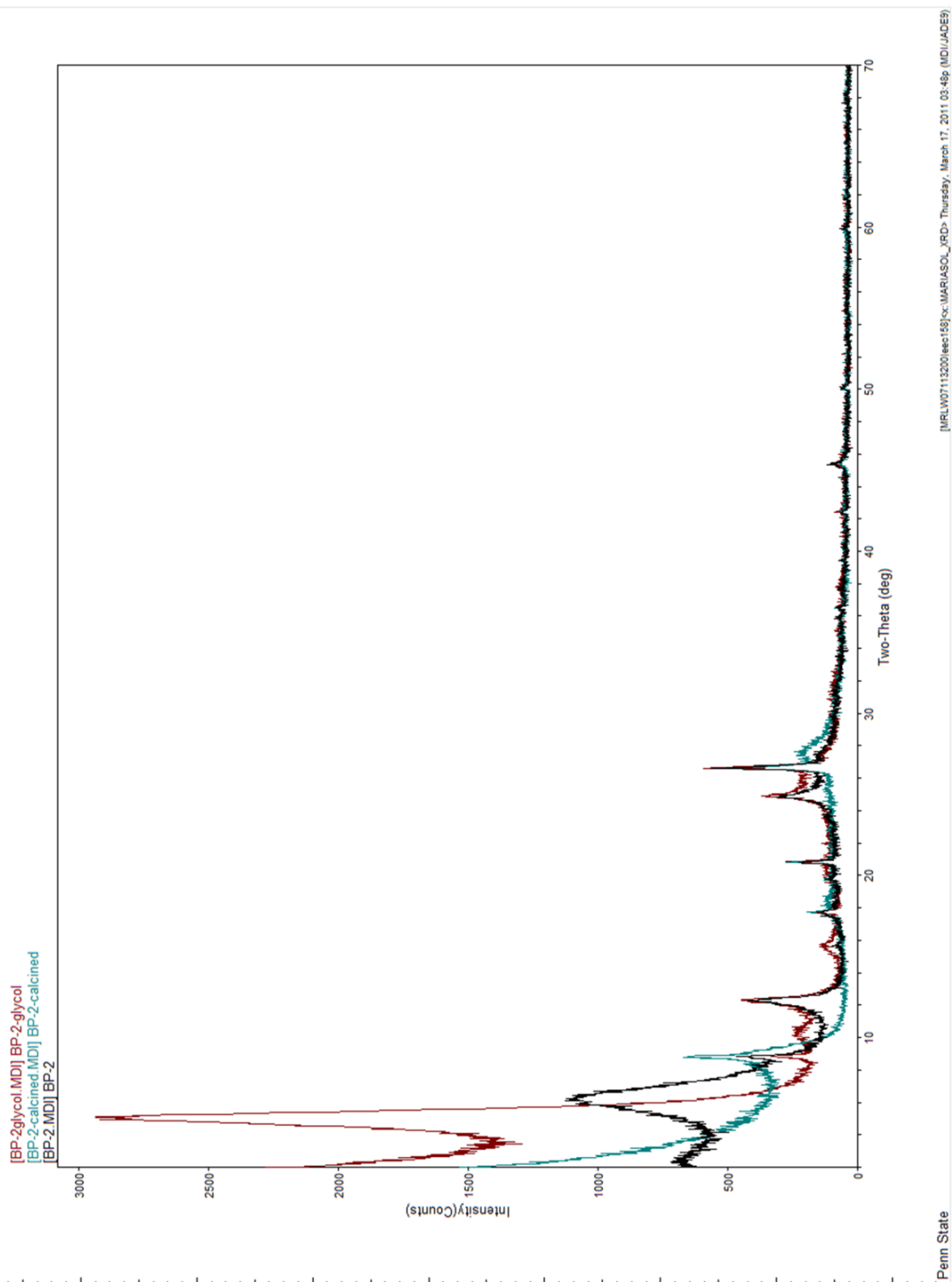
Graphic Log scale in (m)	Facies	Comments	Paleoenvironmental Interpretation	Paleocurrents
	8	Transitional sands to silty clays		
		Unidirectional steeply dipping cross-bedded sand		
	6	Wavy-bedded silts and sands	Lagoonal deposits	
		Coquina	storm deposits	
	6	Wavy-bedded silts and sands	Lagoonal deposits	
5	Poorly-sorted Litharenites and clays	Transgressive Lag		

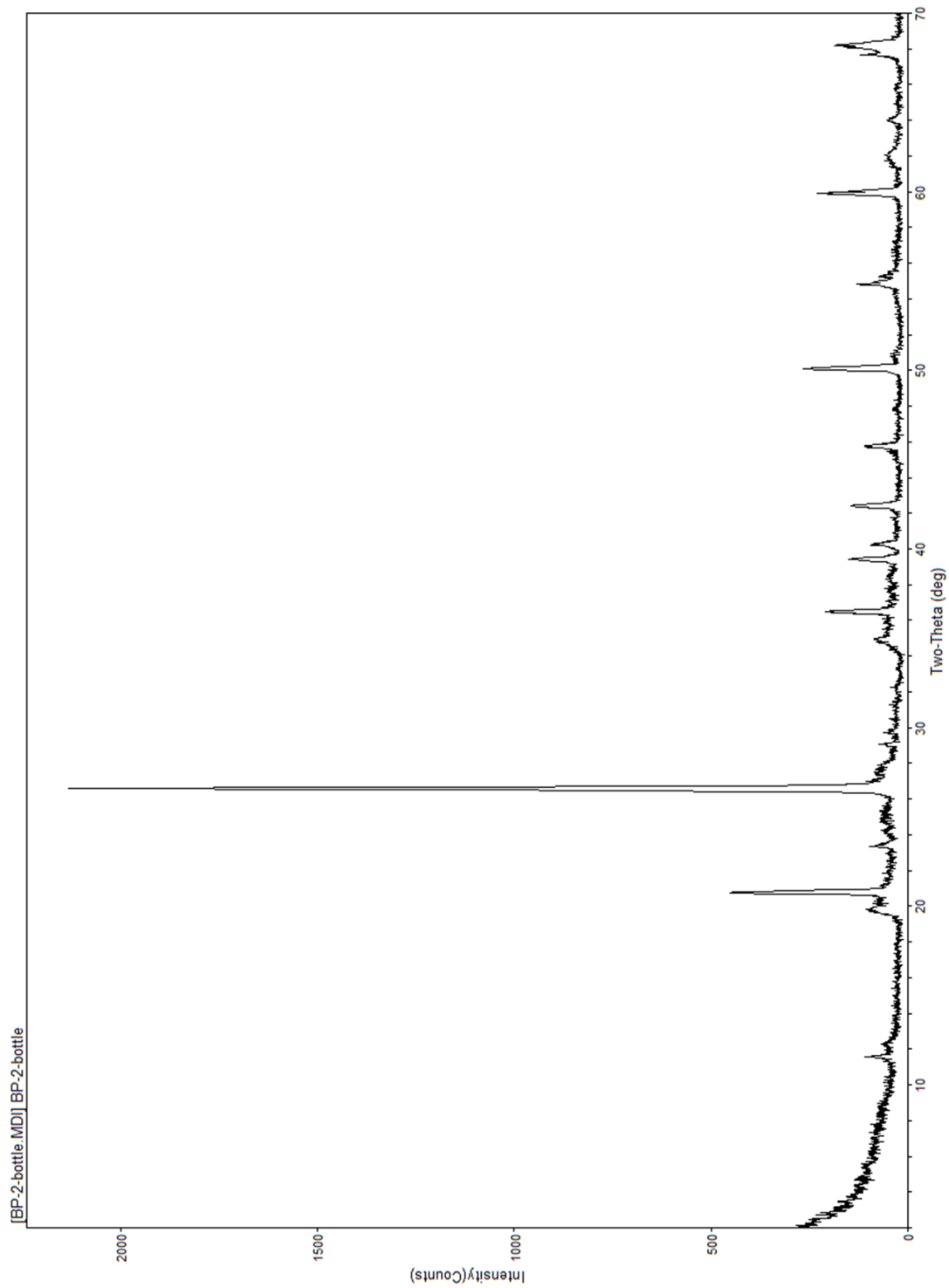
Rancho Grande

## Legend

	trough cross bedding		plant leaves
	flaser bedding		plant hash
	shark teeth		symmetric ripples
	nodules		planar cross stratification
	wispy bedding		accretion sets
	swaley bedding		mudstone facies
	arenicolites burrows		sandstone facies
	mottled texture		siltstone facies
	shell fossil		iron cemented layer
	starfish		paleosol
	gypsum		worm burrow

## APPENDIX B: XRD Patterns

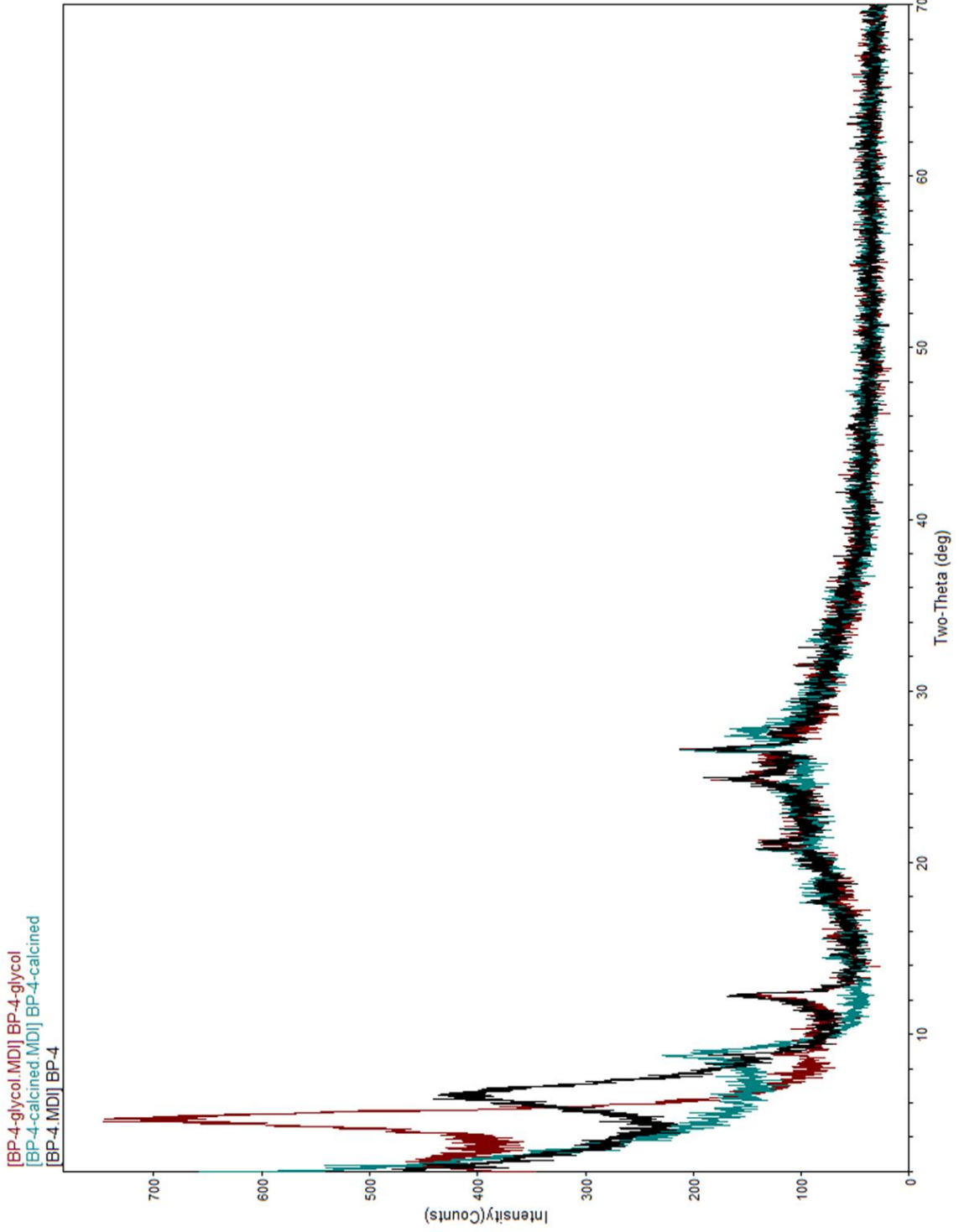




[BP-2-bottle.MD] BP-2-bottle

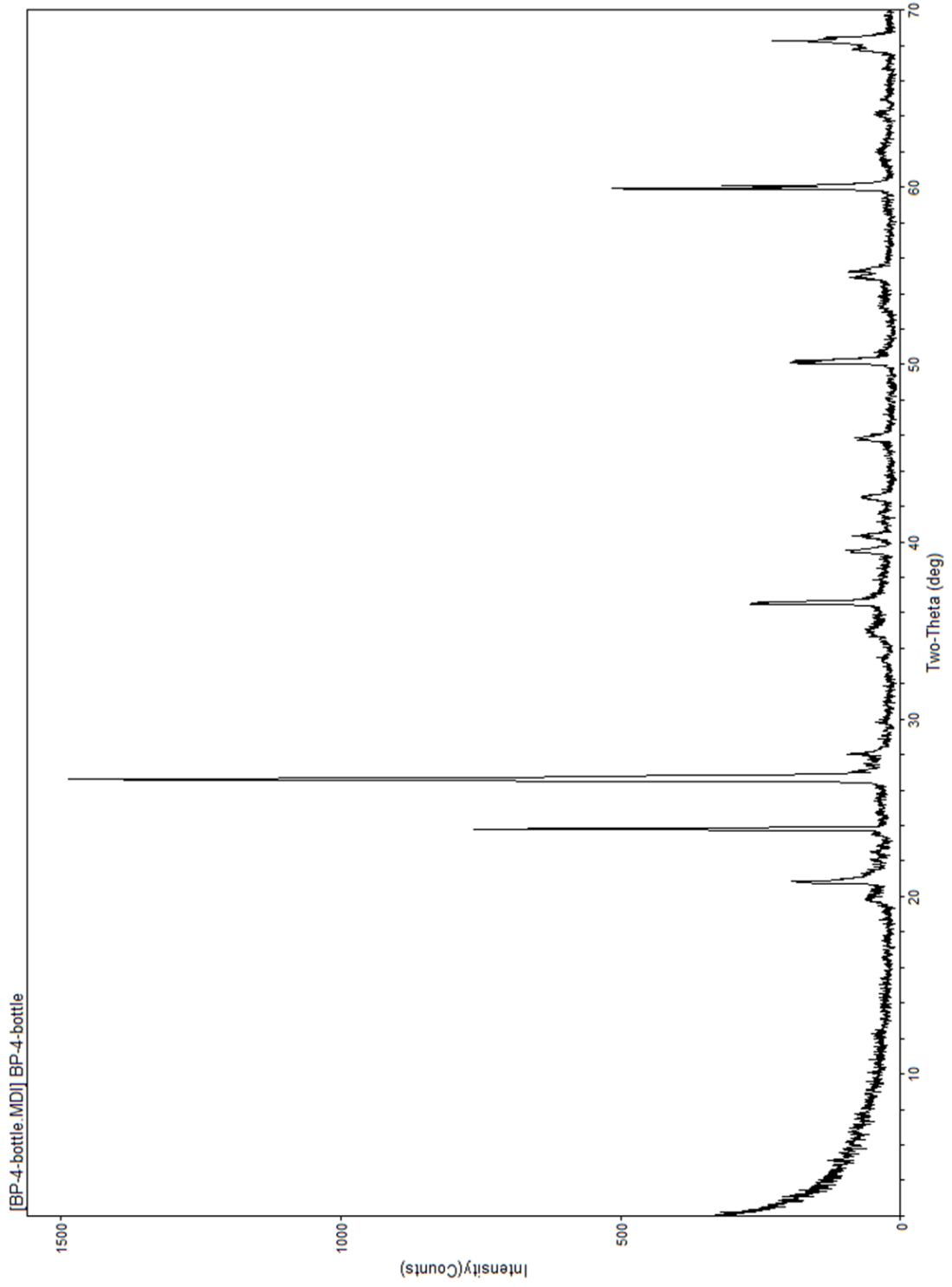
[MRLW07113200.lee158]sc:MARIASOL\_XRD> Thursday, March 17, 2011 03:50p (MDI/JADE9)

Penn State



[MRLW07113200]eoc159]c:\MARIASOL\_XRD> Wednesday, March 23, 2011 11:09a (MDI/JADE9)

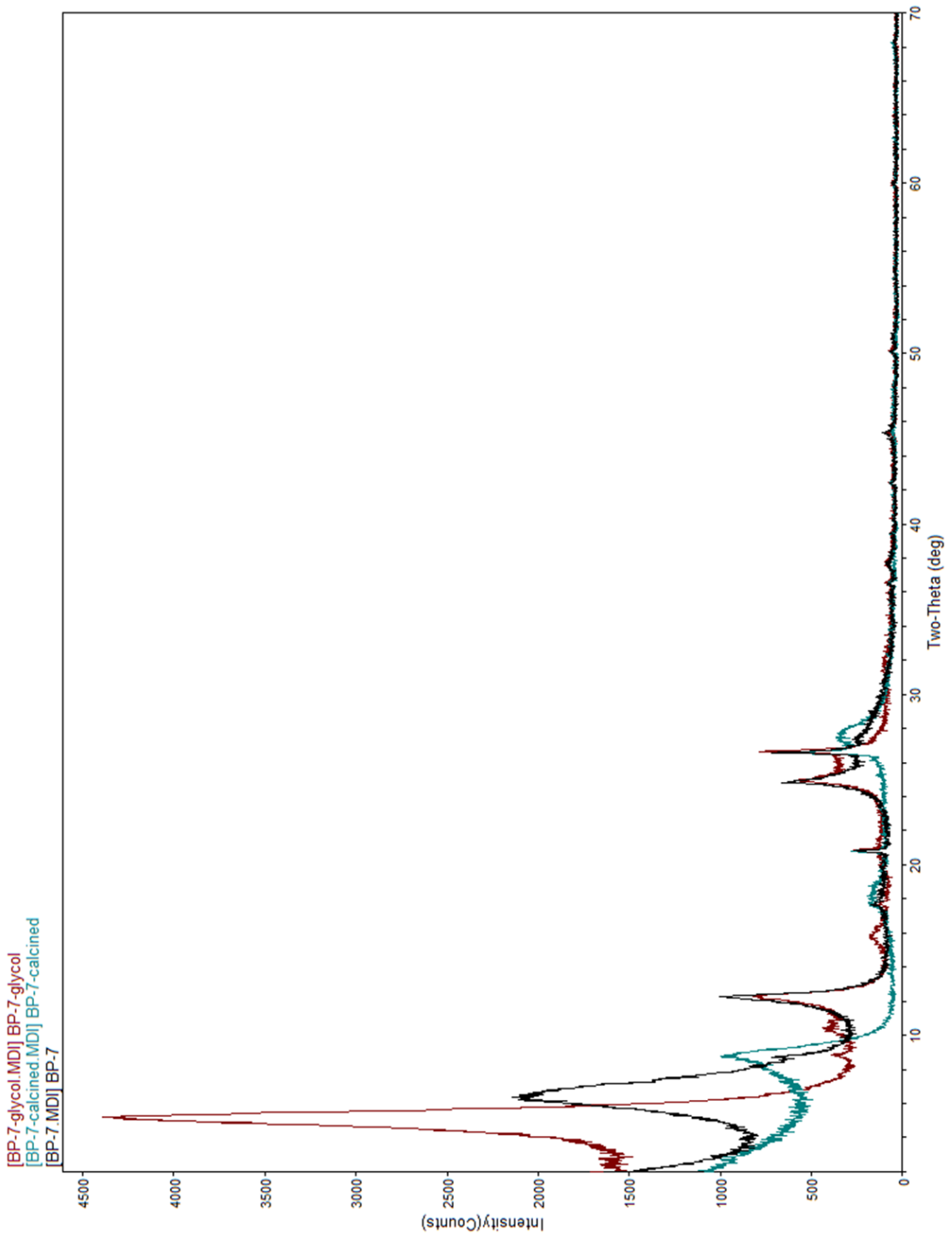
Penn State



[MRLW07113200]ec159]cx:MARIA SOL\_XRD> Wednesday, March 23, 2011 11:24a (MDI/JADE9)

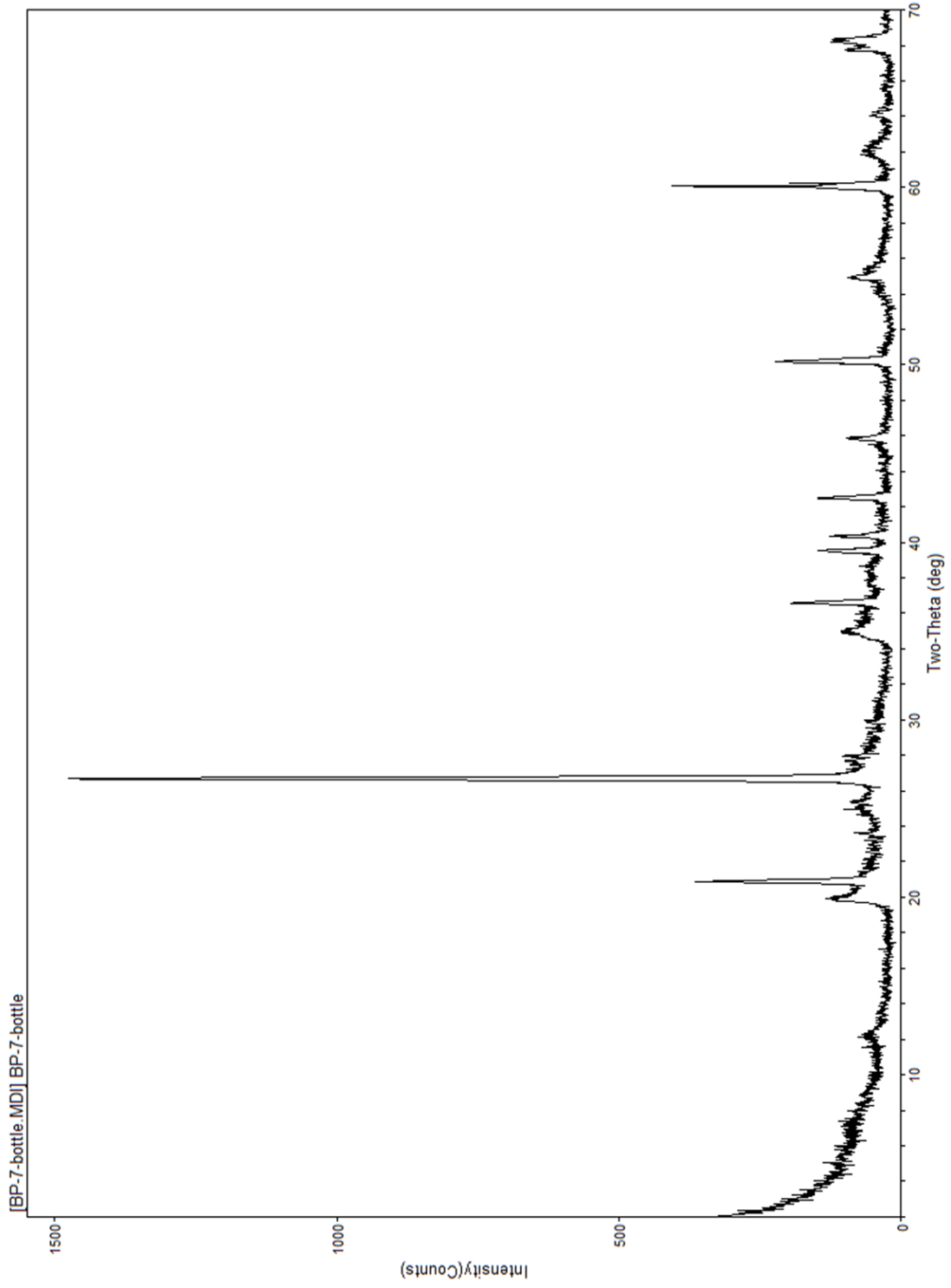
Penn State





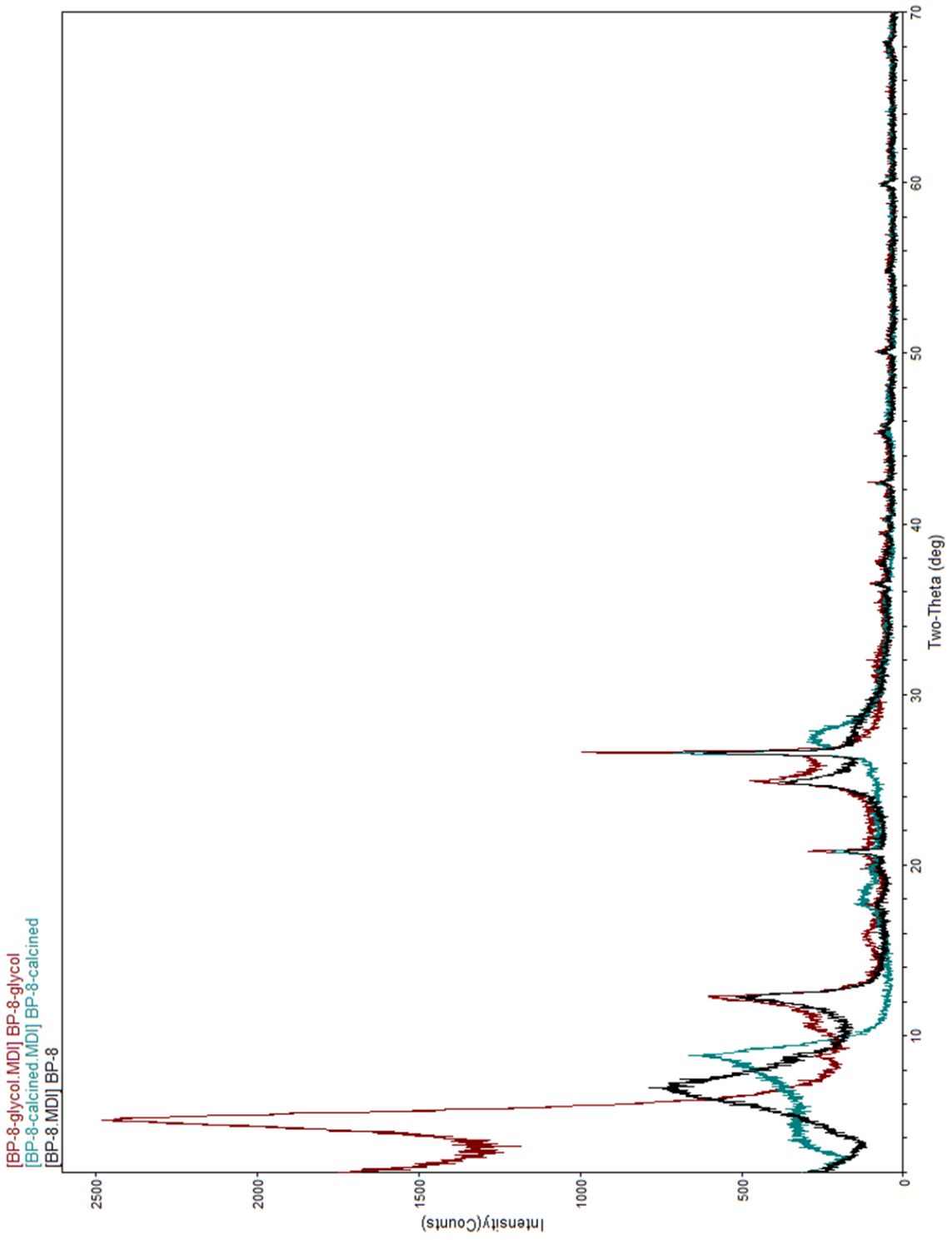
[MRLW07113200]ec159]sc:\MARIASOL\_XRD> Wednesday, March 23, 2011 10:33a (MDI/JADE9)

Penn State



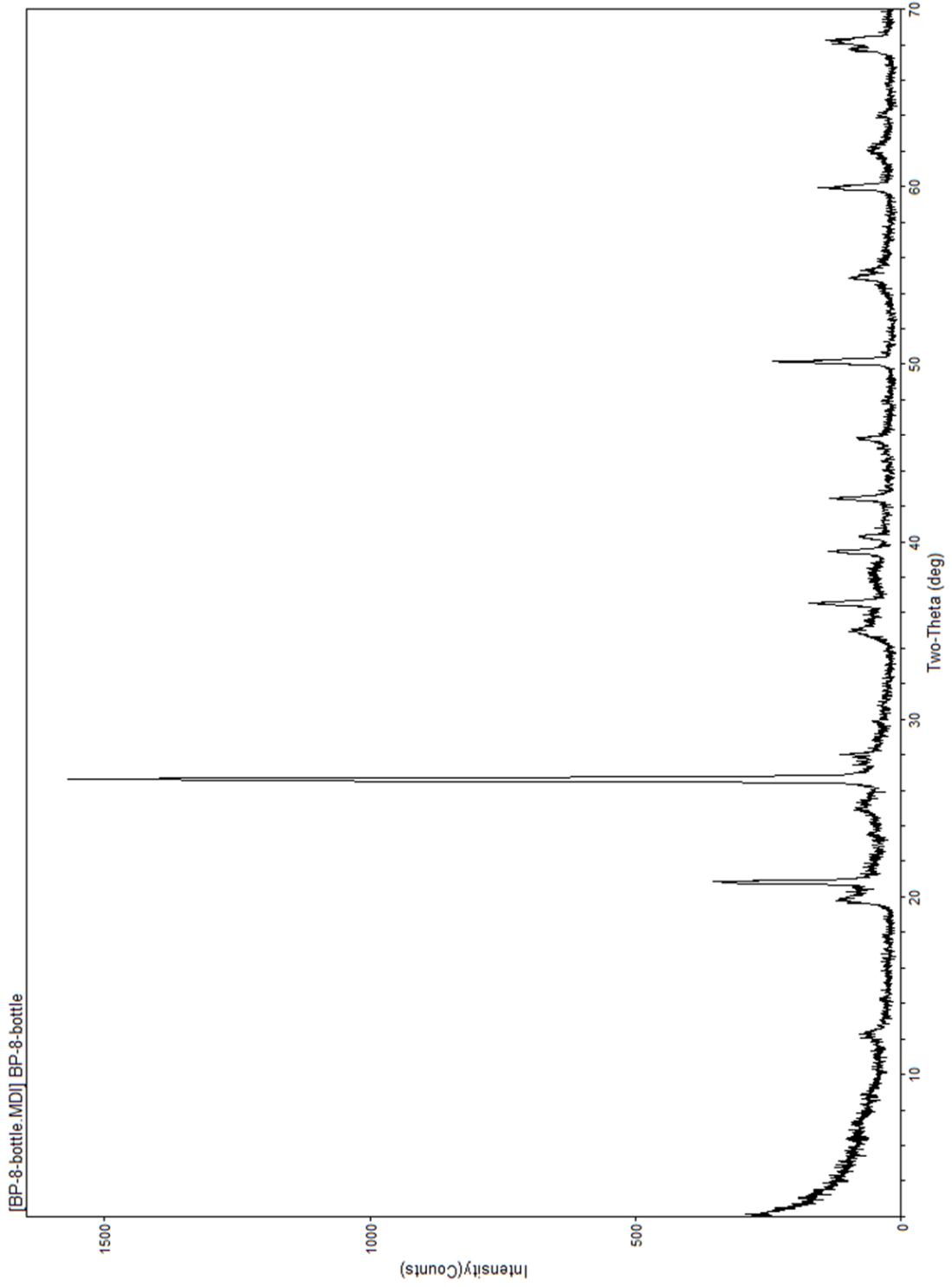
[MRLW07113200]ec159]cx:MARIA SOL\_XRD> Wednesday, March 23, 2011 10:35a (MDI/JADE9)

Penn State



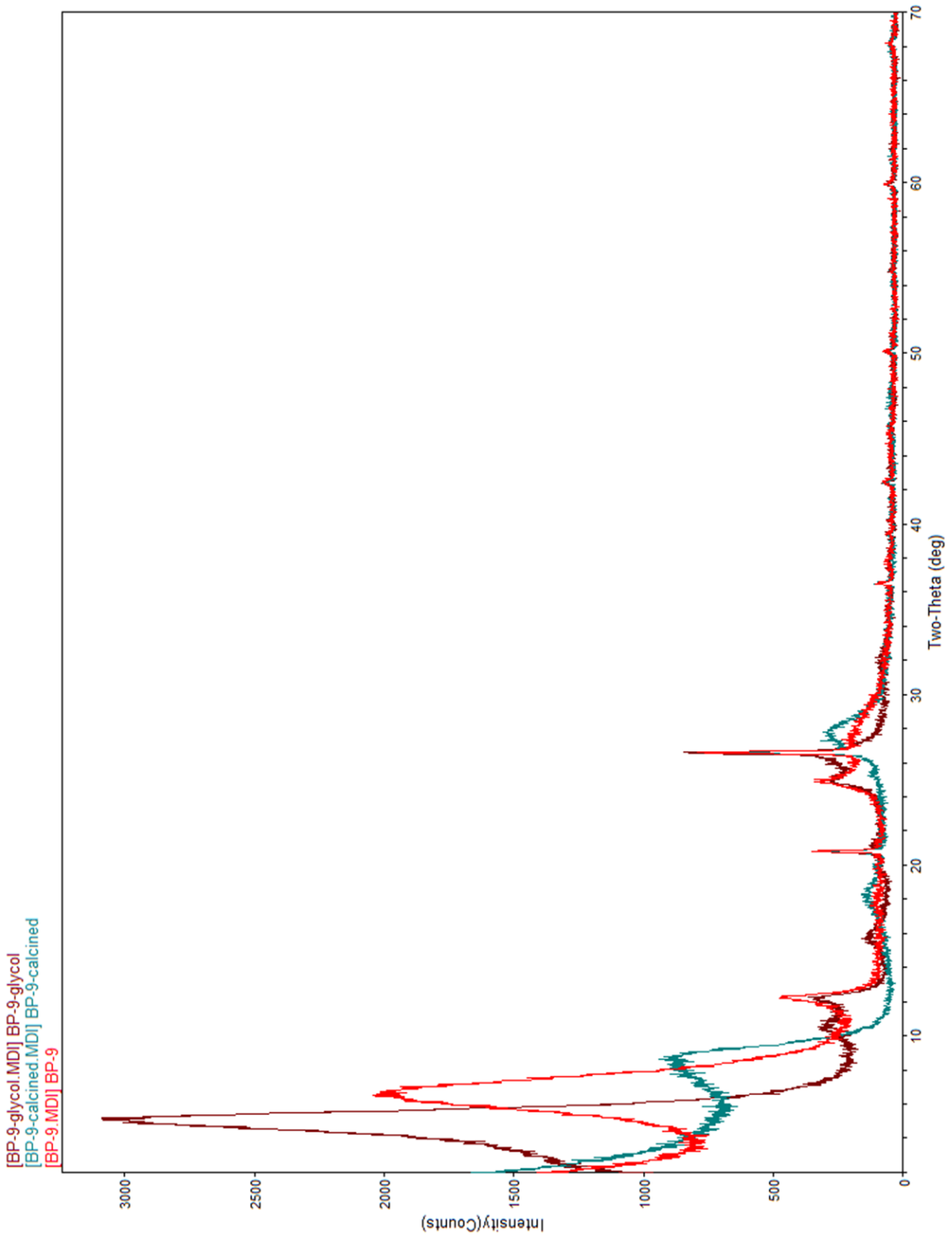
[MRLW07113200]eect159]c:\MARIASOL\_XRD> Wednesday, March 16, 2011 04:36p (MDI/JADE9)

Penn State



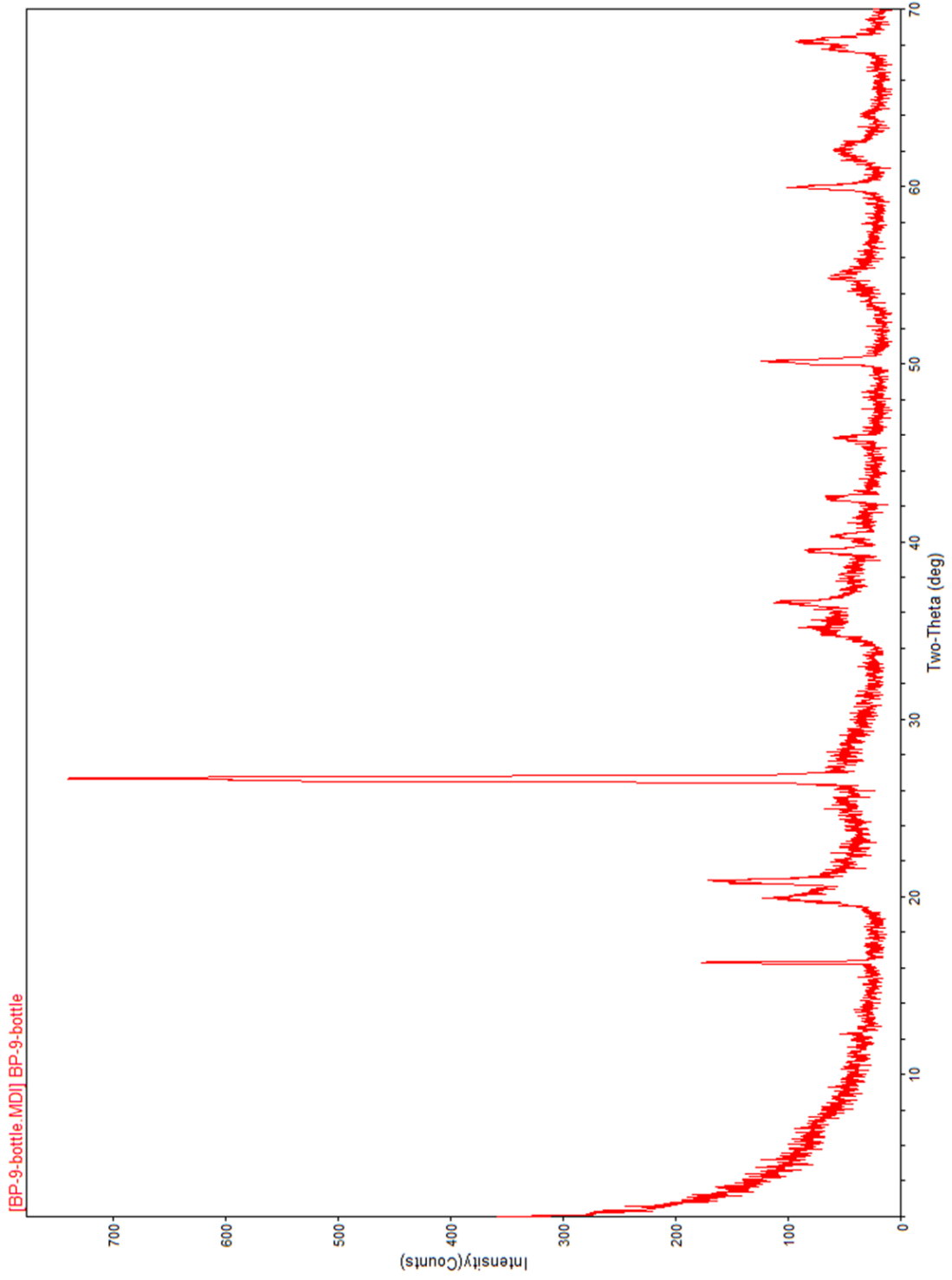
[MRLW07113200[eeec159]sc:\MARIASOL\_XRD> Wednesday, March 16, 2011 04:38p (MDI/JADE9)

Penn State



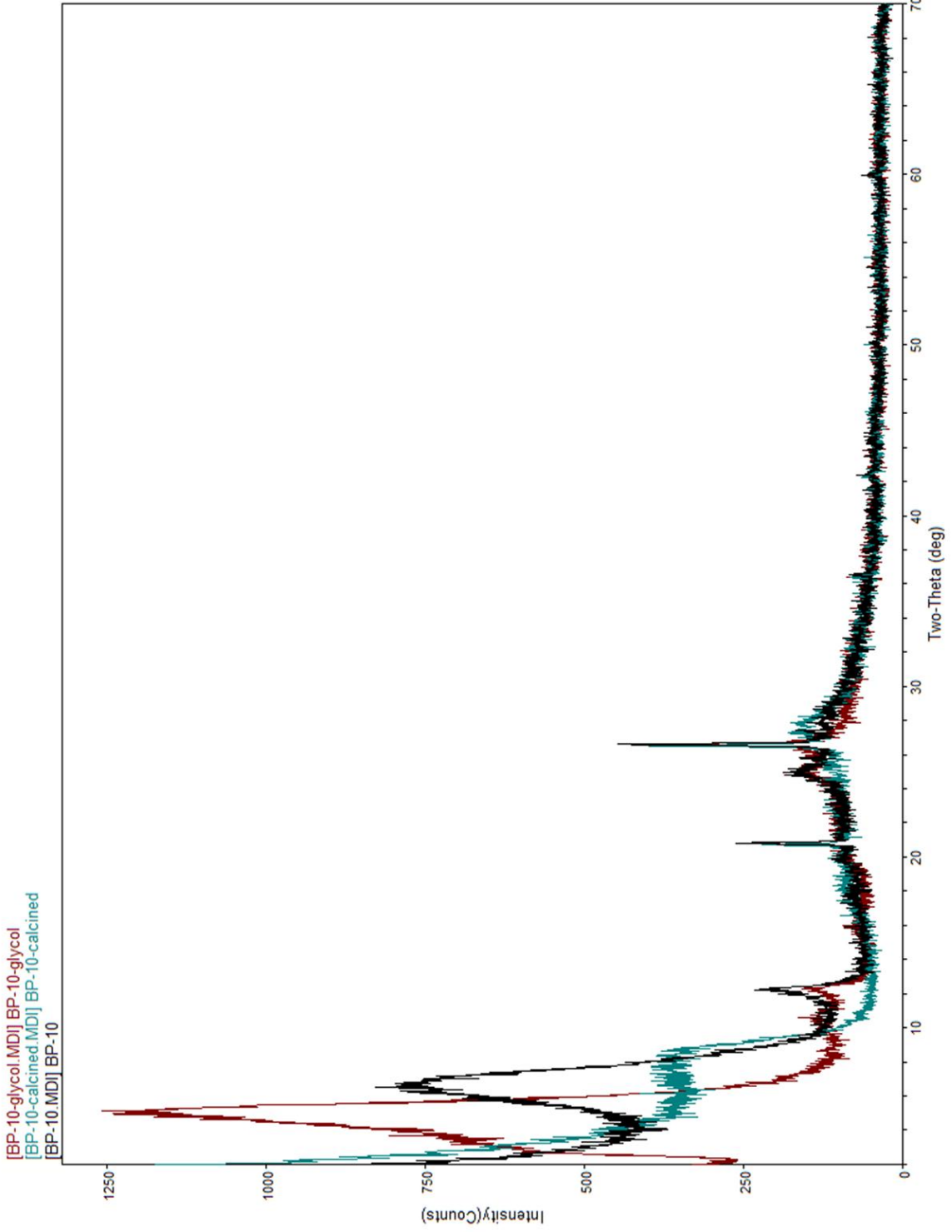
[MRLW07113200]eect159]c:\MARIASOL\_XRD> Wednesday, March 23, 2011 09:02a (MDI/JADE9)

Penn State



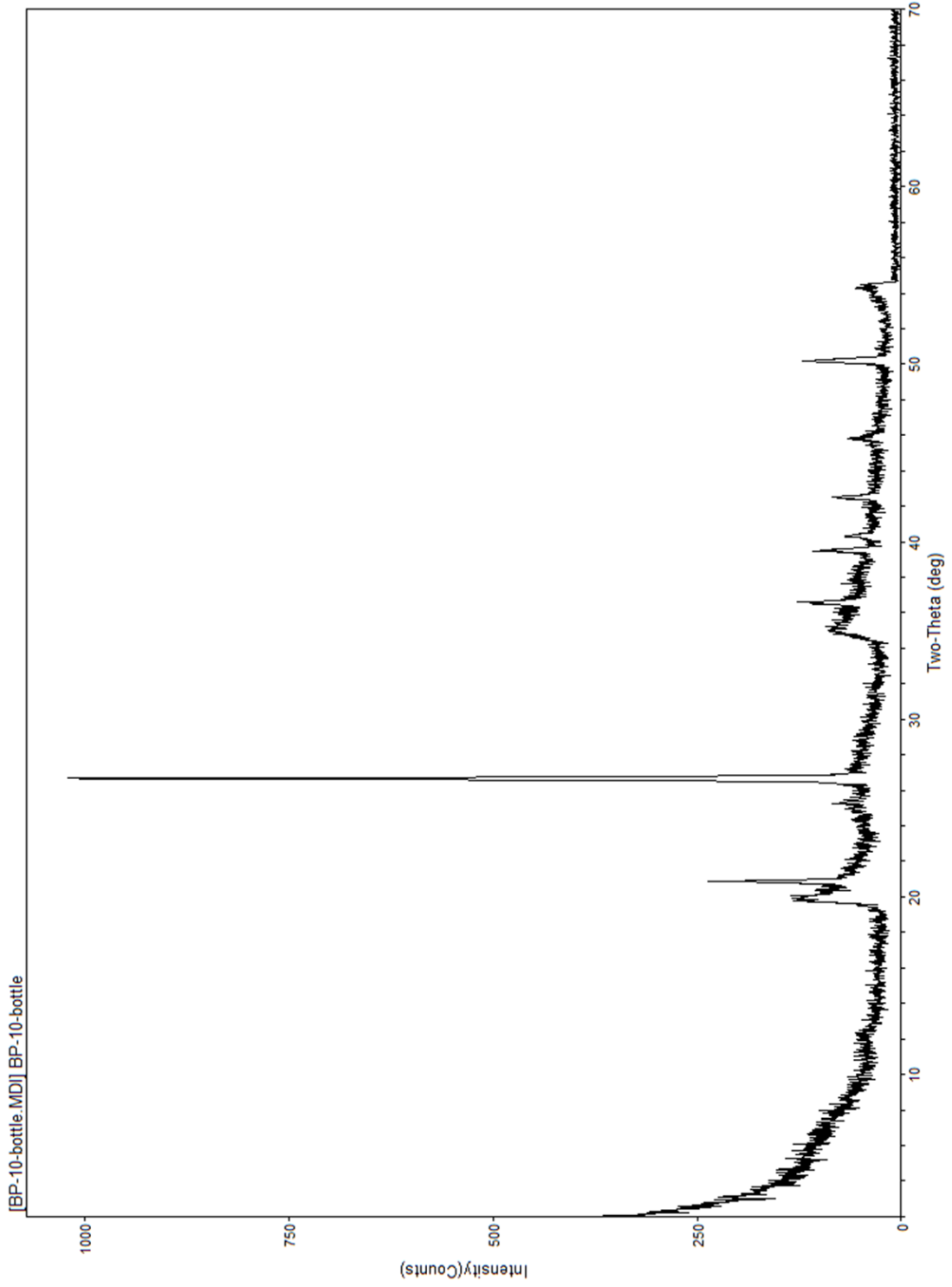
[MRLW07113200[eecl159]sc:MARIA SOL\_XRD> Wednesday, March 23, 2011 09:03a (MDI/JADE9)

Penn State



[MRLW07113200[ec168]sc:MARIA SOL\_XRD> Wednesday, March 16, 2011 03:32p (MDI/JADE9)

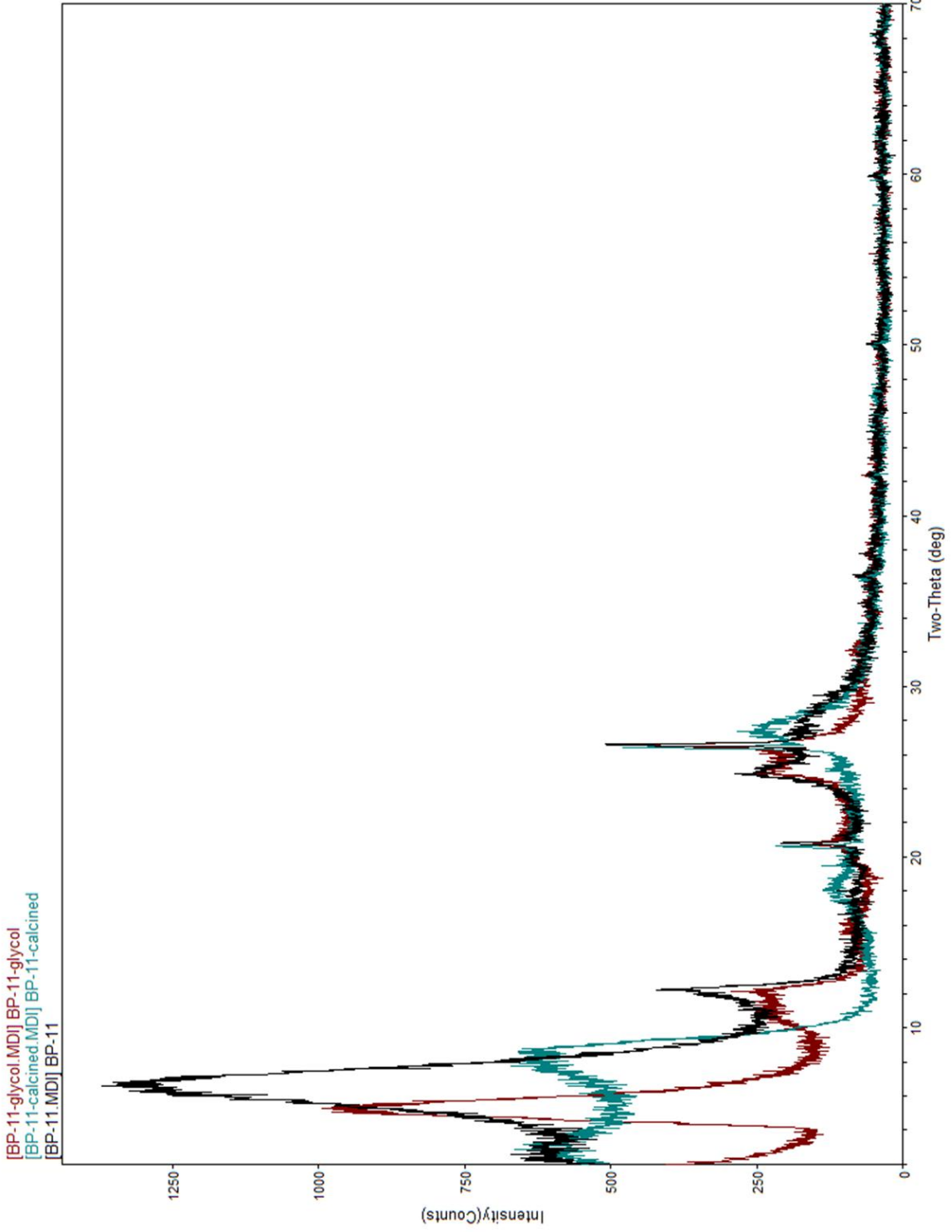
Penn State



[MRLW07113200]ec158]sc:MARIA SOL\_XRD> Wednesday, March 16, 2011 03:34p (MDI/JADE9)

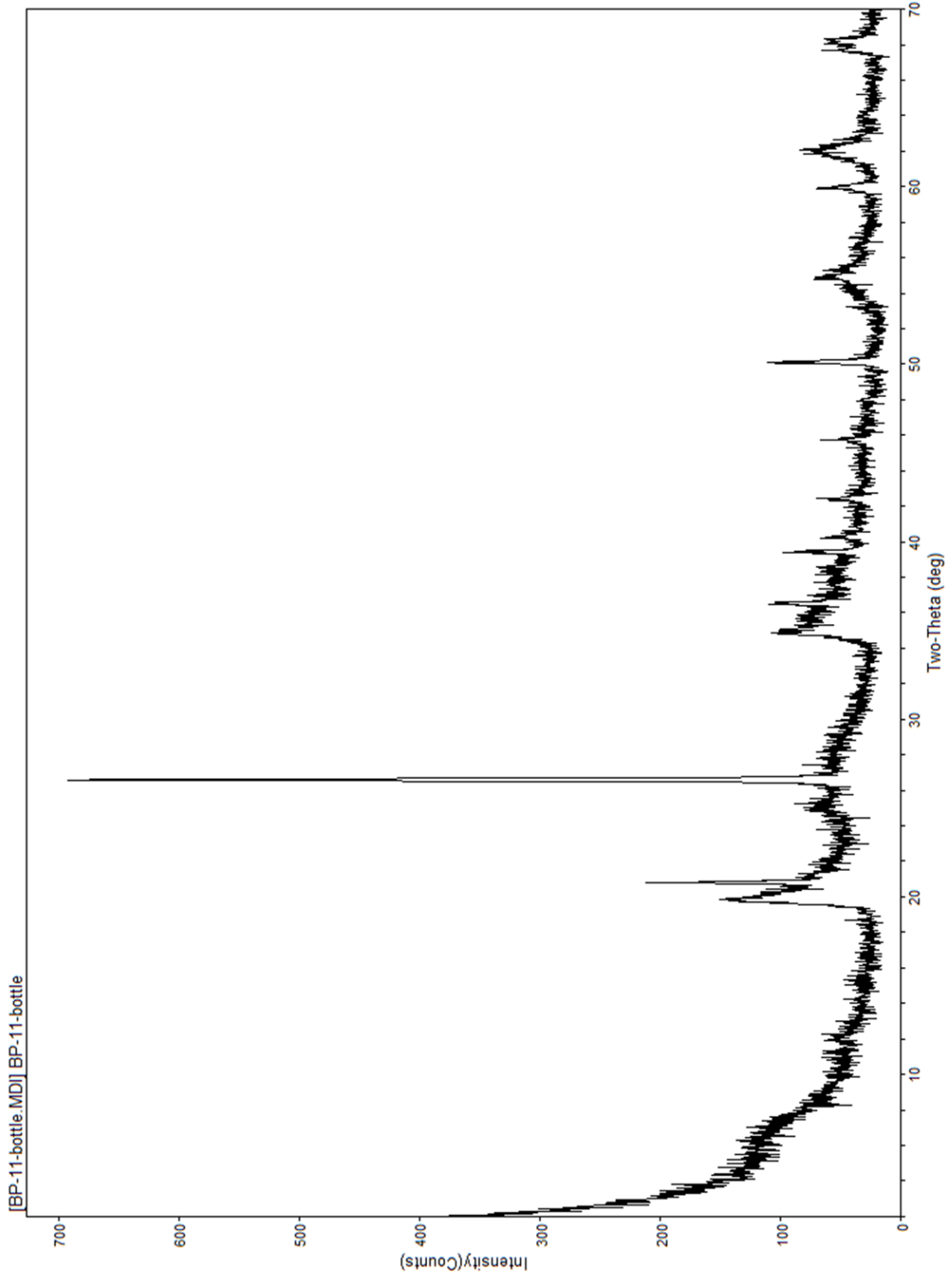
Penn State





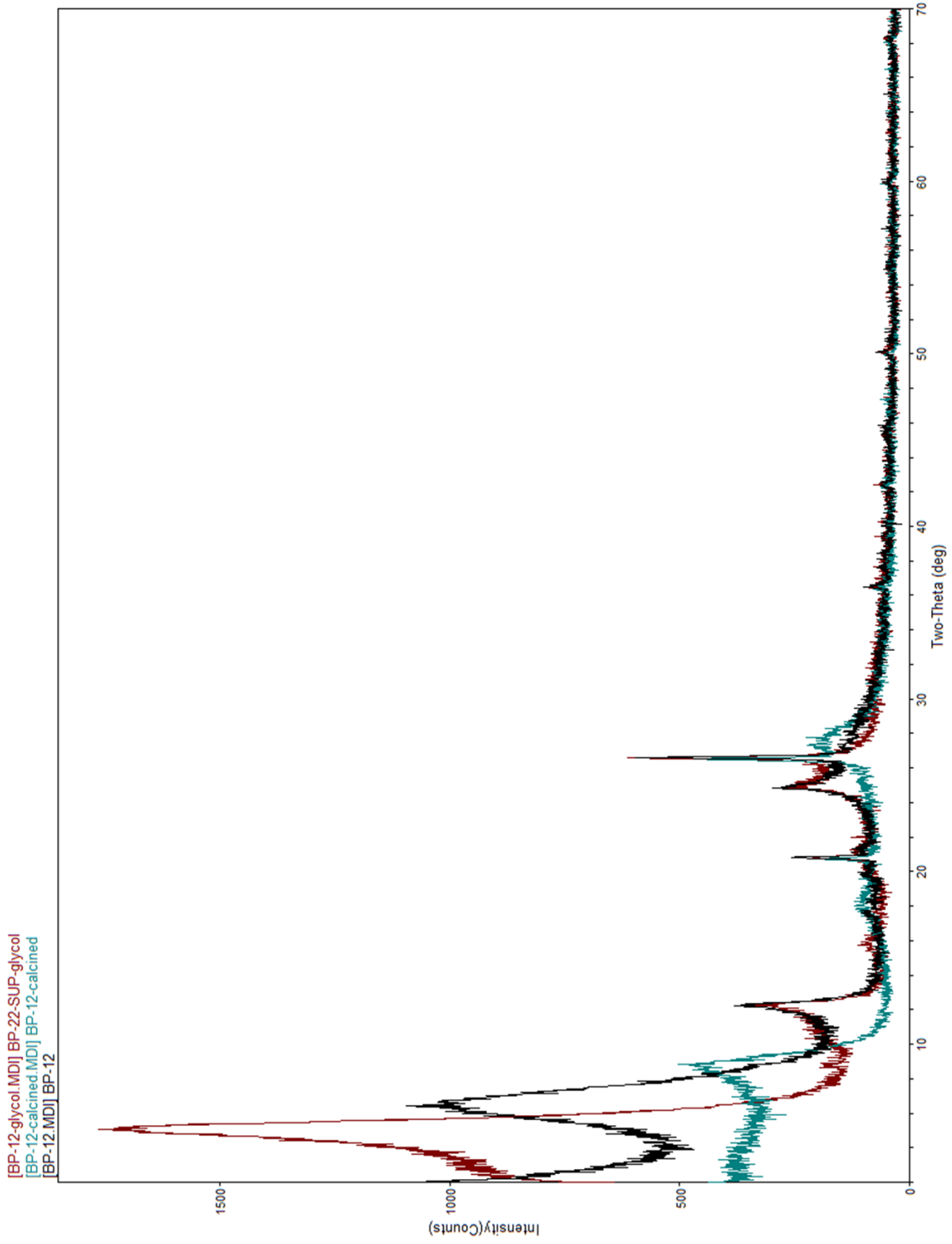
[MRLW07113200[ec168]sc:MARIA SOL\_XRD> Wednesday, March 16, 2011 04:49p (MDI/JADE9)

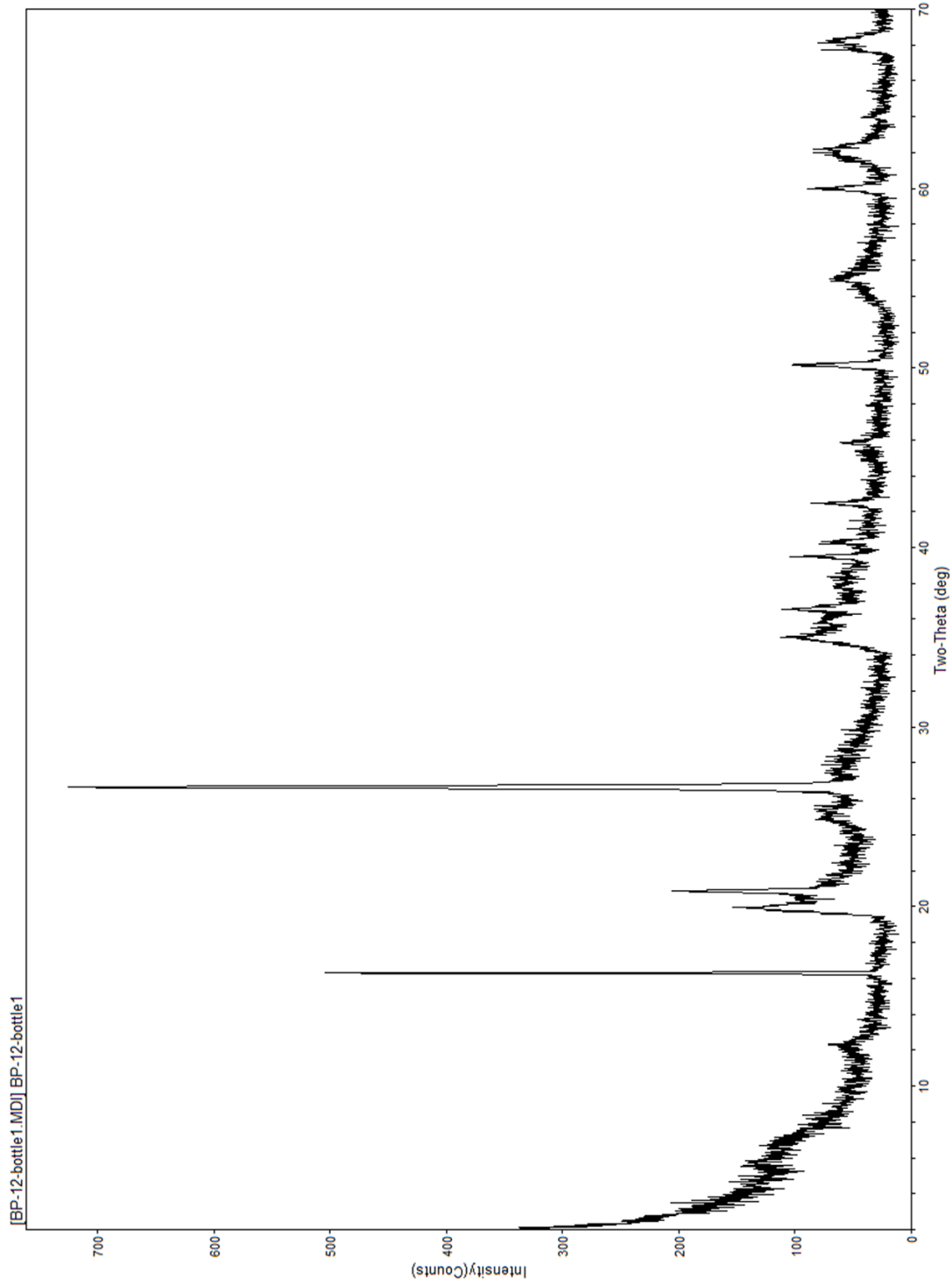
Penn State



[MRLW07113200[eeect159]sc:\MARIASOL\_XRD> Wednesday, March 16, 2011 04:50p (MDI/JADE9)

Penn State

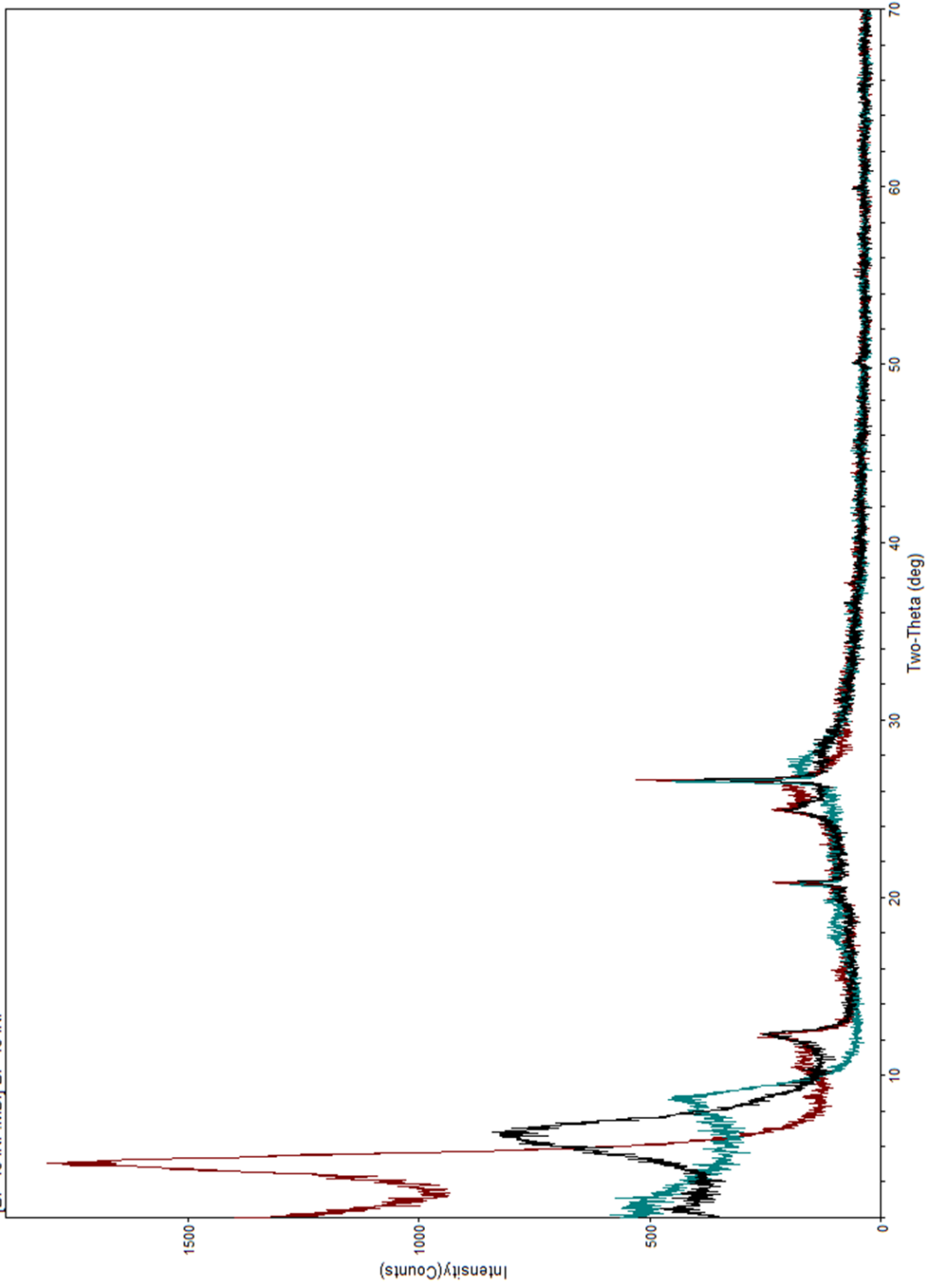


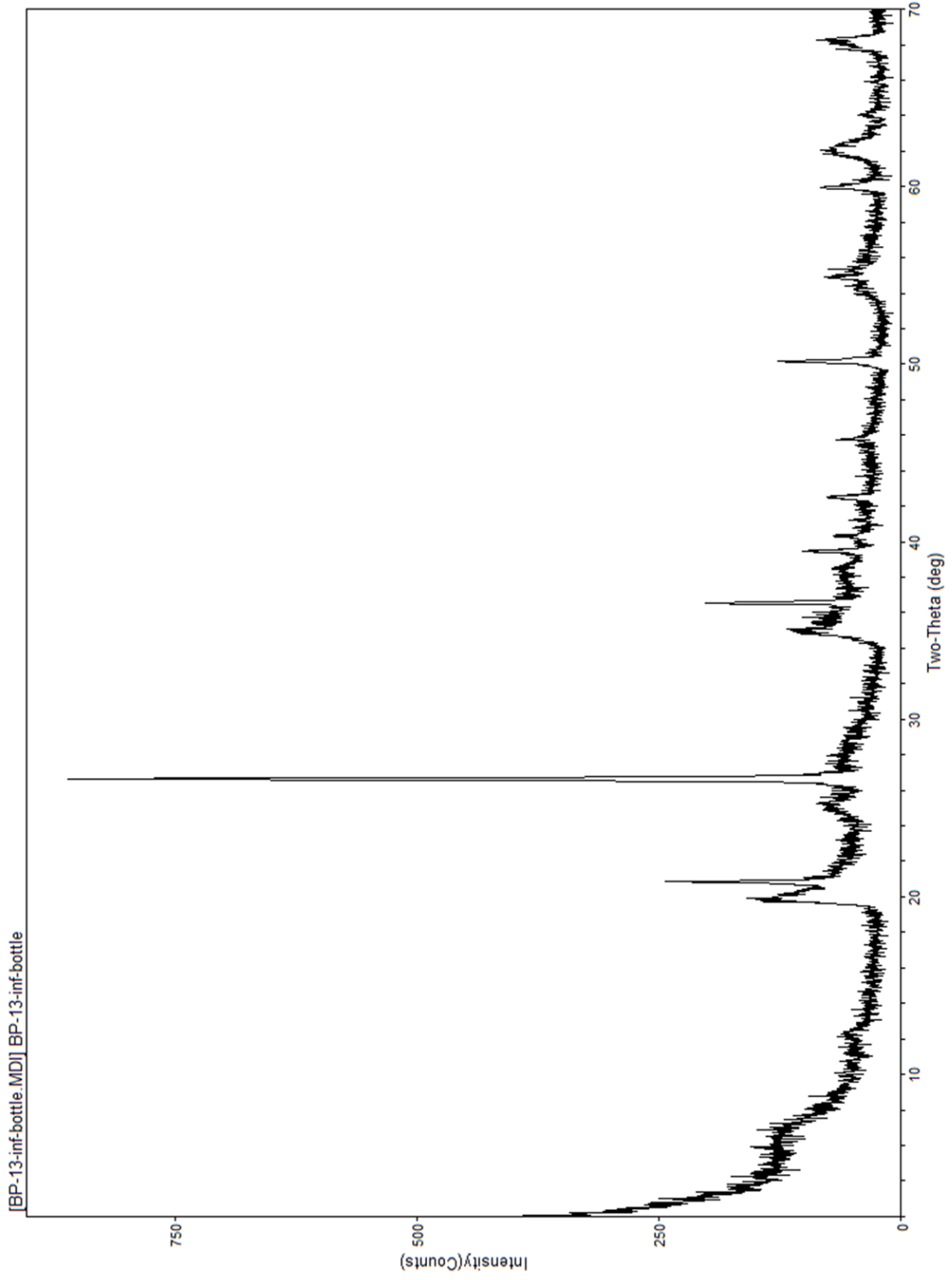


[MRLW0713200]lec169[cc:\MARIASO\_VRD> Thursday, March 17, 2011 04:06p (MD\JADE9)

Penn State

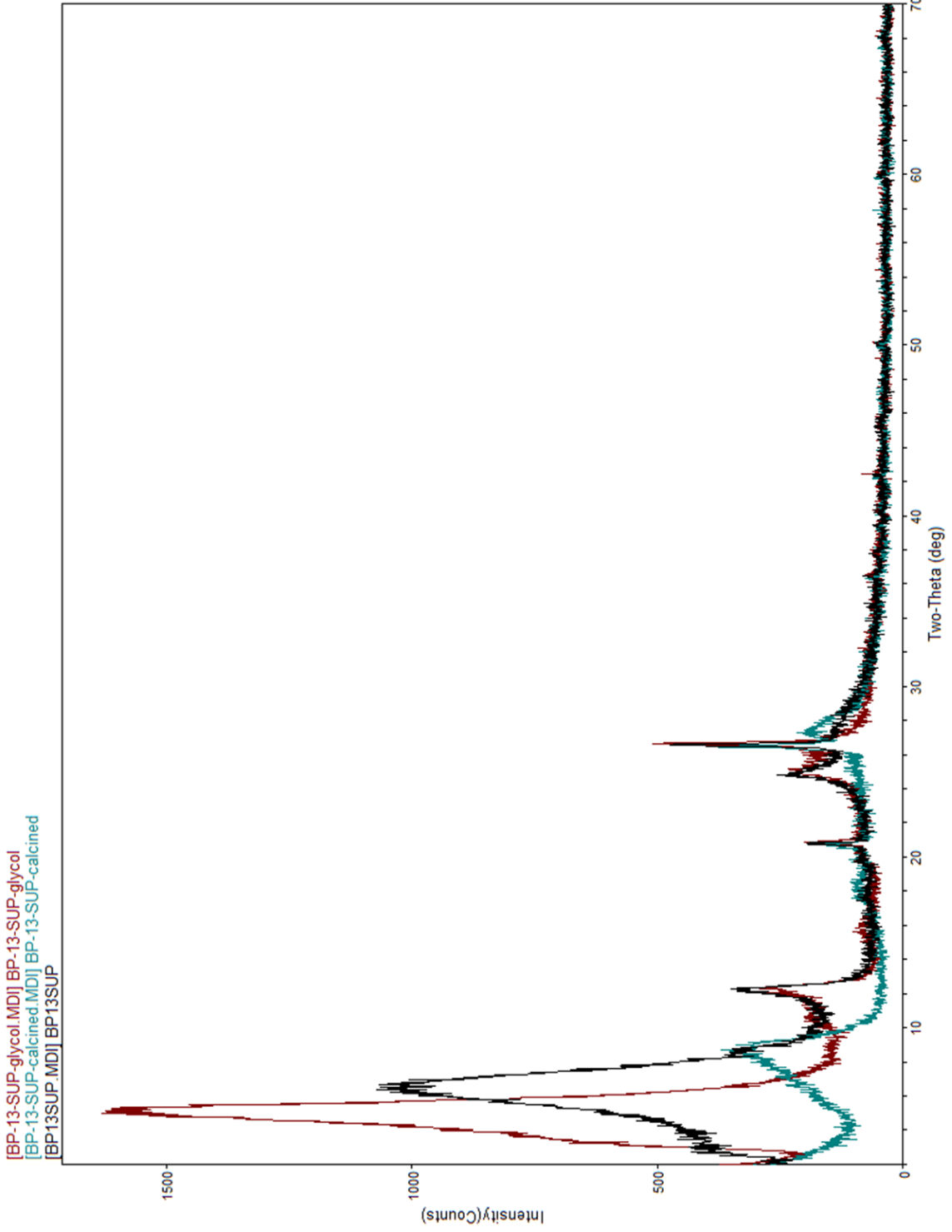
[BP-13-INF-glycol.MDI] BP-13-INF-glycol  
[BP-13-INF-caicined.MDI] BP-13-INF-caicined  
[BP-13-INF.MDI] BP-13-INF





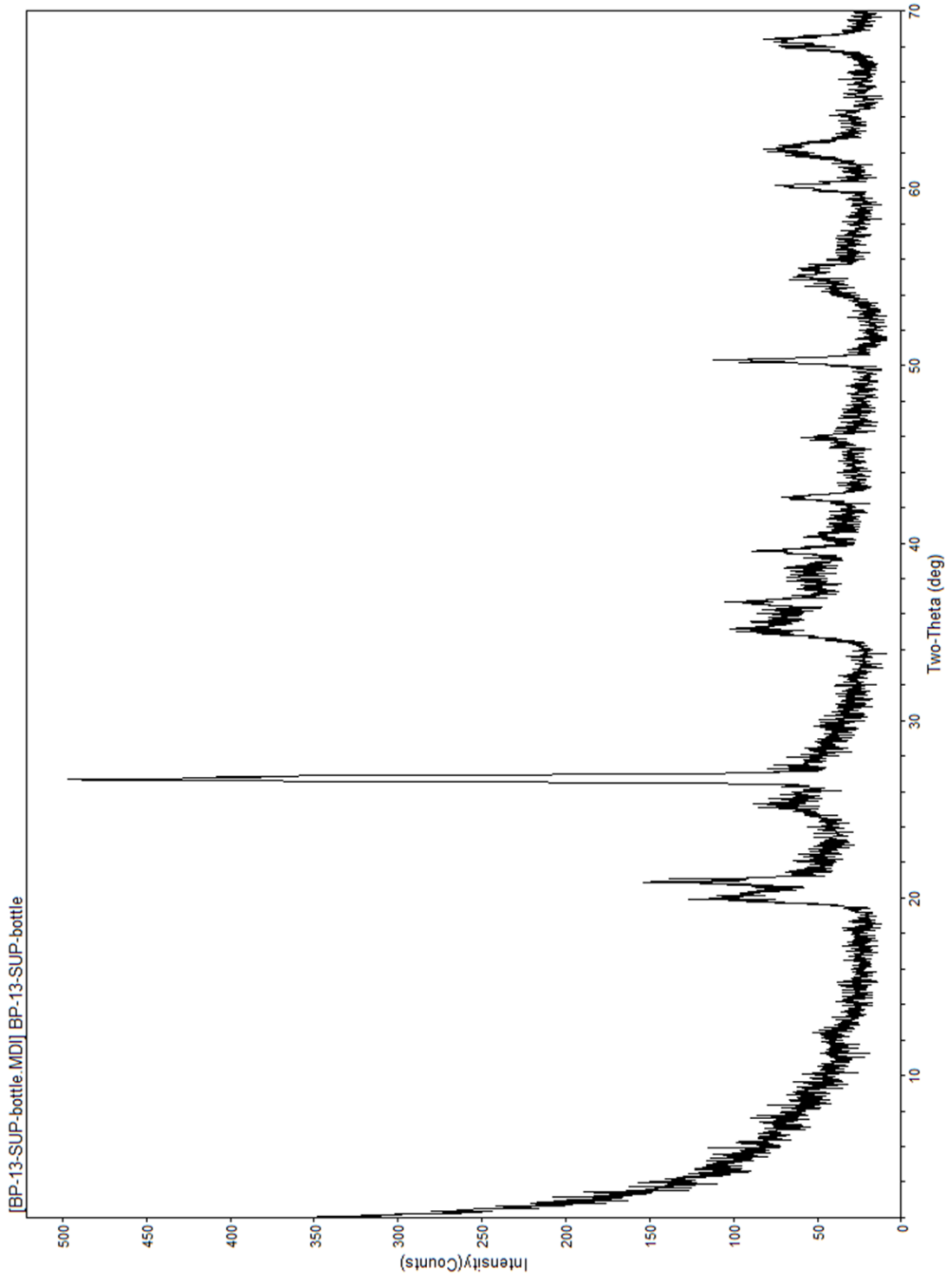
[MRLW07113200]eect159]c:\MARIASOL\_XRD> Wednesday, March 16, 2011 02:26p (MDI/JADE9)

Penn State



[MRLW07113200]eect159]c:\MARIASOL\_XRD> Wednesday, March 16, 2011 03:46p (MDI/JADE9)

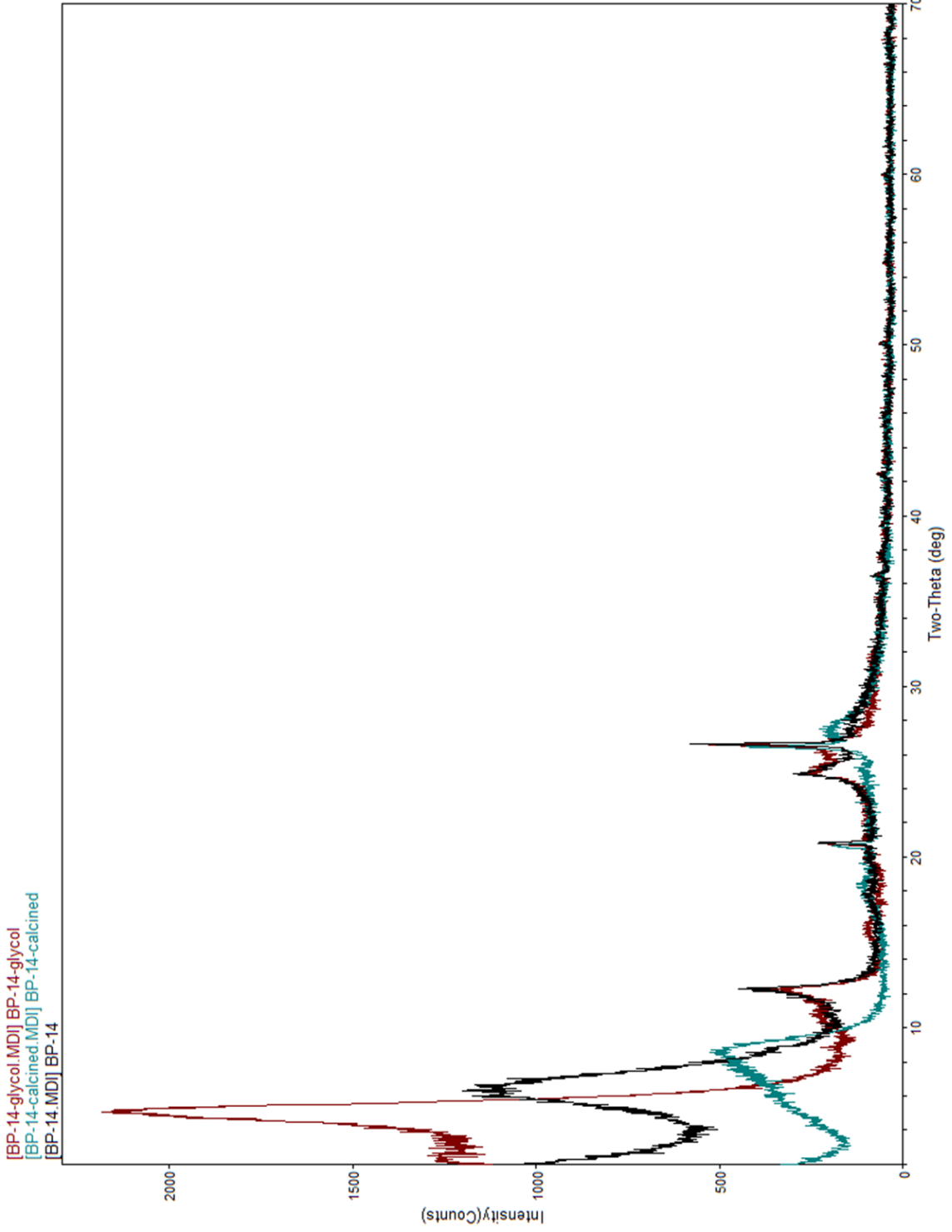
Penn State



[MRLW07113200]eect159]c:\MARIASOL\_XRD> Wednesday, March 16, 2011 03:49p (MDI/JADE9)

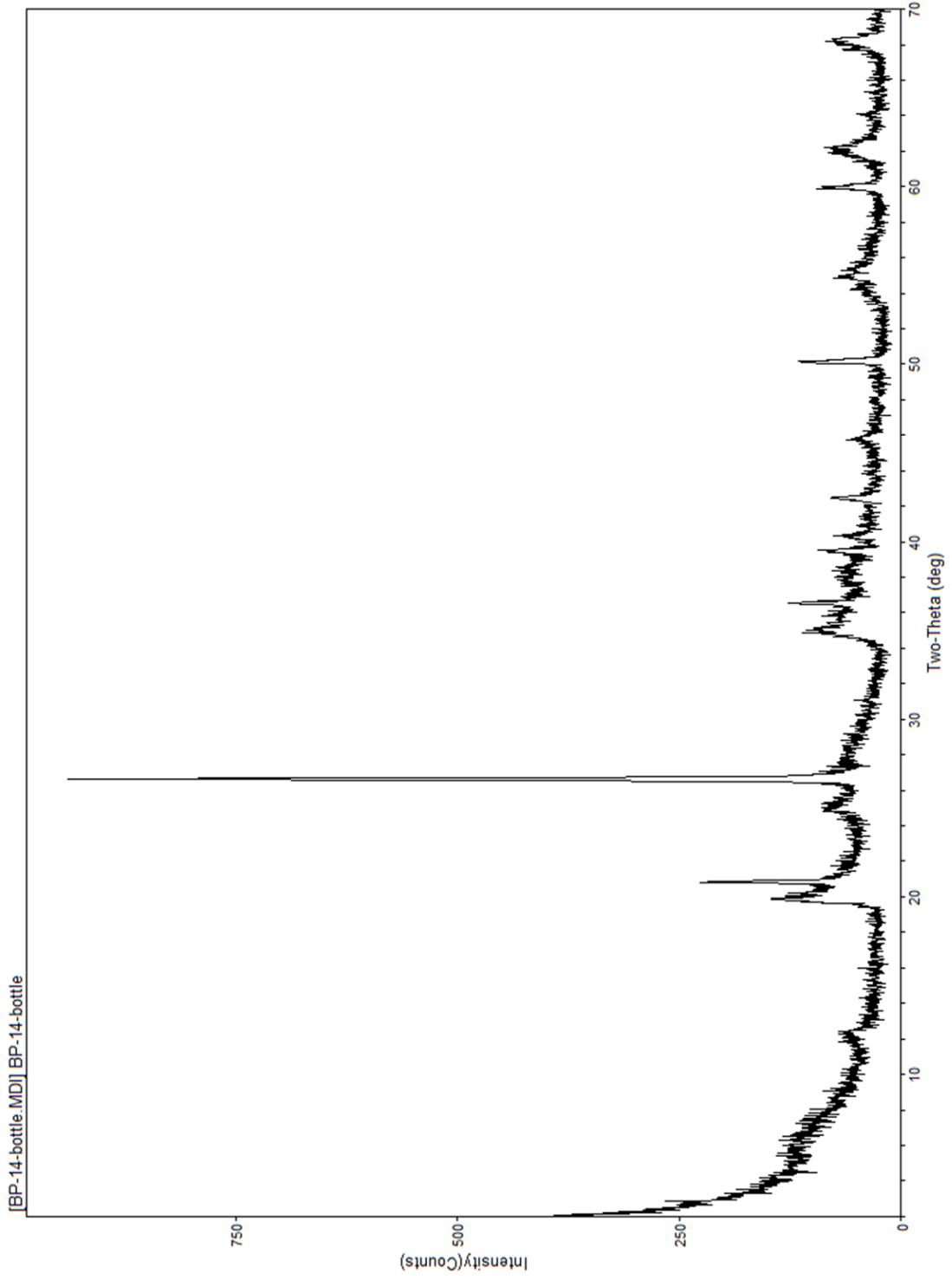
Penn State





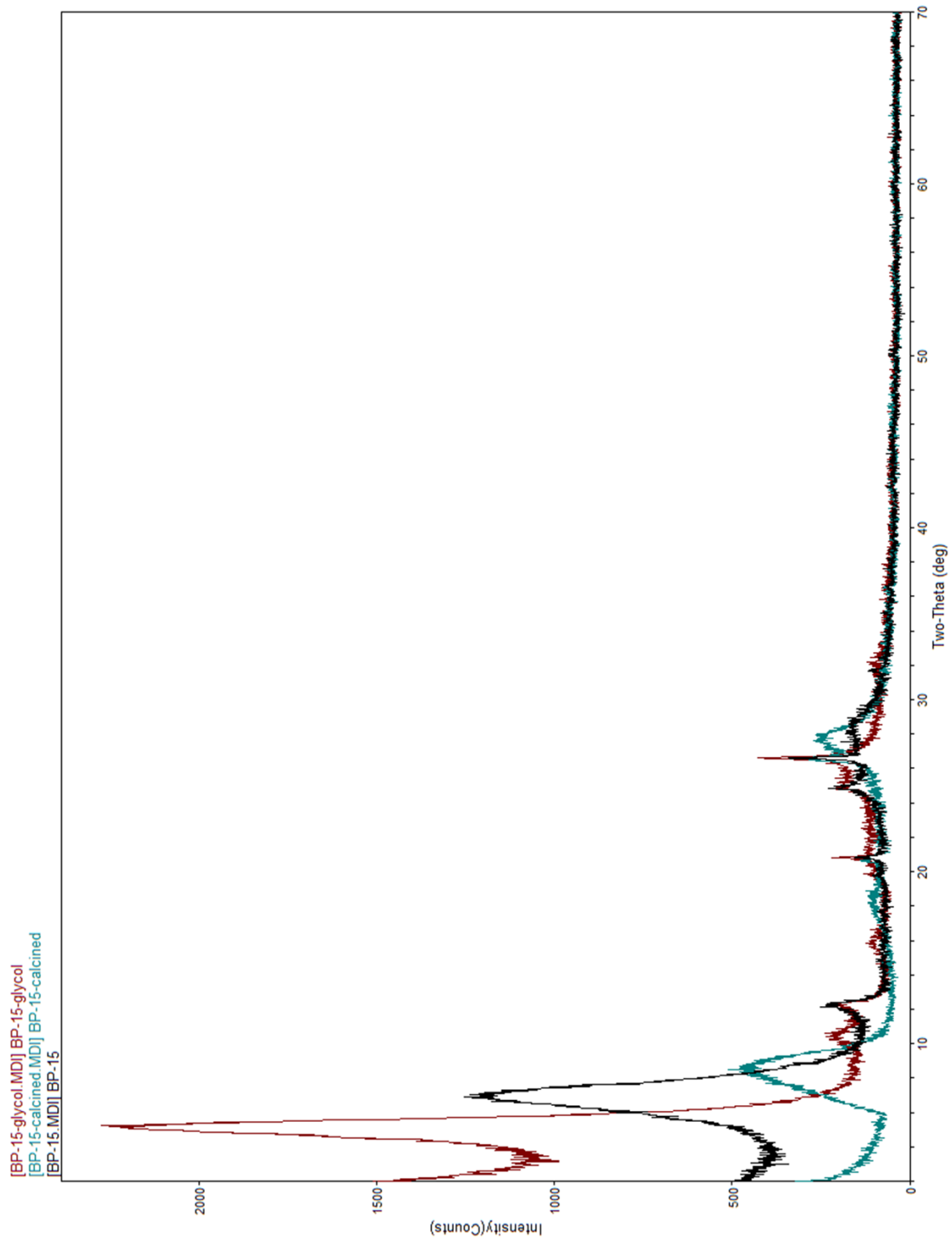
[MRLW07113200]eect159]c:\MARIASOL\_XRD> Wednesday, March 23, 2011 11:56a (MDI/JADE9)

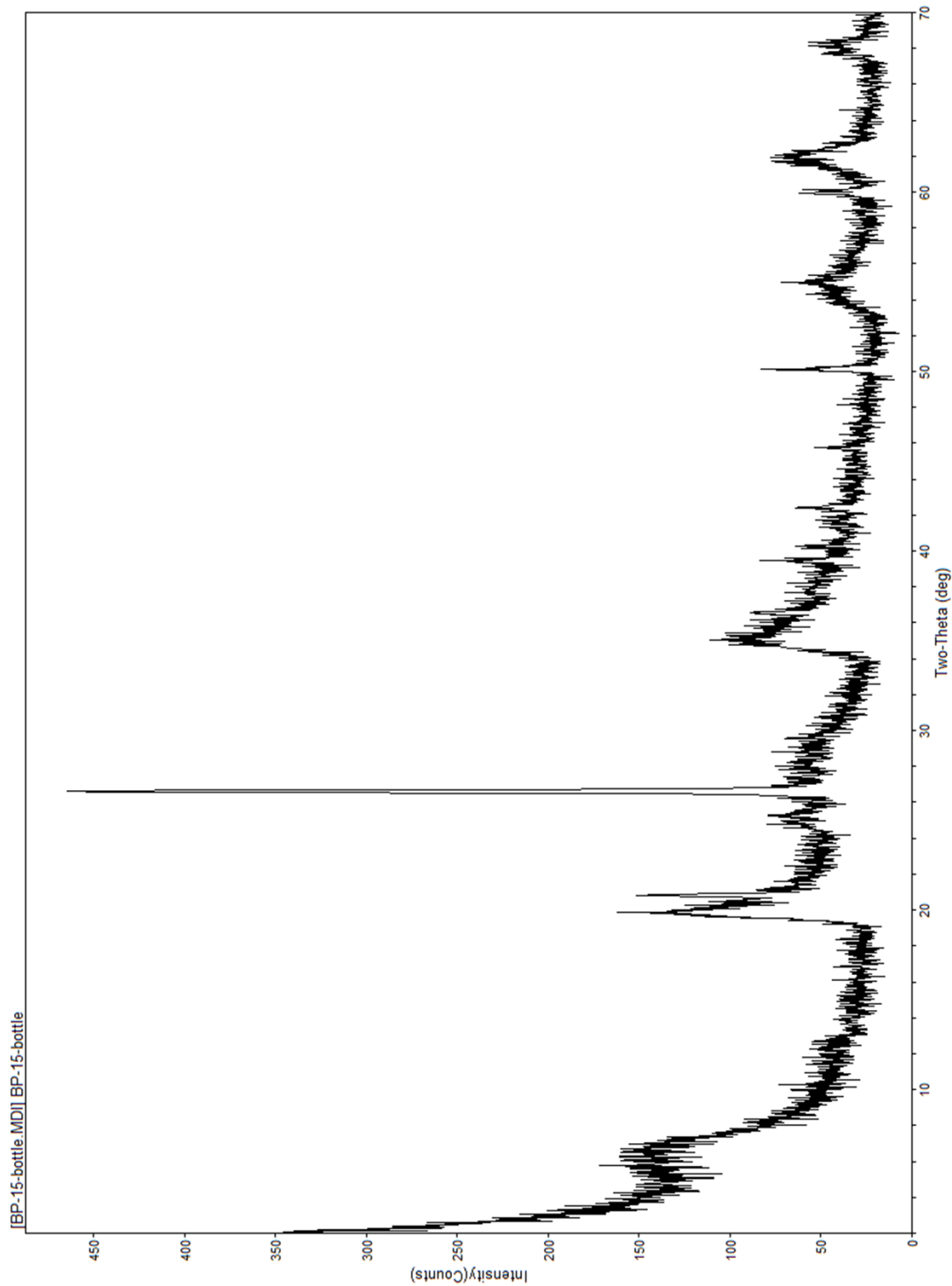
Penn State

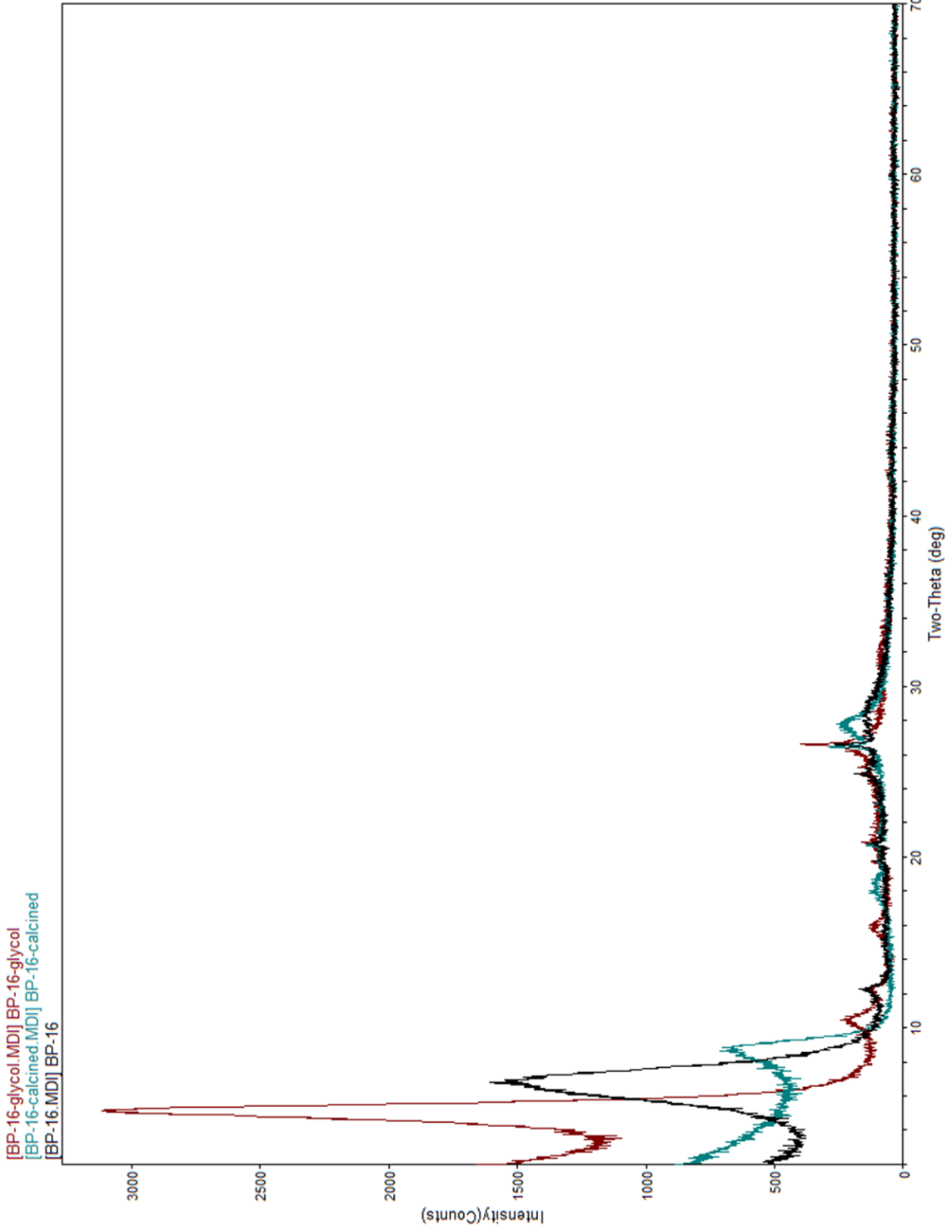


[MRLW07113200[eeec159]sc:MARIA SOL\_XRD> Wednesday, March 23, 2011 11:57a (MDI/JADE9)

Penn State

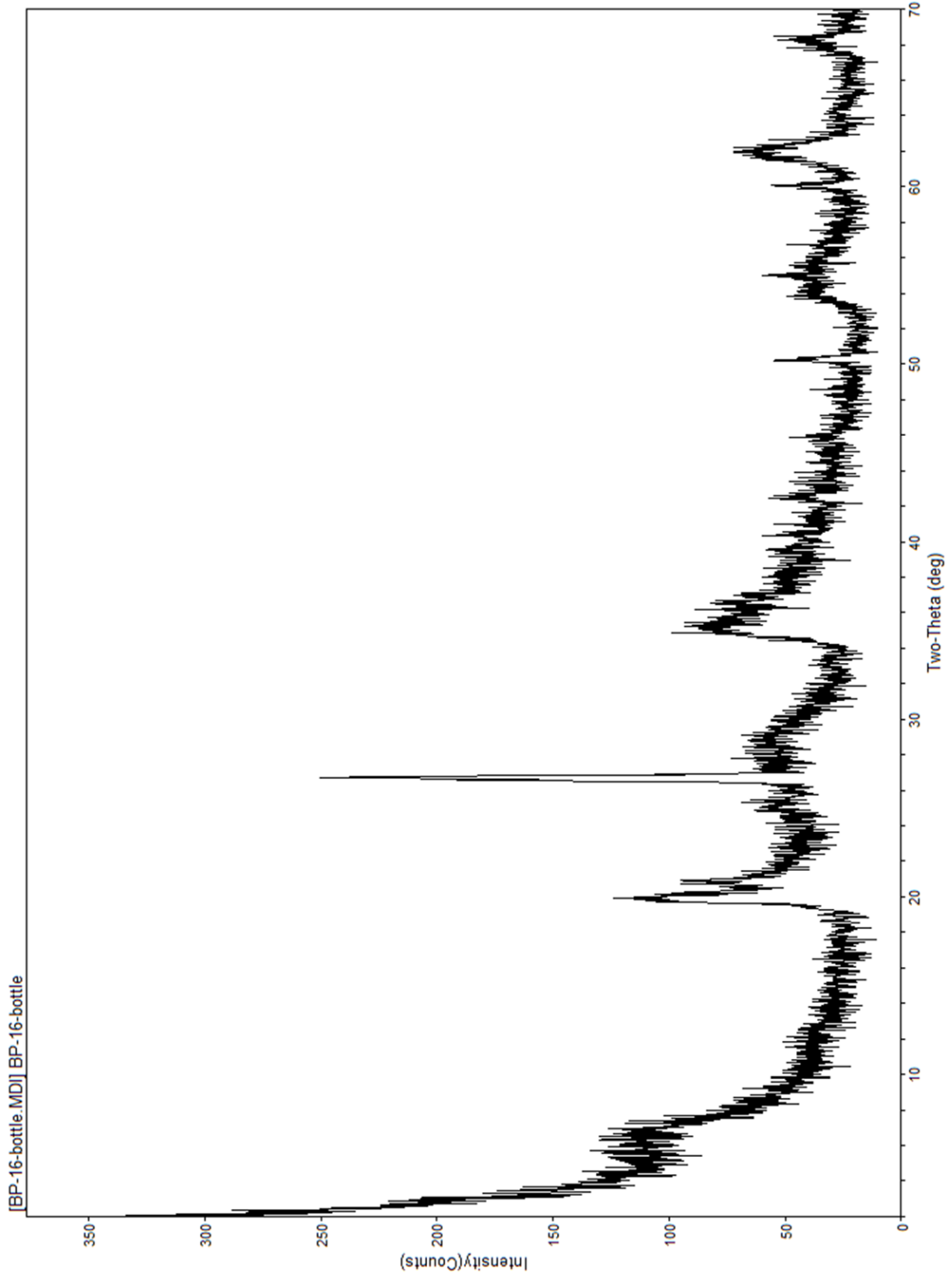






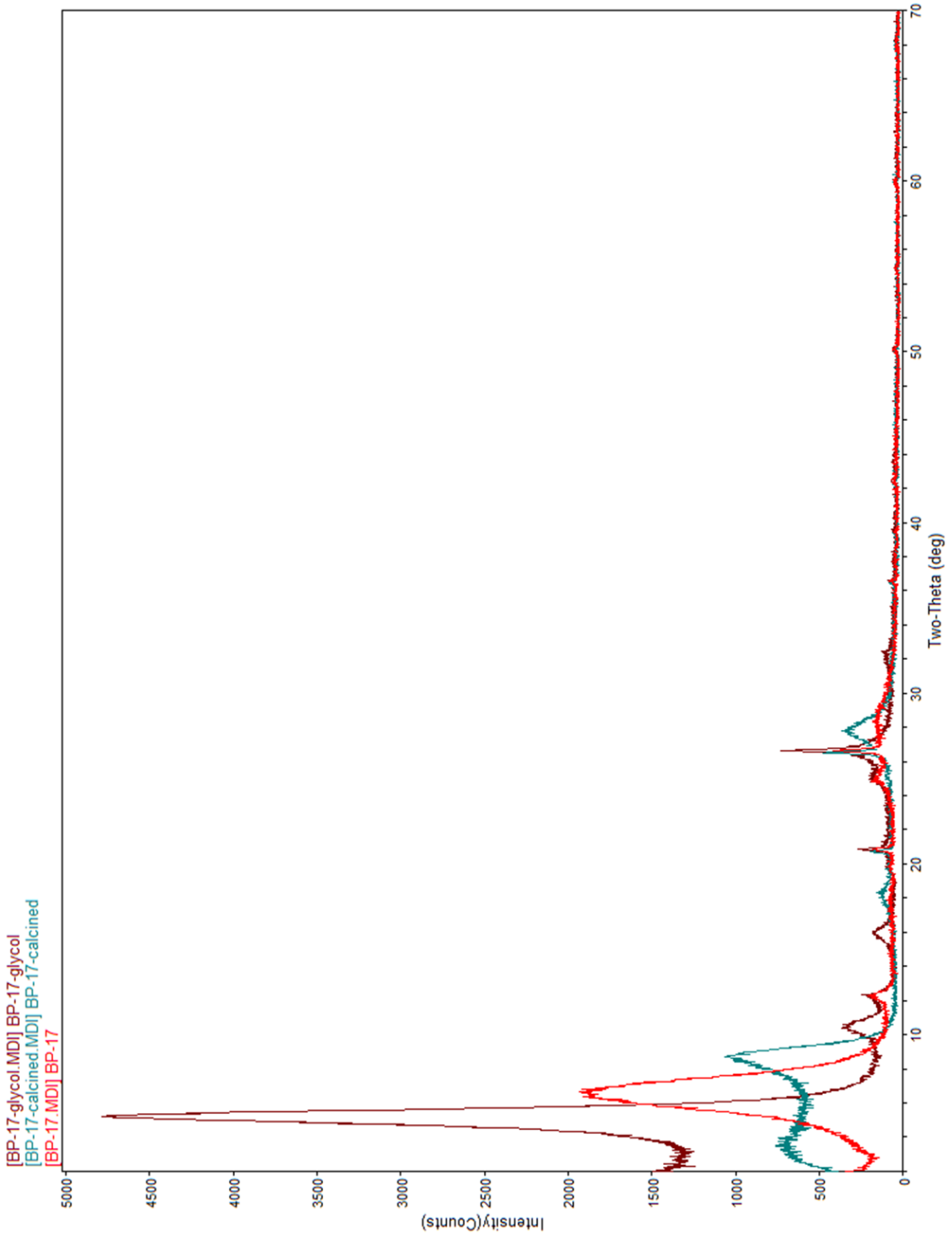
[MRLW07113200]eect159]c:\MARIASOL\_XRD> Wednesday, March 16, 2011 04:55p (MDI/JADE9)

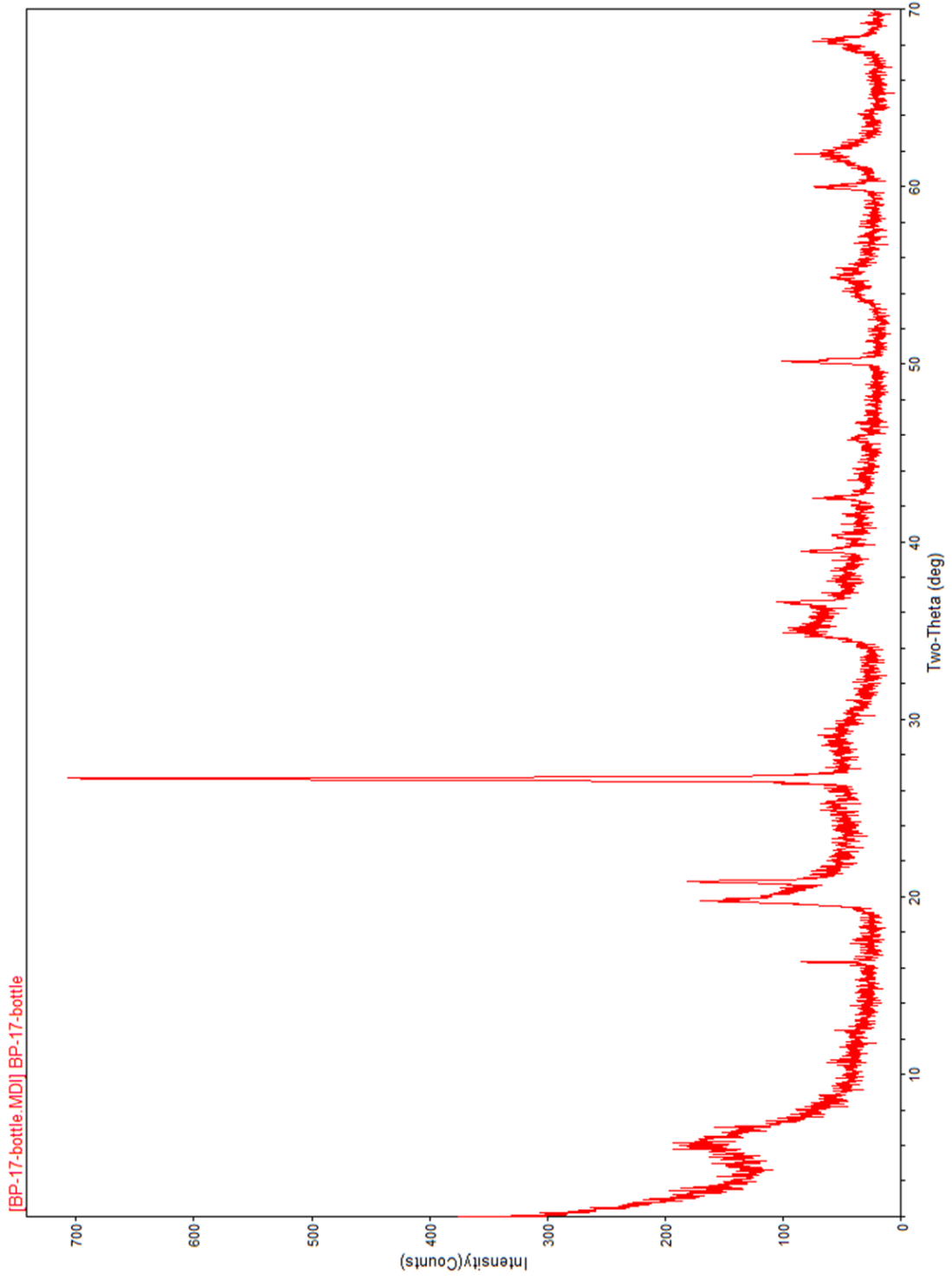
Penn State



[MRLW07113200]eect159]c:\MARIASOL\_XRD> Wednesday, March 16, 2011 04:56p (MDI/JADE9)

Penn State



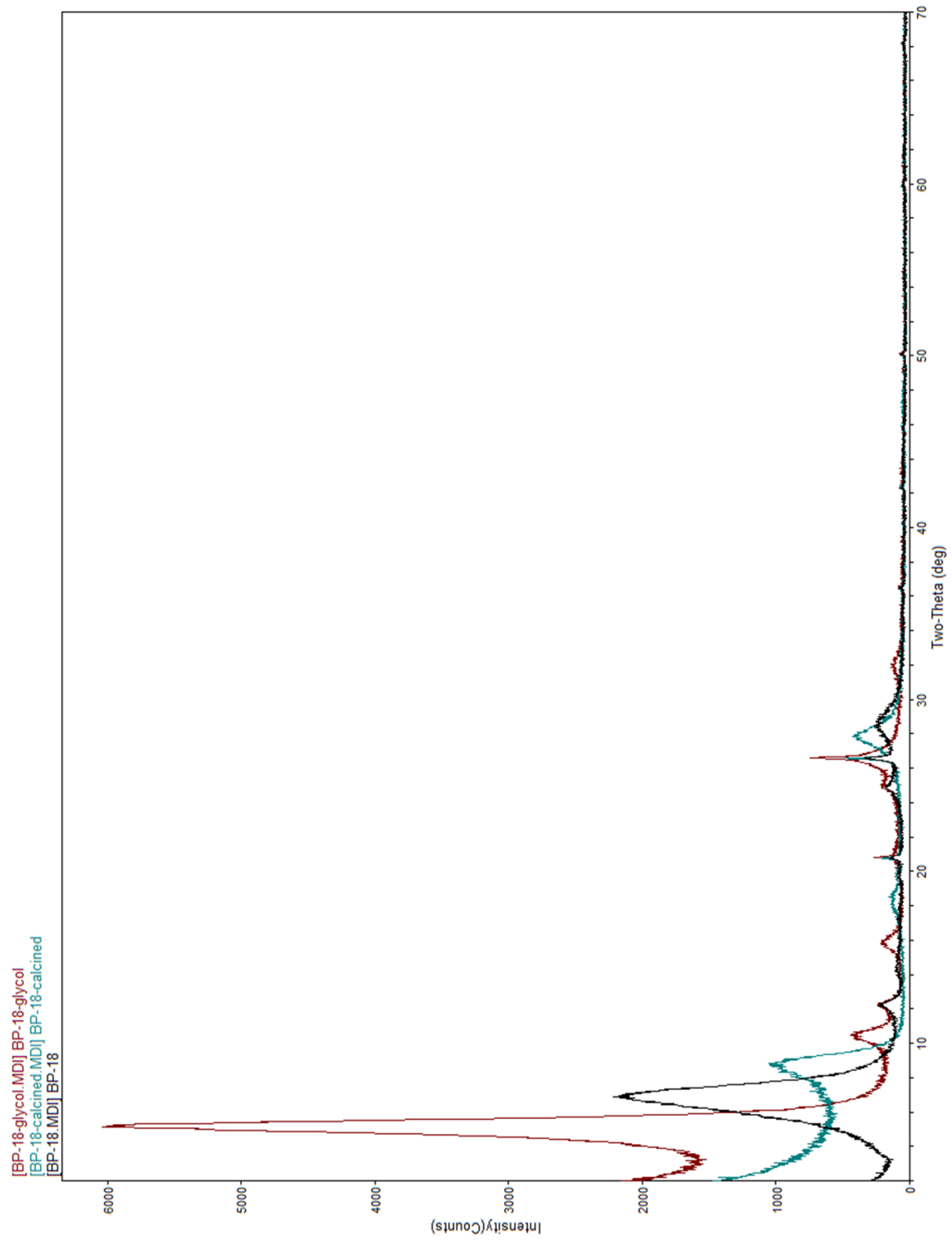


[BP-17-bottle.MDI] BP-17-bottle

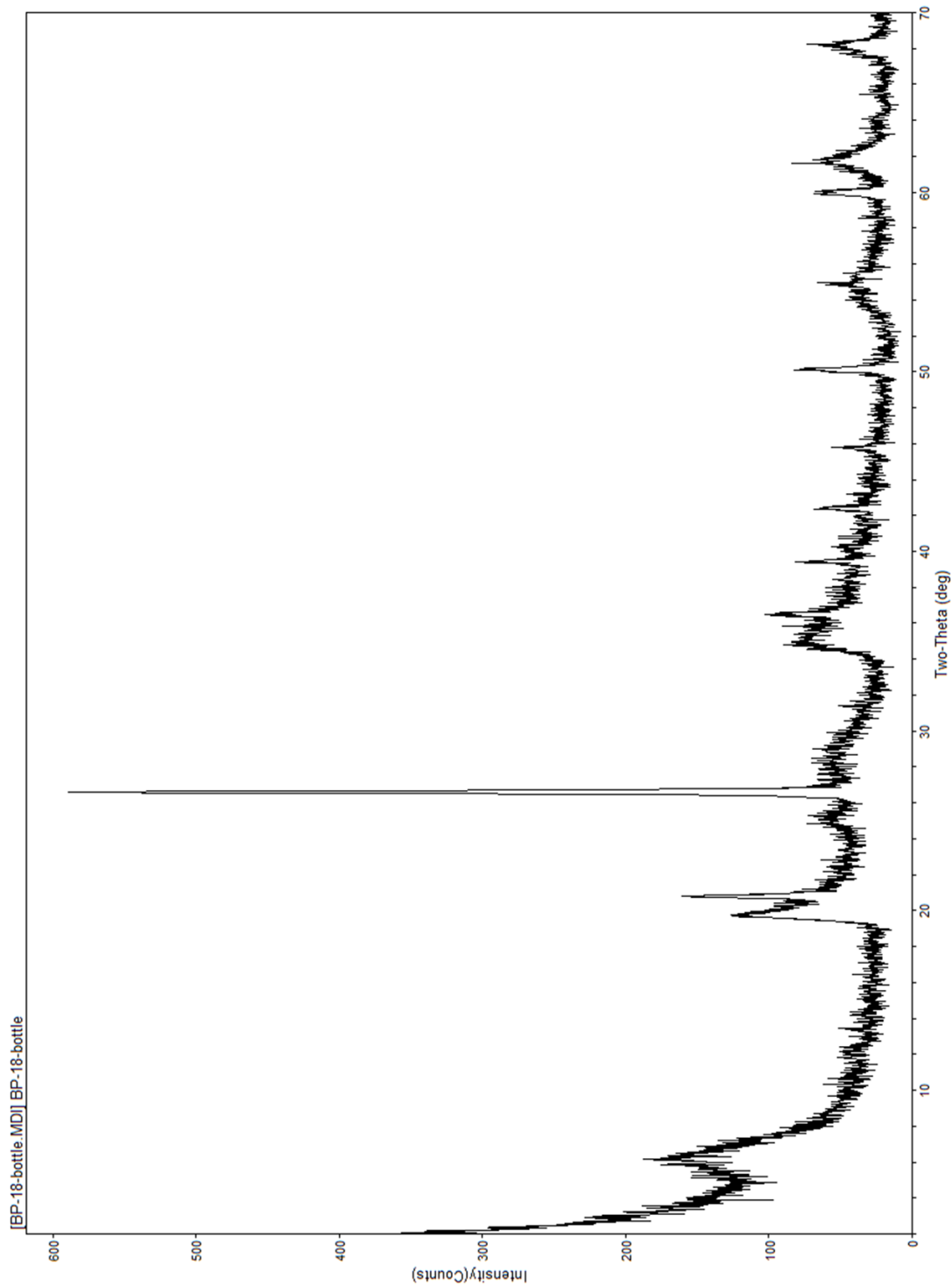
[MRLW07113200.eec159]c:\MARIASOL\_XRD> Wednesday, March 23, 2011 09:17a (MDI/JADE9)

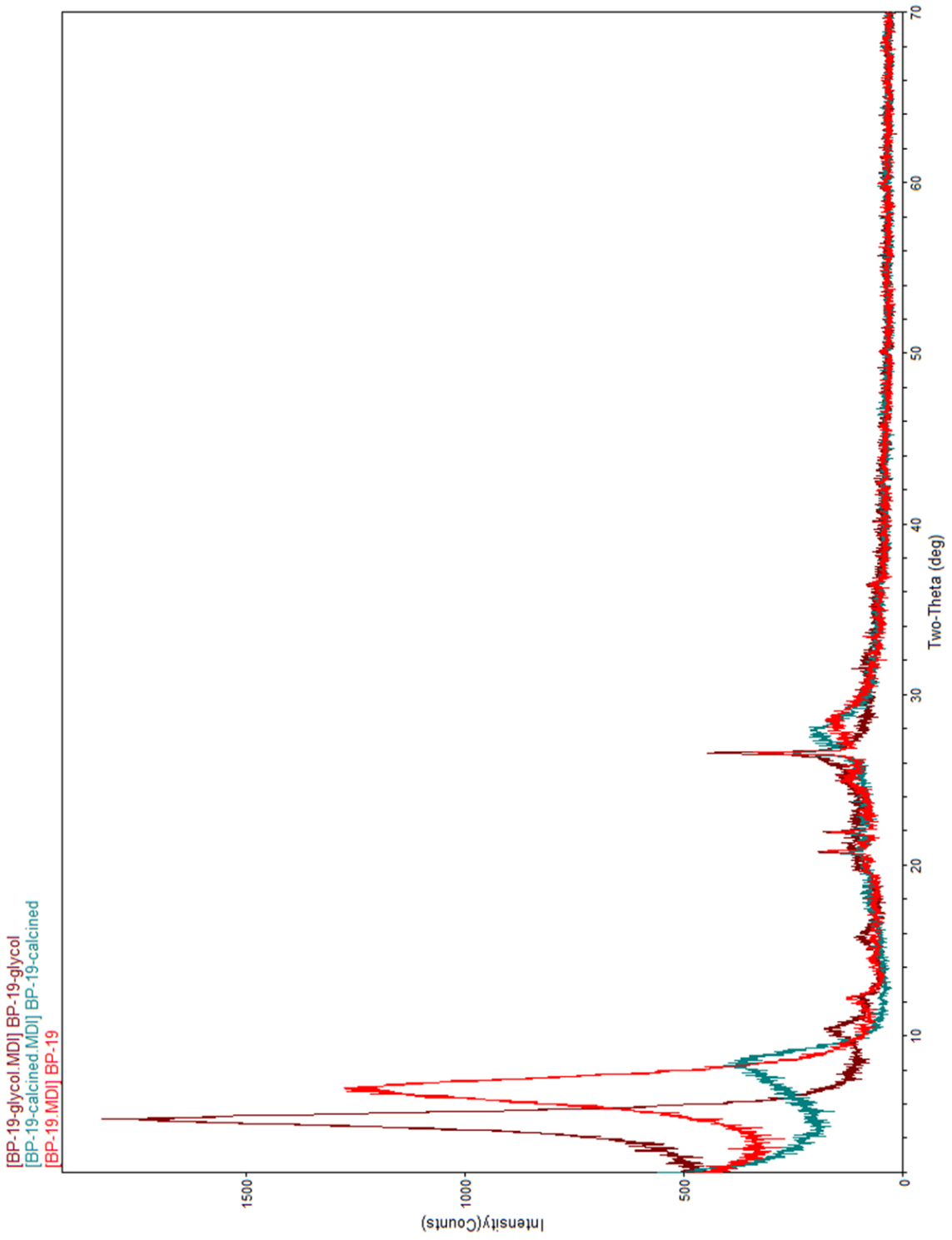
Penn State





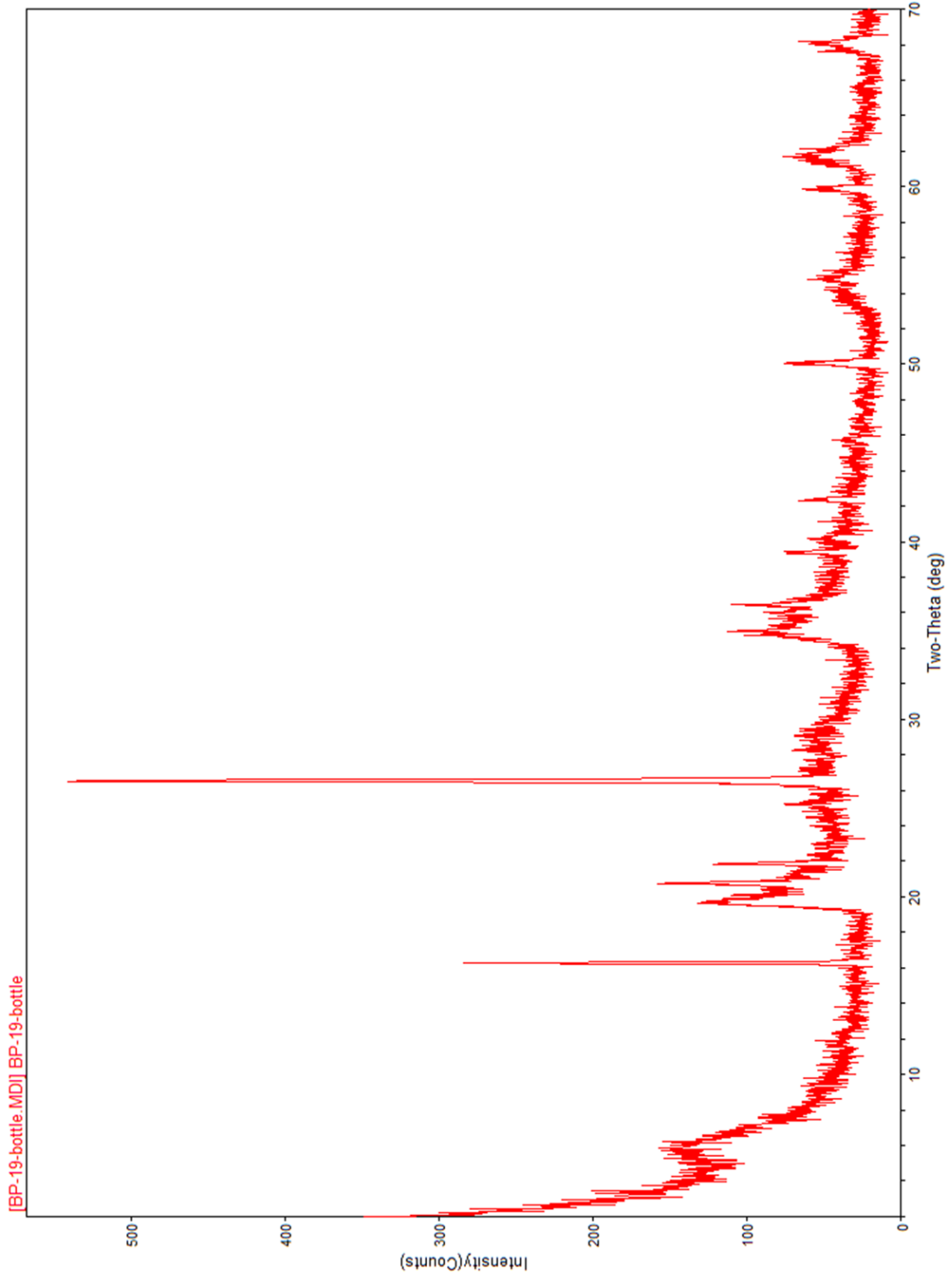
[BP-18-glycol.MDI] BP-18-glycol  
[BP-18-calcined.MDI] BP-18-calcined  
[BP-18.MDI] BP-18





[MRLW07113200]eect159]c:\MARIASOL\_XRD> Wednesday, March 23, 2011 09:33a (MDI/JADE9)

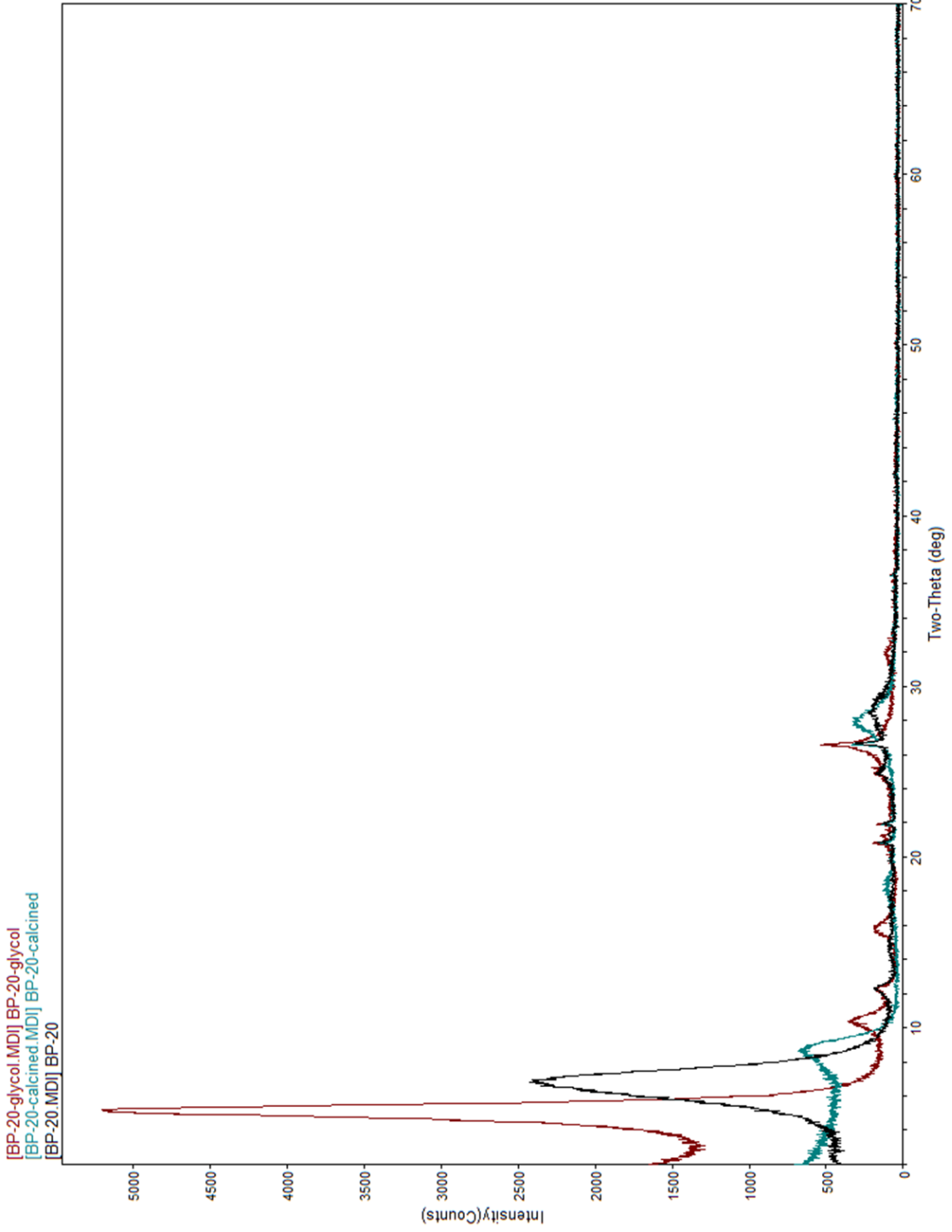
Penn State



[BP-19-bottle.MDI] BP-19-bottle

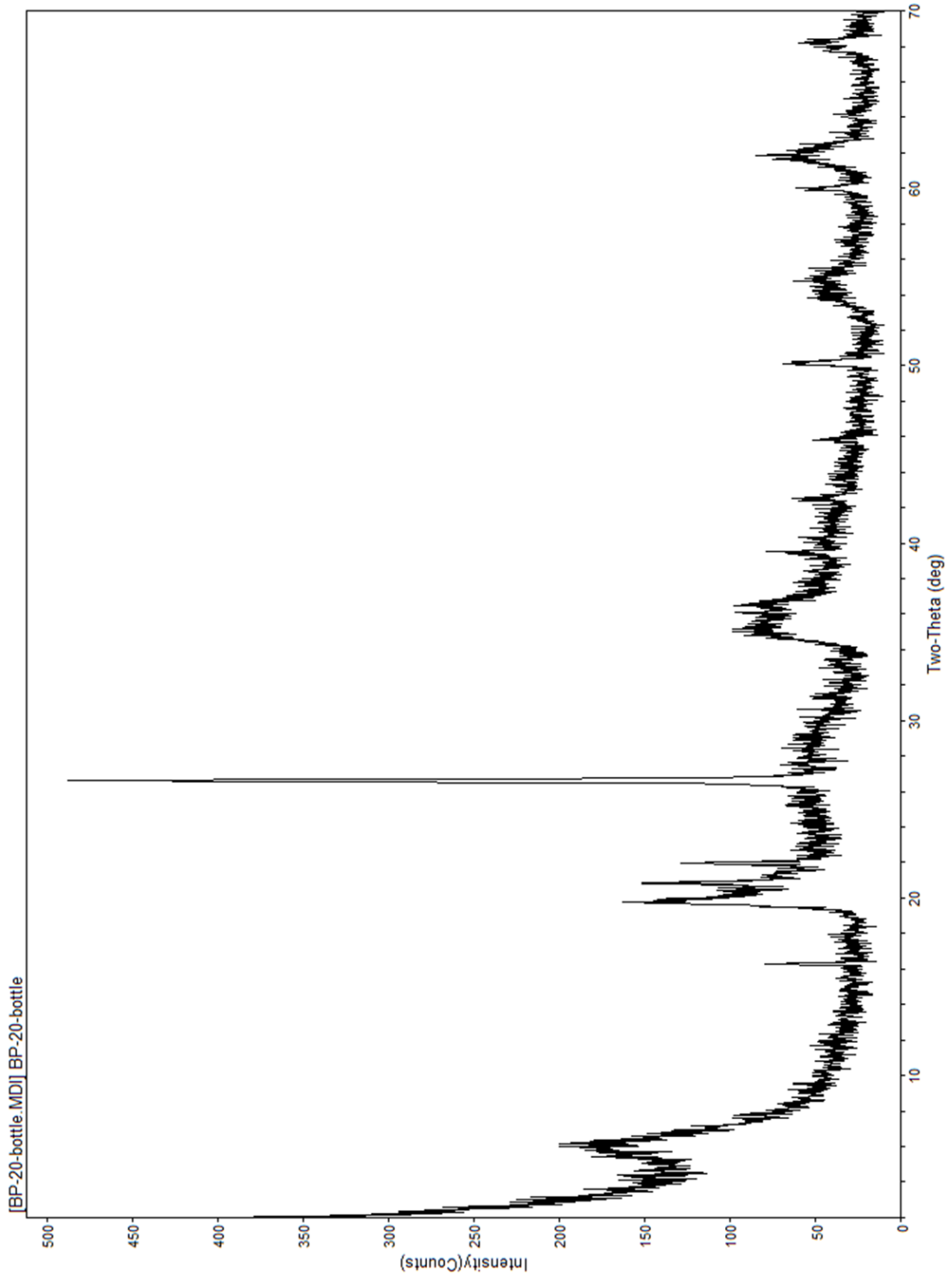
[MRLW07113200]ec159]c:\MARIASOL\_XRD> Wednesday, March 23, 2011 09:35a (MDI/JADE9)

Penn State



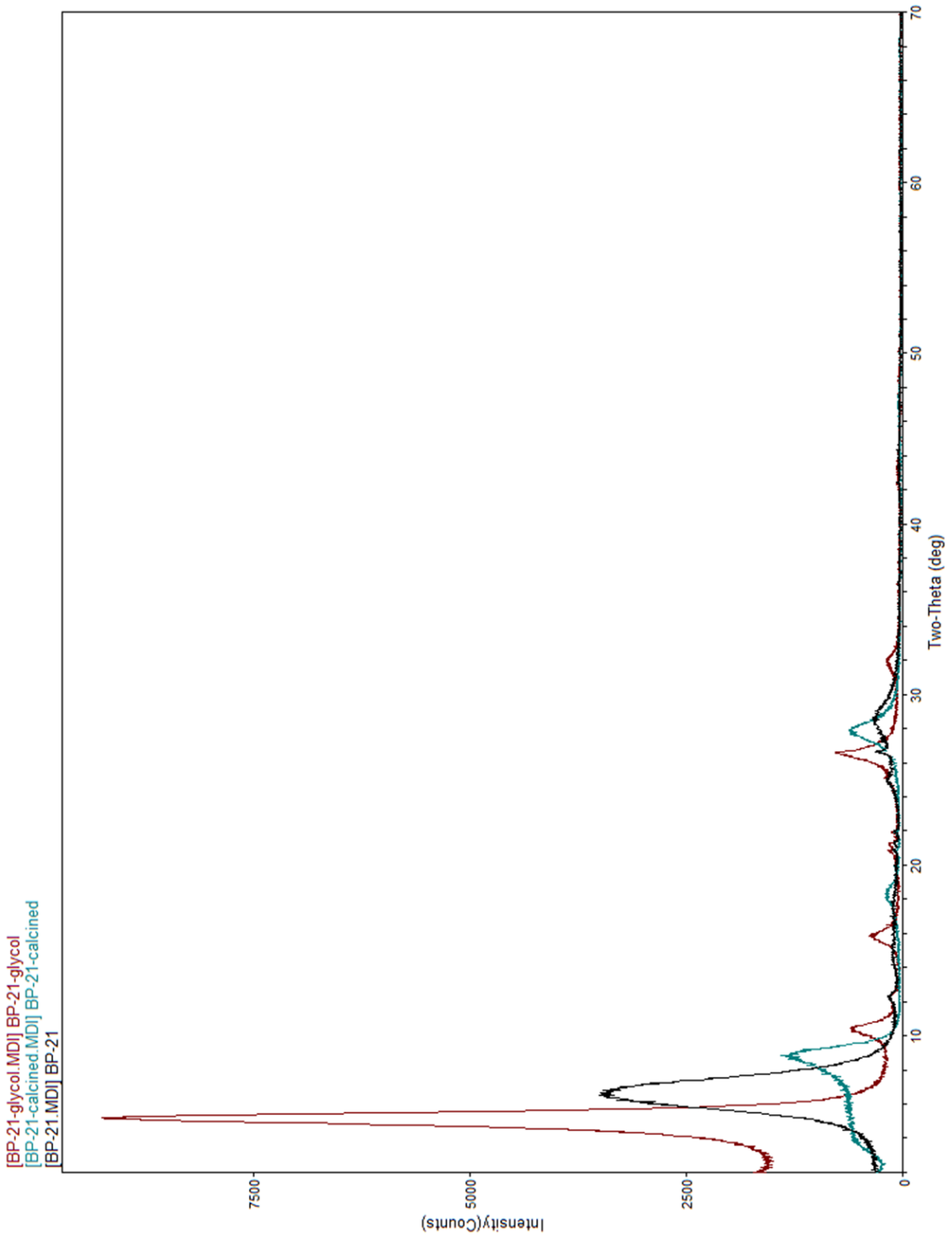
[MRLW07113200]ec158]sc:IMARIASOL\_XRD> Wednesday, March 23, 2011 10:44a (MDI/JADE9)

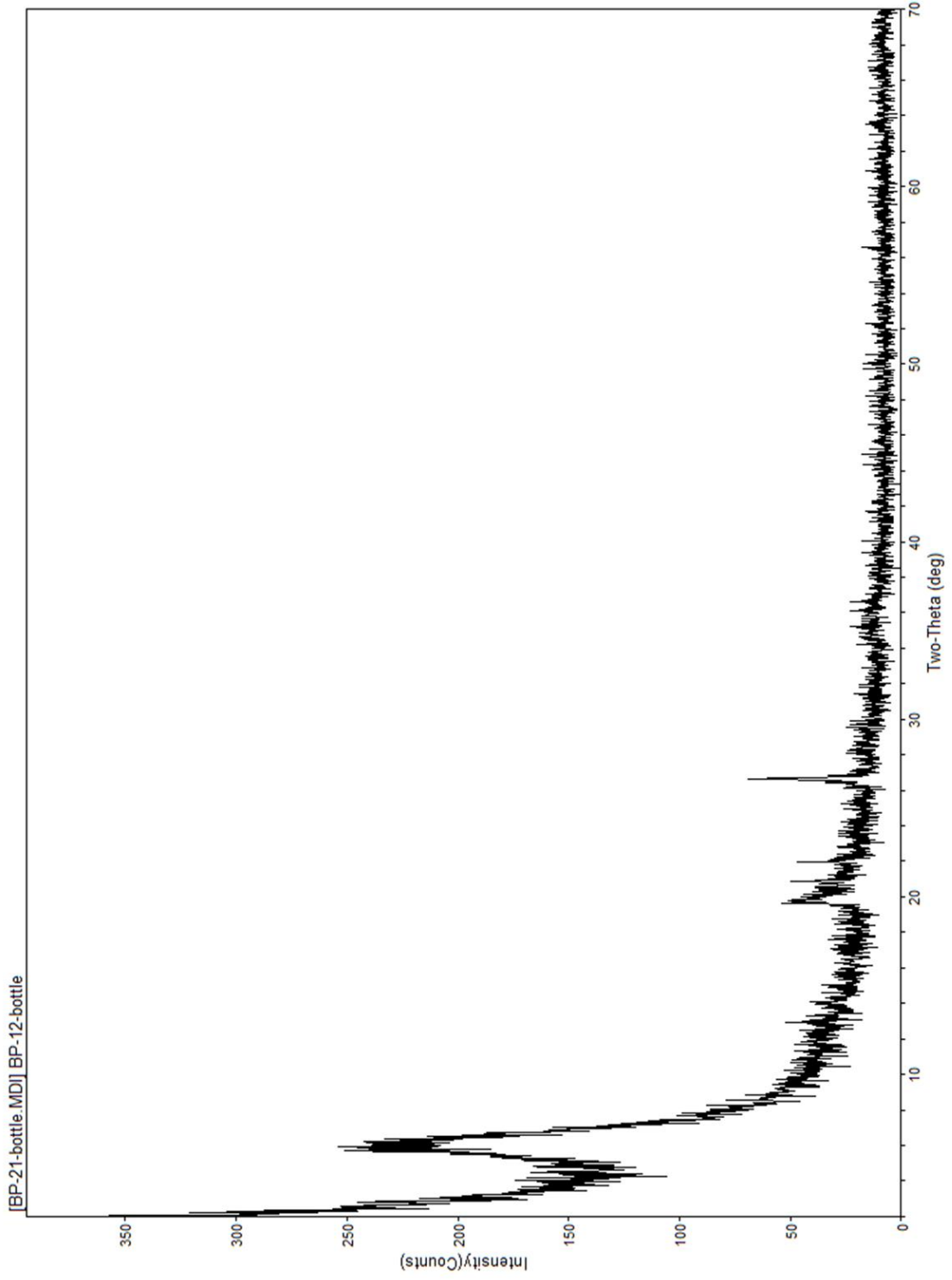
Penn State



[MRLW07113200[eeec159]sc:MIARIASOL\_XRD> Wednesday, March 23, 2011 10:24s (MDI/JADE9)

Penn State



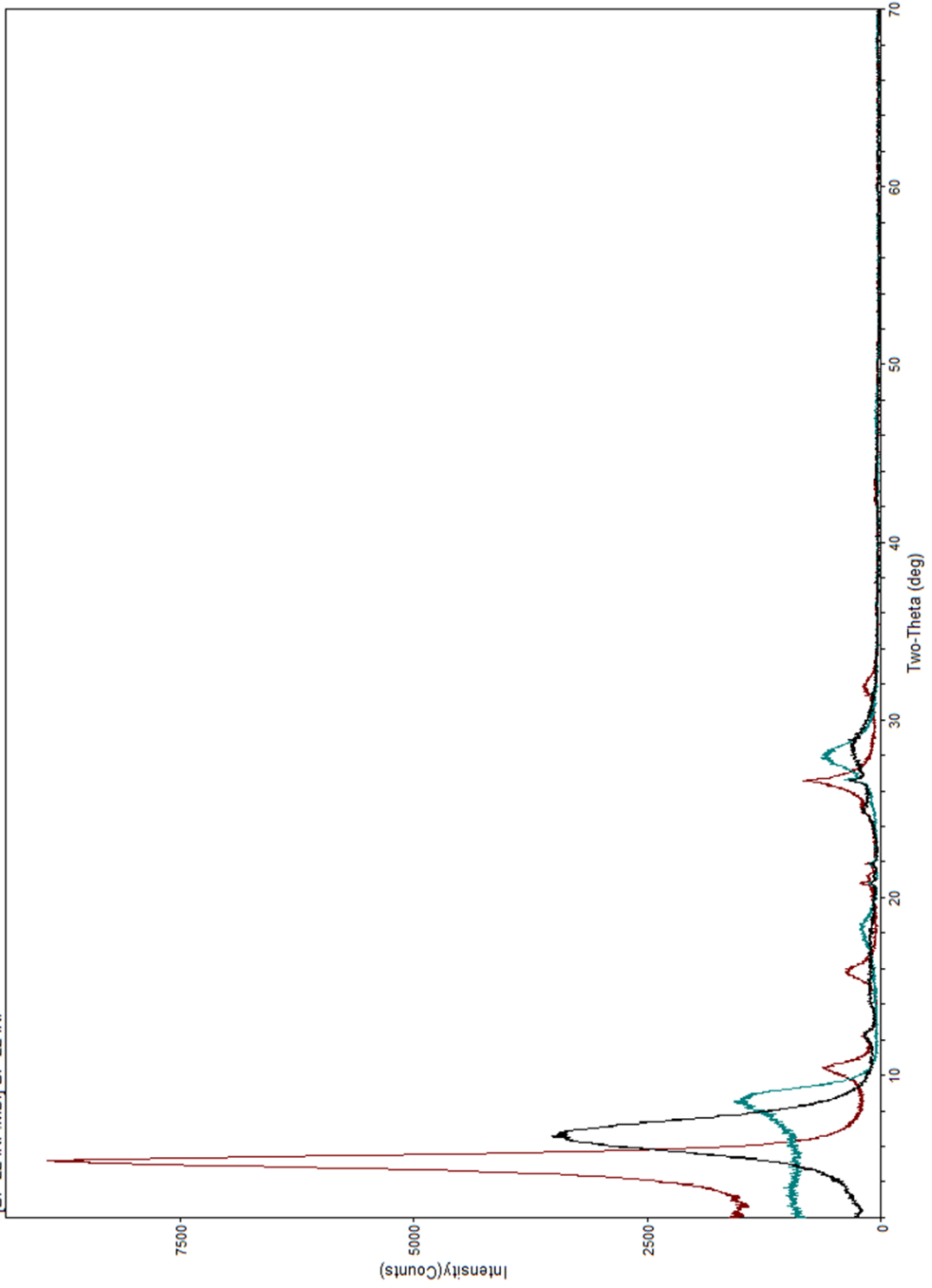


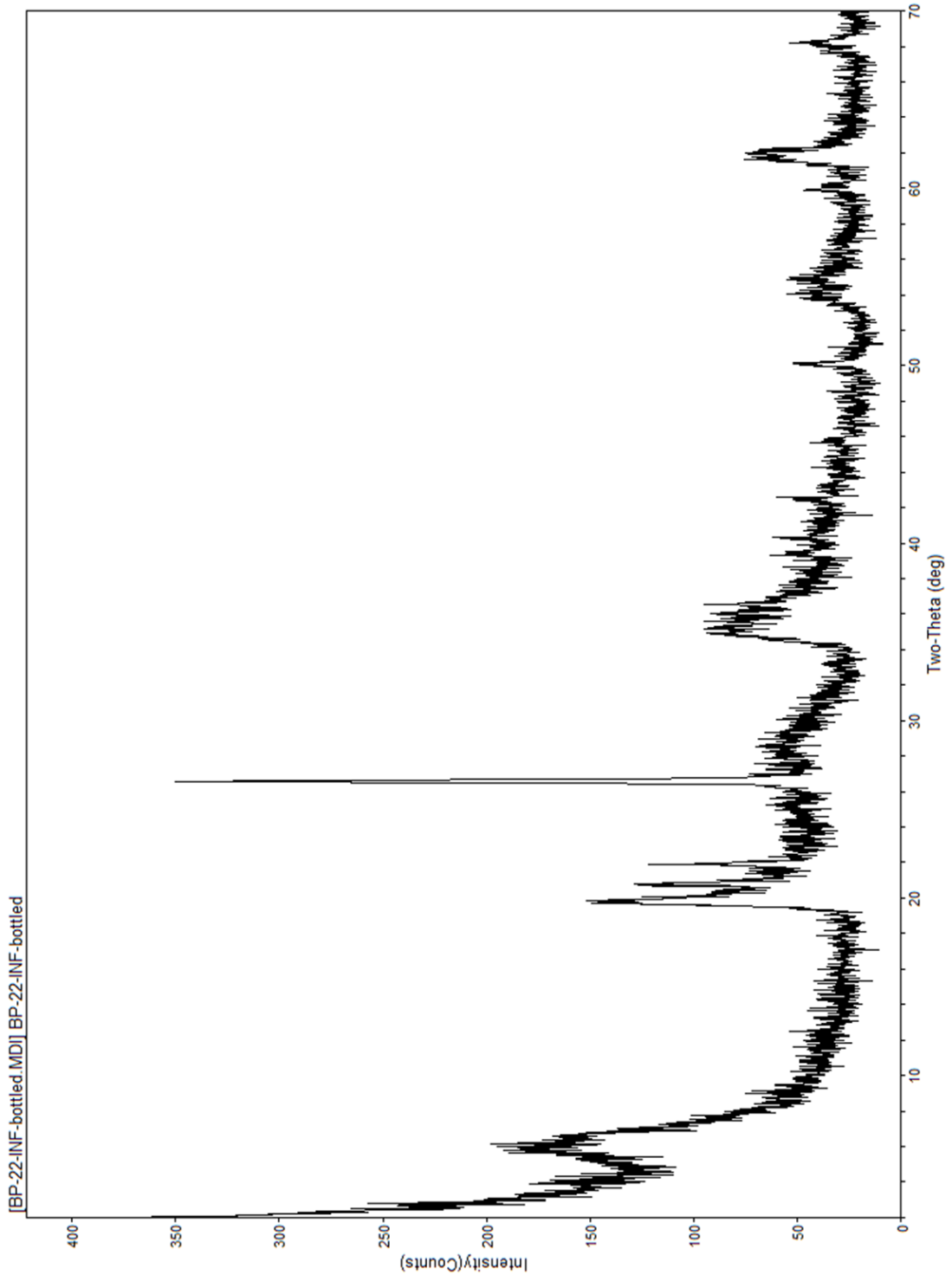
[MRLW07113200[eeet159]sc\MARIASOL\_XRD> Wednesday, March 16, 2011 04:16p (MDI/JADE9)

Penn State



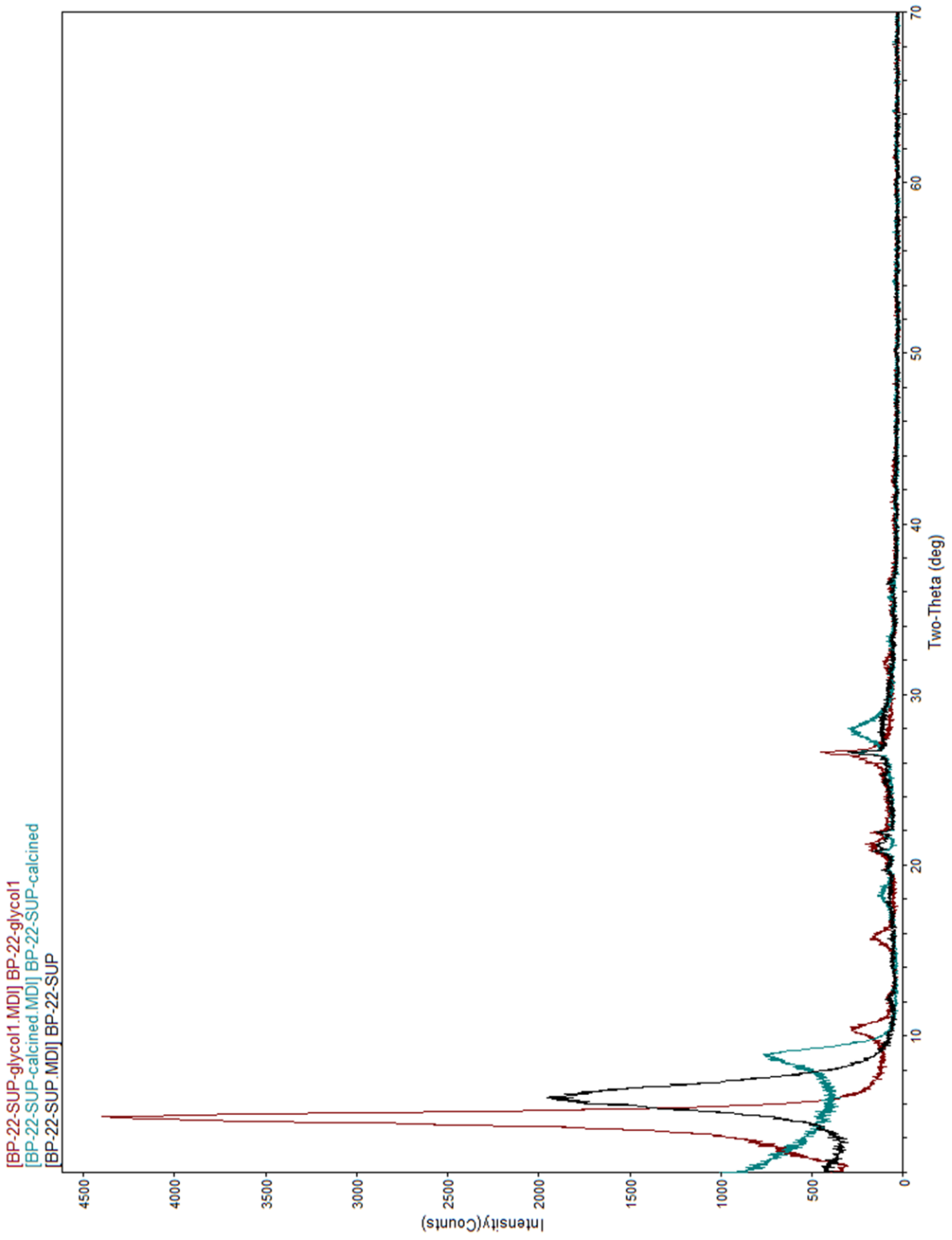
[BP-22-INF-glycol.MDI] BP-22-INF-glycol  
[BP-22-INF-caicined.MDI] BP-22-INF-caicined  
[BP-22-INF.MDI] BP-22-INF





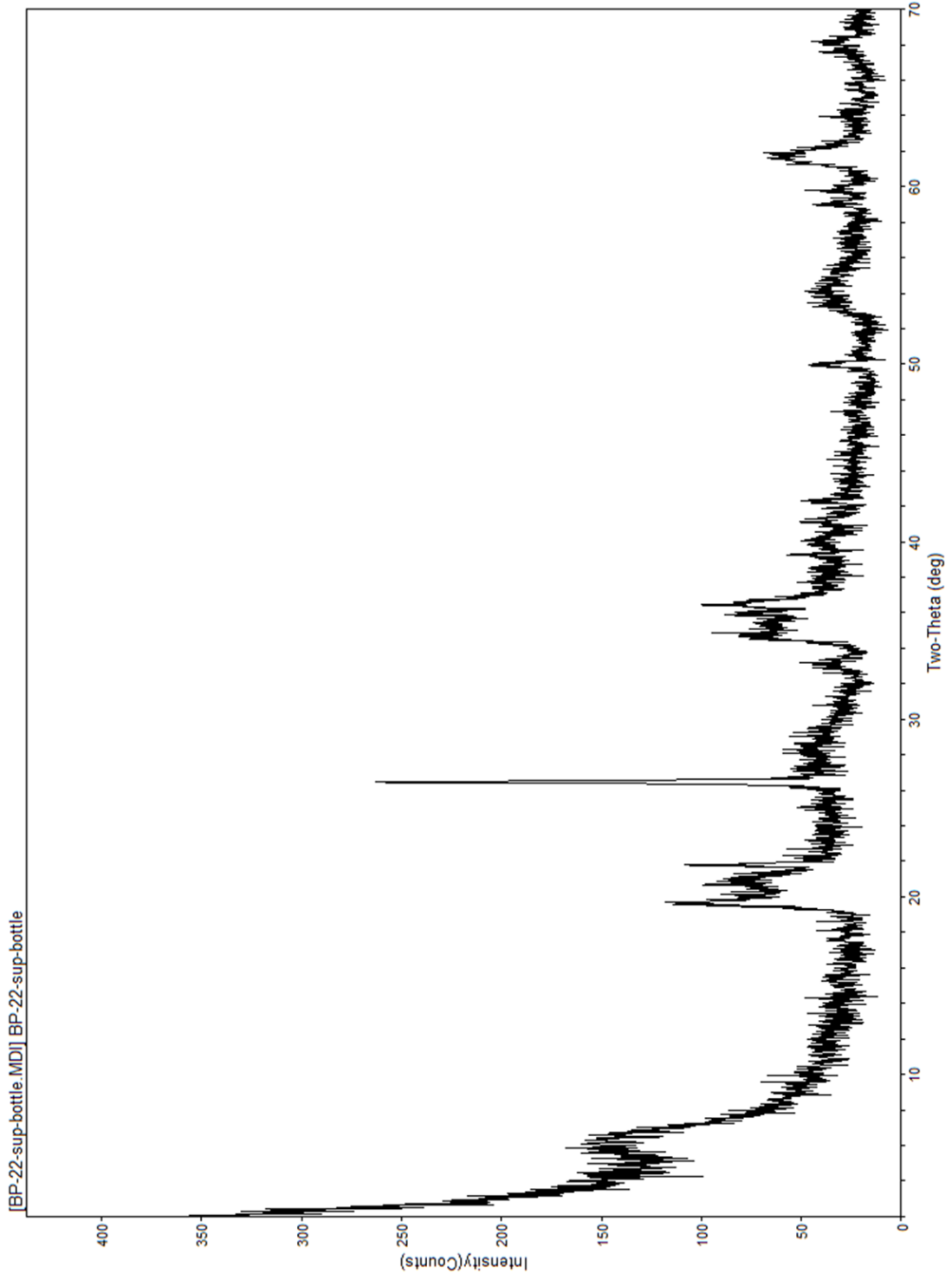
[MRLW07113200]eect159]c:\MARIASOL\_XRD> Wednesday, March 23, 2011 12:39p (MDI/JADE9)

Penn State



[MRLW07113200]eect158]c:\MARIASOL\_XRD> Wednesday, March 16, 2011 04:26p (MDI/JADE9)

Penn State



[MRLW07113200[eeet159]sc:MARIA SOL\_XRD> Wednesday, March 16, 2011 04:28p (MDI/JADE9)

Penn State

From:	Henry Gong, 312 Hosler Building														
To:	Emily Comer														
Date	4/21/11														
Basis	As-Received														
Instrument	Perkin-Elmer Optima 5300, Inductively Coupled Plasma Emission Spectrometry (ICP-AES)														
Dissolution	lithium metaborate														
Subject	Spectrochemical Characterization of solids														
Units	weight percent														
Det. Limit	0.02	0.01	0.02	0.02	0.02	0.02	0.01	0.02	0.01	0.05	0.02	0.01	0.01	0.01	0.01
Our #	Your #	Al <sub>2</sub> O <sub>3</sub> (%)	BaO (%)	CaO (%)	Fe <sub>2</sub> O <sub>3</sub> T (%)	K <sub>2</sub> O (%)	MgO (%)	MnO (%)	Na <sub>2</sub> O (%)	P <sub>2</sub> O <sub>5</sub> (%)	SiO <sub>2</sub> (%)	SrO (%)	TiO <sub>2</sub> (%)	LOI (900C)	Total
11-0577	1	13.2	0.04	0.56	2.51	1.49	0.54	0.04	0.68	0.06	69.3	0.01	0.85	6.88	96.2
11-0578	6	21.3	0.01	1.41	5.78	0.49	0.76	0.00	1.20	0.06	52.6	0.02	0.79	16.3	100.7
11-0579	10	20.7	0.02	1.23	4.69	0.64	0.82	0.04	0.70	0.04	56.6	0.02	0.93	14.3	100.7
11-0580	11	17.2	0.01	1.53	7.72	0.31	0.98	0.02	0.66	0.05	56.5	0.02	0.95	15.1	101.0
11-0581	13	16.2	0.04	0.14	3.27	1.35	0.82	0.04	1.42	0.06	64.0	0.01	0.91	10.0	98.2
11-0582	20	16.5	0.01	1.43	9.26	0.19	1.19	0.01	0.55	0.07	54.7	0.02	0.85	15.3	100.0
Quality Control Std	Al <sub>2</sub> O <sub>3</sub> (%)	BaO (%)	CaO (%)	Fe <sub>2</sub> O <sub>3</sub> T (%)	K <sub>2</sub> O (%)	MgO (%)	MnO (%)	Na <sub>2</sub> O (%)	P <sub>2</sub> O <sub>5</sub> (%)	SiO <sub>2</sub> (%)	SrO (%)	TiO <sub>2</sub> (%)			
W-2 Reference Value	15.45	0.02	10.86	10.83	0.63	6.37	0.17	2.20	0.14	52.68	0.02	1.06			
W-2 (1)	15.45	0.02	10.82	10.96	0.62	6.42	0.17	2.22	0.11	52.69	0.03	1.09			
W-2 (2)	15.51	0.02	10.96	10.93	0.61	6.49	0.17	2.21	0.12	52.88	0.03	1.10			
W-2 (3)	15.39	0.02	11.02	10.78	0.61	6.48	0.17	2.22	0.15	52.48	0.03	1.10			
W-2 (4)	15.57	0.02	11.13	10.78	0.62	6.55	0.17	2.27	0.14	52.79	0.03	1.11			
<i>W-2 is a U.S.Geological Survey rock (diabase) standard.</i>															
Average	15.48	0.02	10.98	10.86	0.61	6.49	0.17	2.23	0.13	52.71	0.03	1.10			
Standard Deviation	0.08	0.00	0.13	0.10	0.01	0.05	0.00	0.03	0.02	0.17	0.00	0.01			
%RSD	0.51	1.54	1.19	0.89	1.19	0.83	1.64	1.29	12.79	0.32	1.14	0.82			
%Bias	-0.18	-1.25	-1.13	-0.29	2.51	-1.82	-0.38	-1.31	6.59	-0.06	-29.50	-3.52			
Note:															
Results in weight percent on as-received basis															
Samples were dissolved by lithium metaborate fusion and run on a Perkin-Elmer Optima 5300 ICP (inductively coupled plasma emission spectrometer) Rock standards were used to calibrate the results.															
Elements are report as oxides by convention															

## APPENDIX D: Petrographic Analysis

Sample Number	Qm	Qp	Ch	K	P	Ls	Lm	Lvm	Lvl	Lvf	Lvp	M	H	G	B	Py	other	TOTAL
PL1001	111	22	13	0	30	89	6	1	0	3	7	8	14	2	1	6	0	313
LF1001	8	3	15	1	85	8	0	26	123	14	5	1	7	0	0	12	0	308
LF1002	46	6	7	1	57	4	1	31	91	21	11	0	3	0	0	29	2	310
OR1001	142	18	11	3	34	57	4	0	0	14	0	3	3	7	2	0	5	303
OR1003	133	20	17	0	43	36	7	1	0	4	3	4	8	30	2	10	1	319
OR1004	125	15	11	0	41	54	6	0	0	10	5	11	8	35	0	4	3	328
OR1005	168	17	15	22	8	30	9	1	0	14	9	2	2	0	0	6	3	306
Sample Number	Q	F	L	Qm	Lt	Lm	Ls	Lv										
PL1001	133	30	150	111	172	14	104	17										
LF1001	11	86	211	8	214	1	23	180										
LF1002	52	58	198	46	204	1	11	183										
OR1001	160	37	101	142	119	7	75	14										
OR1003	153	43	122	133	142	11	83	18										
OR1004	140	41	144	125	159	17	100	19										
OR1005	185	30	88	168	105	11	45	30										
Sample Number	% Qm	% Qp	% Ch	% K	% P	% Ls	% Lm	% Lvm	% Lvl	% Lvf	% Lvp	% M	% H	% G	% B	% Py	% other	TOTAL
PL1001	35.46	7.03	4.15	0.00	9.58	28.43	1.92	0.32	0.00	0.96	2.24	2.56	4.47	0.64	0.32	1.92	0.00	100.000
LF1001	2.60	0.97	4.87	0.32	27.60	2.60	0.00	8.44	39.94	4.55	1.62	0.32	2.27	0.00	0.00	3.90	0.00	100.000
LF1002	14.84	1.94	2.26	0.32	18.39	1.29	0.32	10.00	29.35	6.77	3.55	0.00	0.97	0.00	0.00	9.35	0.65	100.000
OR1001	46.86	5.94	3.63	0.99	11.22	18.81	1.32	0.00	0.00	4.62	0.00	0.99	0.99	2.31	0.66	0.00	1.65	100.000
OR1003	41.69	6.27	5.33	0.00	13.48	11.29	2.19	0.31	0.00	1.25	0.94	1.25	2.51	9.40	0.63	3.13	0.31	100.000
OR1004	38.11	4.57	3.35	0.00	12.50	16.46	1.83	0.00	0.00	3.05	1.52	3.35	2.44	10.67	0.00	1.22	0.91	100.000
OR1005	54.90	5.56	4.90	7.19	2.61	9.80	2.94	0.33	0.00	4.58	2.94	0.65	0.65	0.00	0.00	1.96	0.98	100.000
Sample Number	% Q	% F	% L	% Qm	% Lt	% Lm	% Ls	%Lv										
PL1001	42.49	9.58	47.92	35.46	54.95	10.37	77.04	12.59										
LF1001	3.57	27.92	68.51	2.60	69.48	0.49	11.27	88.24										
LF1002	16.77	18.71	63.87	14.84	65.81	0.51	5.64	93.85										
OR1001	52.81	12.21	33.33	46.86	39.27	7.29	78.13	14.58										
OR1003	47.96	13.48	38.24	41.69	44.51	9.82	74.11	16.07										
OR1004	42.68	12.50	43.90	38.11	48.48	12.50	73.53	13.97										
OR1005	60.46	9.80	28.76	54.90	34.31	12.79	52.33	34.88										

Qm- monocrystalline Quartz; Qp- polycrystalline Quartz; Ch- Chert; K- Potassium Feldspar; P- Plagioclase; Ls- sedimentary lithic; Lm- metamorphic lithic; Lvm- microlitic volcanic lithic; Lvl- lathwork volcanic lithic; Lvp- felsic volcanic lithic; M- mica; H- heavy mineral; G- glauconite; B- bioclast; Py- pyroclastic material

## APPENDIX E: Paleocurrent Directions

Paleocurrent Directions				
Location	Facies	Structure	Magnetic North	True North
OR Cerro Abigarrado	6	gutter cast	30 or 210	
OR Dromedary Hill (Mark 12)	1a	trough cross beds		190
	1a	trough cross beds		170
OR Mark 15 (South of Dromedary)	1a	trough cross beds		130
	1a	trough cross beds		135
	1a	trough cross beds		278
	1a	trough cross beds		310
OR Mark 23	1a	trough cross beds		50
OR locality OR-1 Mark 24	1a	trough cross beds		280
	1a	trough cross beds		270
	7	accretion sets		50
OR Mark 25	1a	trough cross beds		310
	1a	trough cross beds		340
	1a	trough cross beds		350
OR walking river cut near Mark 25	1a	trough cross beds		50
	1a	trough cross beds		40
OR Mark 26	1a	trough cross beds		260
	1a	trough cross beds		250
	1a	trough cross beds		230
	1a	trough cross beds		230
	1a	trough cross beds		200
	7	accretion sets		325
OR-2	1a	trough cross beds	240	232
	1a	trough cross beds	220	212
	1a	trough cross beds	210	202
	1a	trough cross beds	260	252
	1a	trough cross beds	250	242
	1a	trough cross beds	240	232
Cerro Solo	1a	trough cross beds	330	322
	1a	trough cross beds	310	312
	1a	trough cross beds	290	282
OR	1a	trough cross beds	330	322
Palm Hill	1a	trough cross beds	320	312
Palm Hill	1a	trough cross beds	320	312
PL-1	1a	trough cross beds	210	202
PL-1	1a	trough cross beds	20	12
PL Mark 31	1a	trough cross beds		180
PL near Mark 36	1a	trough cross beds		200
	1a	trough cross beds		220
	1a	trough cross beds		220
	7	accretion sets		100
PL (near PL-1)	1a	trough cross beds		70
Mark 44 (near basalts)	1a	trough cross beds		330
	1a	planar cross beds		185
Mark 48	1a	trough cross beds		190
	7	accretion sets		85
Mark 49	1a	trough cross beds		155
	7	accretion sets		70
Mark 50	1a	trough cross beds		335
Mark 52	1a	trough cross beds		20
	7	accretion sets		85
	7	accretion sets		100
Mark 54	1a	trough cross beds		260
PL 3 and PL 4 Mark 55	1a	trough cross beds		320
	7	accretion sets	180	172
PL 5	1a	trunk	205	197
	1a	microdelta	240	232
PL 3 and PI 4	1a	trunk	295	287
	1a	trunk	290	282
	1a	trunk	205	197
	1a	trough cross beds	330	322
Mark 58	1a	trough cross beds	260	252
	2	low angle ppl	W	270
	7	accretion sets	W	270
RG second stop	siltstone within fault	fault	10-015	5
LF Mark 41	white cross bedded sand	trough cross beds		170
LF Mark 42	Cross bedded sand	trough cross beds		40
LF	alternating mud and sand (offset by fault)	reverse fault		230



## APPENDIX F: Grain size results

### SAMPLE STATISTICS

SAMPLE IDENTITY: **OR1001**

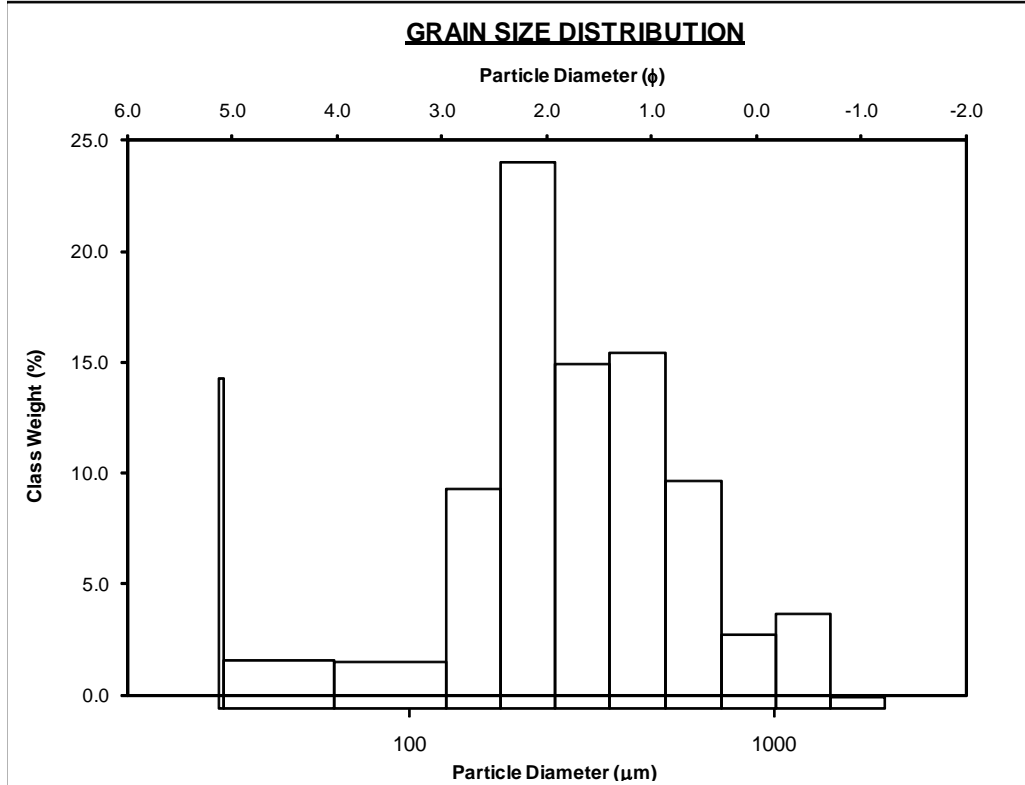
ANALYST & DATE: Emily Comer, 2/19/2011

SAMPLE TYPE: Polymodal, Poorly Sorted

TEXTURAL GROUP: Slightly Gravelly Sand

SEDIMENT NAME: Slightly Very Fine Gravelly Fine Sand

	$\mu\text{m}$	$\phi$	GRAIN SIZE DISTRIBUTION			
	MODE 1:	214.5	2.242	GRAVEL: 1.5%	COARSE SAND: 14.4%	
MODE 2:	426.0	1.254	SAND: 92.6%	MEDIUM SAND: 33.2%		
MODE 3:	30.50	5.035	MUD: 6.0%	FINE SAND: 35.7%		
D <sub>10</sub> :	119.2	0.499		V FINE SAND: 4.3%		
MEDIAN or D <sub>50</sub> :	271.5	1.881	V COARSE GRAVEL: 0.0%	V COARSE SILT: 4.4%		
D <sub>90</sub> :	707.6	3.068	COARSE GRAVEL: 0.0%	COARSE SILT: 1.5%		
(D <sub>90</sub> / D <sub>10</sub> ):	5.934	6.149	MEDIUM GRAVEL: 0.0%	MEDIUM SILT: 0.0%		
(D <sub>90</sub> - D <sub>10</sub> ):	588.4	2.569	FINE GRAVEL: 0.0%	FINE SILT: 0.0%		
(D <sub>75</sub> / D <sub>25</sub> ):	2.430	2.138	V FINE GRAVEL: 1.5%	V FINE SILT: 0.0%		
(D <sub>75</sub> - D <sub>25</sub> ):	269.8	1.281	V COARSE SAND: 4.9%	CLAY: 0.0%		
	METHOD OF MOMENTS			FOLK & WARD METHOD		
	Arithmetic	Geometric	Logarithmic	Geometric	Logarithmic	Description
	$\mu\text{m}$	$\mu\text{m}$	$\phi$	$\mu\text{m}$	$\phi$	
MEAN ( $\bar{x}$ ):	355.3	249.8	1.854	288.8	1.792	Medium Sand
SORTING ( $\sigma$ ):	279.1	2.776	1.127	2.215	1.147	Poorly Sorted
SKEWNESS ( $Sk$ ):	1.870	-2.407	0.468	0.035	-0.035	Symmetrical
KURTOSIS ( $K$ ):	7.171	13.77	3.604	1.400	1.400	Leptokurtic



### SAMPLE STATISTICS

SAMPLE IDENTITY: **OR1001**

ANALYST & DATE: Emily Comer, 2/19/2011

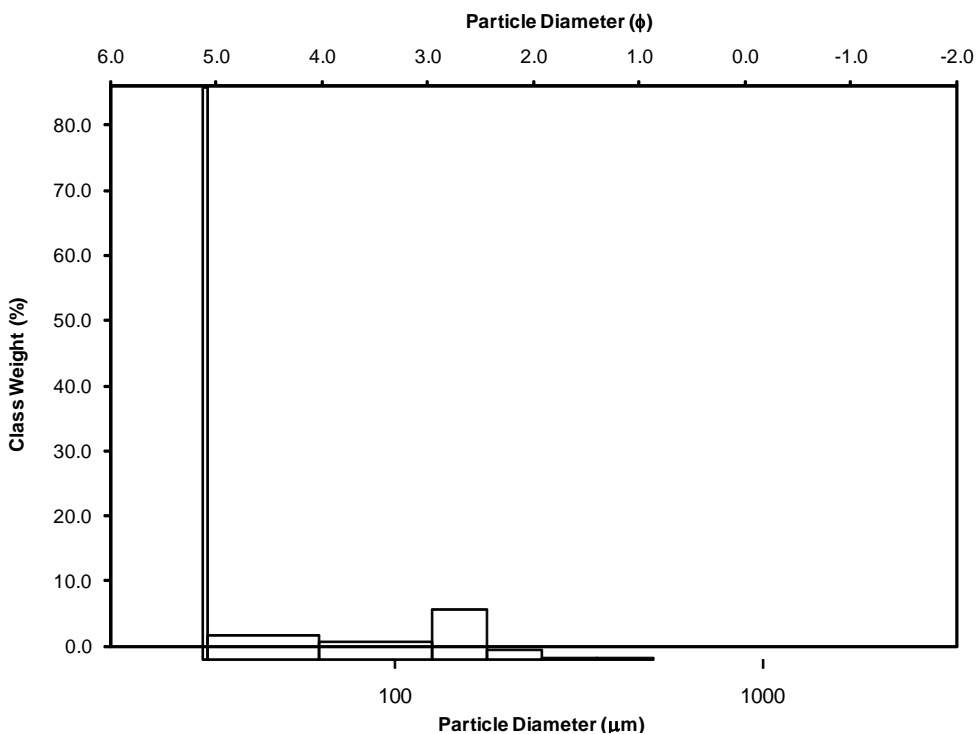
SAMPLE TYPE: Unimodal, Moderately Sorted

TEXTURAL GROUP: Sandy Mud

SEDIMENT NAME: Fine Sandy Coarse Silt

	$\mu\text{m}$		$\phi$		GRAIN SIZE DISTRIBUTION			
	$\mu\text{m}$	$\phi$						
MODE 1:	30.50	5.035			GRAVEL: 0.0%	COARSE SAND: 0.0%		
MODE 2:					SAND: 48.3%	MEDIUM SAND: 1.1%		
MODE 3:					MUD: 51.7%	FINE SAND: 30.1%		
D <sub>10</sub> :	30.36	2.570					V FINE SAND: 17.1%	
MEDIAN or D <sub>50</sub> :	59.37	4.074			V COARSE GRAVEL: 0.0%	V COARSE SILT: 23.9%		
D <sub>90</sub> :	168.4	5.042			COARSE GRAVEL: 0.0%	COARSE SILT: 27.8%		
(D <sub>90</sub> / D <sub>10</sub> ):	5.548	1.962			MEDIUM GRAVEL: 0.0%	MEDIUM SILT: 0.0%		
(D <sub>90</sub> - D <sub>10</sub> ):	138.1	2.472			FINE GRAVEL: 0.0%	FINE SILT: 0.0%		
(D <sub>75</sub> / D <sub>25</sub> ):	4.429	1.748			V FINE GRAVEL: 0.0%	V FINE SILT: 0.0%		
(D <sub>75</sub> - D <sub>25</sub> ):	106.0	2.147			V COARSE SAND: 0.0%	CLAY: 0.0%		
<b>METHOD OF MOMENTS</b>								
	METHOD OF MOMENTS			FOLK & WARD METHOD				
	Arithmetic	Geometric	Logarithmic	Geometric	Logarithmic	Description		
	$\mu\text{m}$	$\mu\text{m}$	$\phi$	$\mu\text{m}$	$\phi$			
MEAN ( $\bar{x}$ ):	88.36	67.36	3.892	65.53	3.932	Very Fine Sand		
SORTING ( $\sigma$ ):	62.86	2.003	1.002	1.984	0.988	Moderately Sorted		
SKEWNESS ( $Sk$ ):	1.347	0.289	-0.289	0.224	-0.224	Coarse Skewed		
KURTOSIS ( $K$ ):	6.136	1.653	1.653	0.508	0.508	Very Platykurtic		

### GRAIN SIZE DISTRIBUTION



### SAMPLE STATISTICS

SAMPLE IDENTITY: **OR1004**

ANALYST & DATE: Emily Comer, 2/19/2011

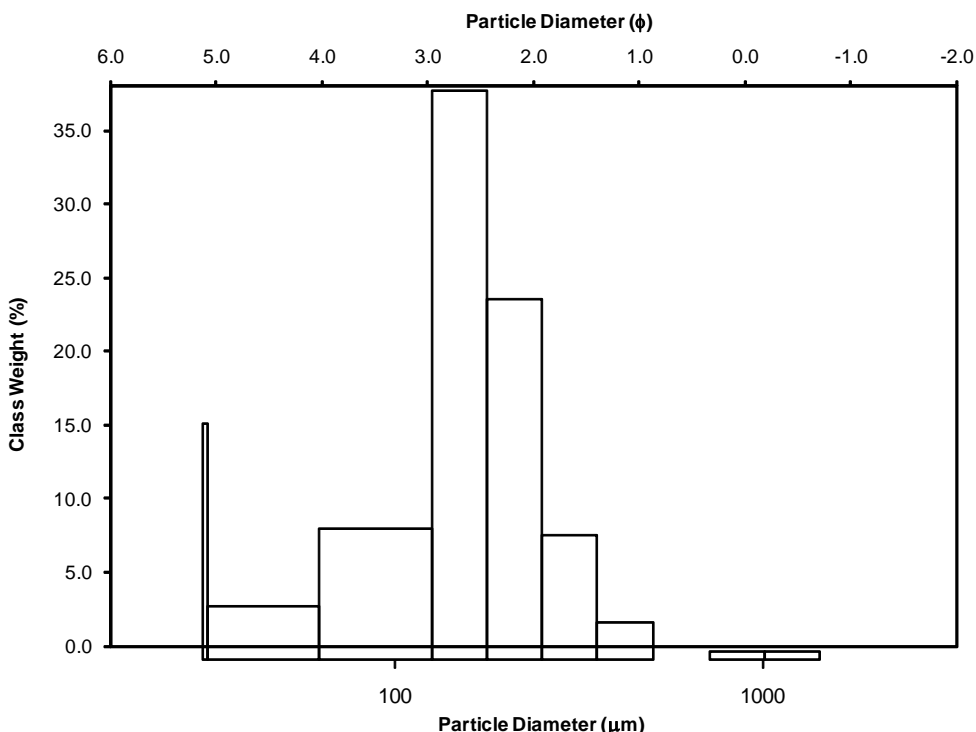
SAMPLE TYPE: Bimodal, Moderately Sorted

TEXTURAL GROUP: Sand

SEDIMENT NAME: Moderately Sorted Fine Sand

	$\mu\text{m}$	$\phi$	GRAIN SIZE DISTRIBUTION			
	MODE 1:	152.0	2.739	GRAVEL: 0.0%	COARSE SAND: 0.5%	
MODE 2:	30.50	5.035	SAND: 91.3%	MEDIUM SAND: 10.8%		
MODE 3:			MUD: 8.7%	FINE SAND: 61.9%		
D <sub>10</sub> :	65.77	1.904		V FINE SAND: 17.6%		
MEDIAN or D <sub>50</sub> :	156.0	2.680	V COARSE GRAVEL: 0.0%	V COARSE SILT: 7.1%		
D <sub>90</sub> :	267.3	3.926	COARSE GRAVEL: 0.0%	COARSE SILT: 1.6%		
(D <sub>90</sub> / D <sub>10</sub> ):	4.064	2.063	MEDIUM GRAVEL: 0.0%	MEDIUM SILT: 0.0%		
(D <sub>90</sub> - D <sub>10</sub> ):	201.5	2.023	FINE GRAVEL: 0.0%	FINE SILT: 0.0%		
(D <sub>75</sub> / D <sub>25</sub> ):	1.742	1.352	V FINE GRAVEL: 0.0%	V FINE SILT: 0.0%		
(D <sub>75</sub> - D <sub>25</sub> ):	88.11	0.801	V COARSE SAND: 0.5%	CLAY: 0.0%		
	METHOD OF MOMENTS		FOLK & WARD METHOD			
	Arithmetic	Geometric	Logarithmic	Geometric	Logarithmic	Description
	$\mu\text{m}$	$\mu\text{m}$	$\phi$	$\mu\text{m}$	$\phi$	
MEAN ( $\bar{x}$ ):	174.9	146.4	2.772	145.2	2.784	Fine Sand
SORTING ( $\sigma$ ):	117.1	1.764	0.819	1.760	0.815	Moderately Sorted
SKEWNESS ( $Sk$ ):	4.574	-0.338	0.338	-0.233	0.233	Fine Skewed
KURTOSIS ( $K$ ):	36.64	4.327	4.327	1.490	1.490	Leptokurtic

### GRAIN SIZE DISTRIBUTION



### SAMPLE STATISTICS

SAMPLE IDENTITY: **OR1005**

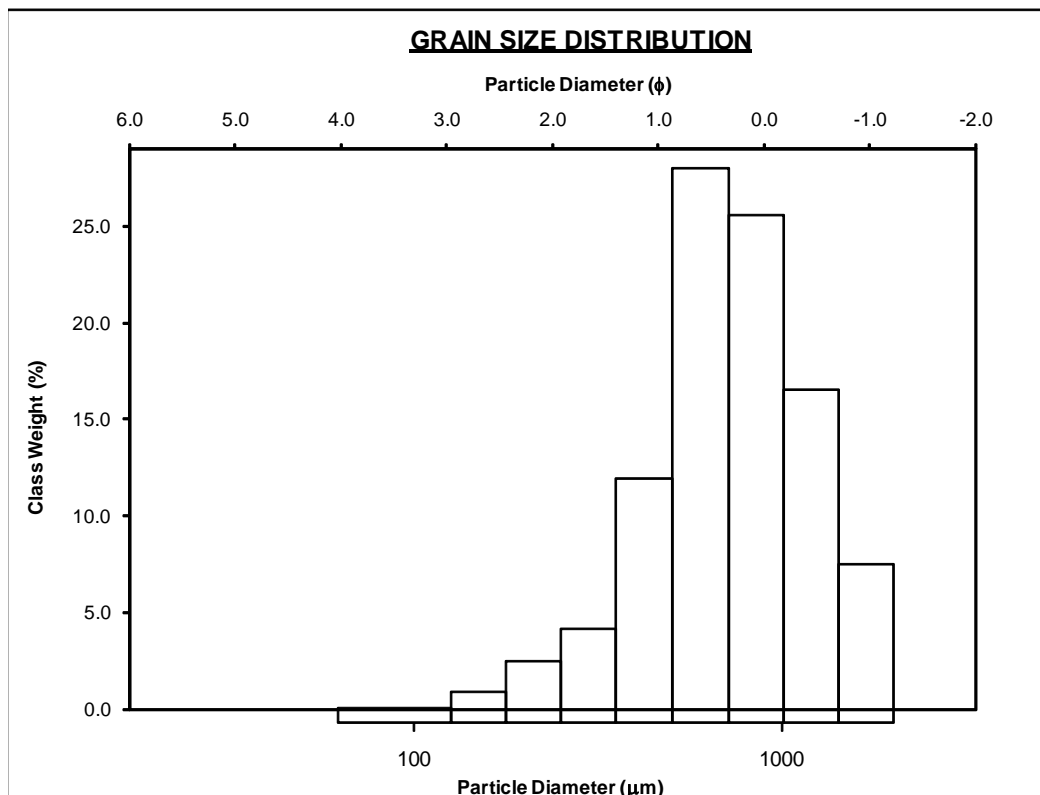
ANALYST & DATE: Emily Comer, 2/17/2011

SAMPLE TYPE: Unimodal, Moderately Sorted

TEXTURAL GROUP: Slightly Gravelly Sand

SEDIMENT NAME: Slightly Very Fine Gravelly Coarse Sand

	$\mu\text{m}$		$\phi$		GRAIN SIZE DISTRIBUTION			
	$\mu\text{m}$	$\phi$						
MODE 1:	606.0	0.745			GRAVEL: 0.0%	COARSE SAND: 52.7%		
MODE 2:					SAND: 100.0%	MEDIUM SAND: 16.9%		
MODE 3:					MUD: 0.0%	FINE SAND: 4.5%		
D <sub>10</sub> :	339.4	-0.435					V FINE SAND: 1.5%	
MEDIAN or D <sub>50</sub> :	704.4	0.506			V COARSE GRAVEL: 0.0%		V COARSE SILT: 0.0%	
D <sub>90</sub> :	1352.1	1.559			COARSE GRAVEL: 0.0%		COARSE SILT: 0.0%	
(D <sub>90</sub> / D <sub>10</sub> ):	3.983	-3.582			MEDIUM GRAVEL: 0.0%		MEDIUM SILT: 0.0%	
(D <sub>90</sub> - D <sub>10</sub> ):	1012.7	1.994			FINE GRAVEL: 0.0%		FINE SILT: 0.0%	
(D <sub>75</sub> / D <sub>25</sub> ):	1.929	87.99			V FINE GRAVEL: 0.0%		V FINE SILT: 0.0%	
(D <sub>75</sub> - D <sub>25</sub> ):	478.0	0.948			V COARSE SAND: 24.4%		CLAY: 0.0%	
<b>METHOD OF MOMENTS</b>								
	METHOD OF MOMENTS			FOLK & WARD METHOD				
	Arithmetic	Geometric	Logarithmic	Geometric	Logarithmic	Description		
	$\mu\text{m}$	$\mu\text{m}$	$\phi$	$\mu\text{m}$	$\phi$			
MEAN ( $\bar{x}$ ):	792.1	677.2	0.562	701.8	0.511	Coarse Sand		
SORTING ( $\sigma$ ):	395.1	1.775	0.828	1.758	0.814	Moderately Sorted		
SKEWNESS ( $Sk$ ):	0.722	-0.910	0.910	-0.086	0.086	Symmetrical		
KURTOSIS ( $K$ ):	3.074	4.490	4.490	1.228	1.228	Leptokurtic		



### SAMPLE STATISTICS

SAMPLE IDENTITY: **PL1001**

ANALYST & DATE: Emily Comer, 2/19/2011

SAMPLE TYPE: Bimodal, Moderately Well Sorted

TEXTURAL GROUP: Muddy Sand

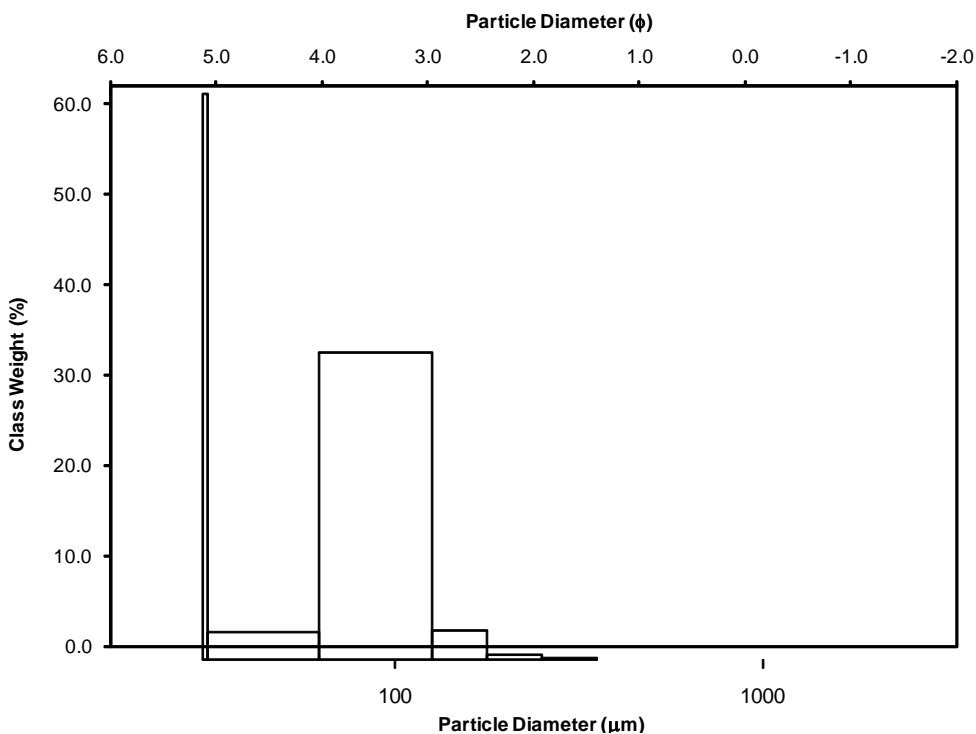
SEDIMENT NAME: Very Coarse Silty Very Fine Sand

	$\mu\text{m}$ $\phi$		GRAIN SIZE DISTRIBUTION			
	MODE 1:	30.50	5.035	GRAVEL: 0.0%	COARSE SAND: 0.0%	
MODE 2:	94.00	3.500	SAND: 84.9%	MEDIUM SAND: 0.1%		
MODE 3:			MUD: 15.1%	FINE SAND: 5.2%		
D <sub>10</sub> :	41.59	3.059		V FINE SAND: 79.6%		
MEDIAN or D <sub>50</sub> :	84.71	3.561	V COARSE GRAVEL: 0.0%	V COARSE SILT: 8.0%		
D <sub>90</sub> :	120.0	4.588	COARSE GRAVEL: 0.0%	COARSE SILT: 7.0%		
(D <sub>90</sub> / D <sub>10</sub> ):	2.885	1.500	MEDIUM GRAVEL: 0.0%	MEDIUM SILT: 0.0%		
(D <sub>90</sub> - D <sub>10</sub> ):	78.42	1.529	FINE GRAVEL: 0.0%	FINE SILT: 0.0%		
(D <sub>75</sub> / D <sub>25</sub> ):	1.546	1.193	V FINE GRAVEL: 0.0%	V FINE SILT: 0.0%		
(D <sub>75</sub> - D <sub>25</sub> ):	37.17	0.628	V COARSE SAND: 0.0%	CLAY: 0.0%		

	METHOD OF MOMENTS			FOLK & WARD METHOD		
	Arithmetic	Geometric	Logarithmic	Geometric	Logarithmic	Description
	$\mu\text{m}$	$\mu\text{m}$	$\phi$	$\mu\text{m}$	$\phi$	
MEAN ( $\bar{x}$ ):	89.26	80.10	3.642	84.71	3.561	Very Fine Sand
SORTING ( $\sigma$ ):	26.09	1.416	0.501	1.435	0.521	Moderately Well Sorted
SKEWNESS ( $Sk$ ):	0.719	-1.441	1.441	-0.221	0.221	Fine Skewed
KURTOSIS ( $K$ ):	12.19	5.783	5.783	1.324	1.324	Leptokurtic

### GRAIN SIZE DISTRIBUTION



### SAMPLE STATISTICS

SAMPLE IDENTITY: **LF1001**

ANALYST & DATE: Emily Comer, 2/19/2011

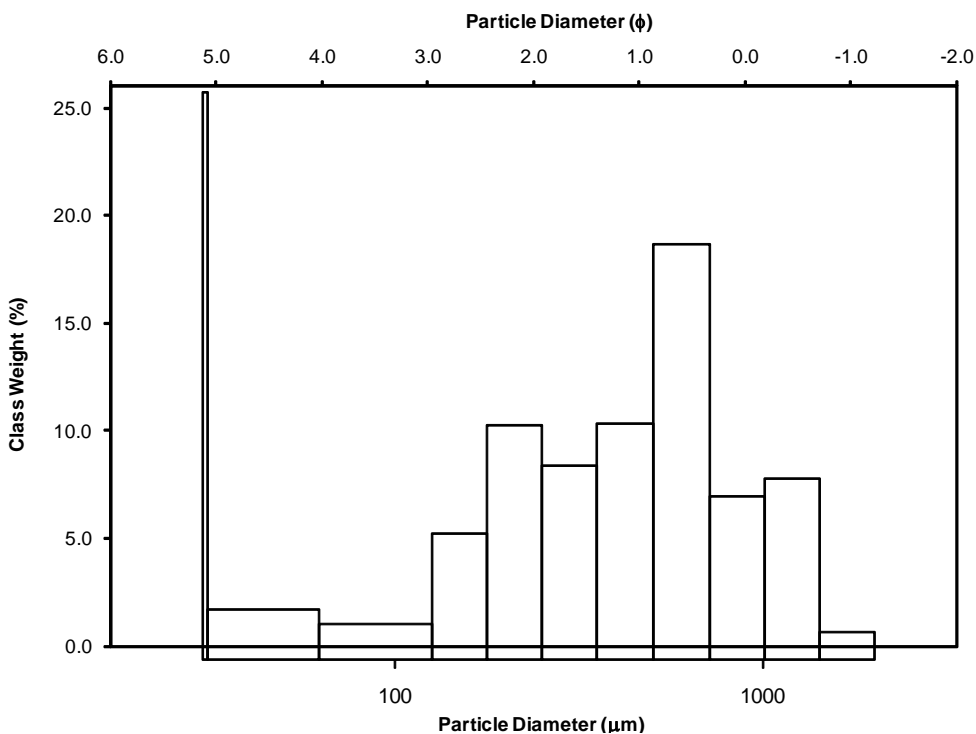
SAMPLE TYPE: Polymodal, Poorly Sorted

TEXTURAL GROUP: Slightly Gravelly Sand

SEDIMENT NAME: Slightly Very Fine Gravelly Coarse Sand

	$\mu\text{m}$	$\phi$	GRAIN SIZE DISTRIBUTION			
			GRAVEL: 0.0%	COARSE SAND: 32.4%	SAND: 91.5%	MEDIUM SAND: 24.0%
MODE 1:	30.50	5.035	MUD: 8.5%	FINE SAND: 19.8%		
MODE 2:	606.0	0.745		V FINE SAND: 3.9%		
MODE 3:	214.5	2.242				
D <sub>10</sub> :	81.61	-0.073	V COARSE GRAVEL: 0.0%	V COARSE SILT: 5.5%		
MEDIAN or D <sub>50</sub> :	424.9	1.235	COARSE GRAVEL: 0.0%	COARSE SILT: 3.0%		
D <sub>90</sub> :	1052.1	3.615	MEDIUM GRAVEL: 0.0%	MEDIUM SILT: 0.0%		
(D <sub>90</sub> / D <sub>10</sub> ):	12.89	-49.349	FINE GRAVEL: 0.0%	FINE SILT: 0.0%		
(D <sub>90</sub> - D <sub>10</sub> ):	970.5	3.688	V FINE GRAVEL: 0.0%	V FINE SILT: 0.0%		
(D <sub>75</sub> / D <sub>25</sub> ):	3.213	3.847	V COARSE SAND: 11.5%	CLAY: 0.0%		
(D <sub>75</sub> - D <sub>25</sub> ):	457.1	1.684				
	METHOD OF MOMENTS		FOLK & WARD METHOD			
	Arithmetic	Geometric	Logarithmic	Geometric	Logarithmic	Description
	$\mu\text{m}$	$\mu\text{m}$	$\phi$	$\mu\text{m}$	$\phi$	
MEAN ( $\bar{x}$ ):	498.0	346.5	1.529	377.4	1.406	Medium Sand
SORTING ( $\sigma$ ):	365.4	2.584	1.369	2.591	1.373	Poorly Sorted
SKEWNESS ( $Sk$ ):	0.997	-0.847	0.847	-0.290	0.290	Fine Skewed
KURTOSIS ( $K$ ):	3.648	3.230	3.230	1.208	1.208	Leptokurtic

### GRAIN SIZE DISTRIBUTION



### SAMPLE STATISTICS

SAMPLE IDENTITY: **LF1002**

ANALYST & DATE: Emily Comer, 2/19/2011

SAMPLE TYPE: Unimodal, Moderately Sorted

TEXTURAL GROUP: Slightly Gravelly Sand

SEDIMENT NAME: Slightly Very Fine Gravelly Coarse Sand

	$\mu\text{m}$ $\phi$		GRAIN SIZE DISTRIBUTION			
	MODE 1:	856.0	0.245	GRAVEL: 4.4%	COARSE SAND: 52.9%	
MODE 2:			SAND: 94.6%	MEDIUM SAND: 12.6%		
MODE 3:			MUD: 1.0%	FINE SAND: 3.4%		
D <sub>10</sub> :	380.9	-0.708		V FINE SAND: 0.5%		
MEDIAN or D <sub>50</sub> :	784.7	0.350	V COARSE GRAVEL: 0.0%	V COARSE SILT: 1.0%		
D <sub>90</sub> :	1634.0	1.392	COARSE GRAVEL: 0.0%	COARSE SILT: 0.0%		
(D <sub>90</sub> / D <sub>10</sub> ):	4.289	-1.966	MEDIUM GRAVEL: 0.0%	MEDIUM SILT: 0.0%		
(D <sub>90</sub> - D <sub>10</sub> ):	1253.1	2.101	FINE GRAVEL: 0.0%	FINE SILT: 0.0%		
(D <sub>75</sub> / D <sub>25</sub> ):	1.985	-5.661	V FINE GRAVEL: 4.4%	V FINE SILT: 0.0%		
(D <sub>75</sub> - D <sub>25</sub> ):	550.0	0.989	V COARSE SAND: 25.3%	CLAY: 0.0%		
	METHOD OF MOMENTS			FOLK & WARD METHOD		
	Arithmetic	Geometric	Logarithmic	Geometric	Logarithmic	Description
	$\mu\text{m}$	$\mu\text{m}$	$\phi$	$\mu\text{m}$	$\phi$	
MEAN ( $\bar{x}$ ):	802.6	538.9	0.457	795.6	0.330	Coarse Sand
SORTING ( $\sigma$ ):	429.9	4.326	0.845	1.769	0.823	Moderately Sorted
SKEWNESS ( $S_k$ ):	0.436	-3.456	1.585	-0.032	0.032	Symmetrical
KURTOSIS ( $K$ ):	2.939	15.01	7.865	1.217	1.217	Leptokurtic

